Mineral weathering and soil formation: the role of microorganisms

Andrew William Bray

Submitted in accordance with the requirements for the degree of

Doctor of Philosophy

University of Leeds

School of Earth and Environment

January, 2014

DECLARATION

The candidate confirms that the work submitted is his own, except where work which has formed part of jointly-authored publications has been included. The contribution of the candidate and the other authors to this work has been explicitly indicated below. The candidate confirms that appropriate credit has been given within the thesis where reference has been made to the work of others.

Chapter 4 is reproduction of a peer-reviewed publication in *Geochimica et Cosmochimica Acta*:

Bray A. W., Benning L. G., Bonneville S., Oelkers E. H. (2014) Biotite surface chemistry as a function of aqueous fluid composition. *Geochim. Cosmochim Acta* **128**, 58-70.

The candidate conducted the experiments, analyses, data processing, interpretation and preparation of the manuscript. Liane G. Benning contributed with the study idea, and aided in the data interpretation and manuscript preparation process. Steeve Bonneville contributed to the data processing, interpretation and manuscript preparation. Eric H. Oelkers contributed at the experiment design stage as well as the data processing, interpretation and manuscript preparation. A reprint of the original manuscript is present in Appendix C.

Chapter 5 is a reproduction of a manuscript prepared for submission to *Geochimica et Cosmochimica Acta*.

Bray A. W., Oelkers E. H., Bonneville S., Wolff-Boenisch D., Potts N. J., Fones G., Benning L. G. The effect of pH, grain size and organic ligands on biotite weathering kinetics

The candidate conducted the experiments, analyses (except ICP-MS measurements), data processing, interpretation and preparation of the manuscript. Eric

H. Oelkers contributed to the experiment design, provided insight during the data processing and interpretation, and aided in the manuscript preparation. Steeve Bonneville aided in the preparations for the Moen biotite experiments, contributed to the data interpretation and manuscript preparation. Domenik Wolff-Boenisch aided in the design and execution of the open-system Moen biotite experiments and contributed to the manuscript preparation. Nicola J. Potts aided in the preparation for and execution of the closed-system Grasåsen experiments. Gary Fones conducted the aqueous analysis of a selection of fluids from the closed-system Grasåsen experiments by ICP-MS. Liane G. Benning contributed the study idea and aided in the experiment design, data interpretation and manuscript preparation process.

Collaborative publications

Bonneville S., Morgan D. J., Schmalenberger A., **Bray A.**, Brown A., Banwart S. A., Benning L. G. (2011) Tree-mycorrhiza symbiosis accelerate mineral weathering: Evidences from nanometer-scale elemental fluxes at the hypha–mineral interface. *Geochimica et Cosmochimica Acta* **75**, 6988-7005.

The candidate provided experimental data from abiotic, solution based closed- and open-system biotite dissolution experiments for comparison to mycorrhiza driven biotite alteration rates. The candidate also helped in the manuscript preparation. A reprint of the original manuscript is present in Appendix D.

For Joe and Ben

"Air. I want air, and sunshine, and blue sky, the feeling of the breeze upon my face, the feeling of the turf beneath my feet, and no walls but the far-off mountain tops. Then I am free and strong, once more myself."

Beltran Cruzado

From: The Spanish Student. A Play in Three Acts

Henry Wadsworth Longfellow, 1843

ACKNOWLEDGEMENTS

I could not have produced this work without the help, guidance, friendship, supervision and inspiration of a multitude of individuals. I will attempt to thank them all here.

Firstly, my supervisors Liane G. Benning, Steeve Bonneville, and Bruce Yardley; without their astute advice and scientific zeal this work may not have happened, and it wouldn't have been half as fun.

Liane has been a constant source of inspiration through this process. I am particularly thankful for her open door and her patience during the innumerable 'got a minute?' discussions I instigated. I have learned an awful lot from Liane and I know there is still much to learn!

With Steeve's help I cut my teeth in the laboratory and have started to grasp what it means to be a researcher. I have learned a lot from Steeve's attention to detail; whether making sure my hand doesn't wave over a sterilised agar plate whilst carefully and accurately placing the roots of a Pinus sylvestris seedling, or trawling through a spreadsheet of 30000 cells to find the one with a mistake; he has helped to temper my formerly blasé approach.

This thesis is part of the wider World Universities Network Weathering Science Consortium (WSC) and I am thankful to all the consortium members for their research and discussions which have helped to frame this study. I am particularly thankful to Adele L. Duran and Irene Johnson for their instruction and support in setting up and maintaining the experimental plant-fungi-continuum microcosms. Thanks also go to Claire Corkhill, María Romero-González, Achim Schmalenberger, and the beamline scientists at B22, Diamond Light Source for their help during the data collection for Chapter 6. I would also like to thank the help of Gabriella Kakonyi and Gary Fones during ICP-MS analyses and data evaluation.

During this study I have also had the privilege of working with Domenik Wolff-Boenisch at the University of Iceland and Eric Oelkers at Géosciences Environnement Toulouse for which I am extremely grateful. I am particularly thankful to Eric who has taken time to teach me a lot about dissolution processes and aqueous geochemistry. Thanks also to the folks at these two institutes who made my visits fun and productive, namely: Alfreðsson, Berninger, Björke, Bosc, Declercq, Gudbrandsson, Jones, Keller, Mavromatis, Rinder, Rodríguez, Sigurðardóttir and others.

Cohen Geochemistry has been an excellent group of scientists to be part of through my time in Leeds. There are many fantastic individuals who have supported me in the research and social aspects of doing a PhD. Particular thanks go to Nicci for helping me label approximately 8000 tubes; Haggis for forming the KWG (Kinetics working group) with me, and being the only other member of our one meeting; Jörgen for many discussions on solution chemistry and kinetics; Romain for his friendship and thoughtfulness in discussions on everything from the most efficient route to the coffee room, to the units of rate constants; Steffi for climbing; and Sam Allshorn for his tireless efforts in ensuring the labs ran so smoothly. I'd also like to thank Luke for being a sounding board over many coffees; James and Santi, my original Garstang office buddies; the 8.154 folks; and the rest of the Benning group.

I'd also like to thank Eliot, Mark, Sim, James, Giles, Ali, Dave, Fiona and Paul for sharing places with me over the last few years and making home a relaxing place to be. I owe a huge amount of thanks to Lucy for her support and encouragement, and for her enthusiasm for the topic of this thesis, which she got very good at pretending she's been interested in!

Final thanks go to my family; Chris, Helen (parents), Sarah, Adam, Tom (siblings), Joe and Ben (nephews). You guys have been great. Chris will try to claim responsibility for me getting to this stage, having paved the way through studying a Soil Science MSc and completing a PhD in chemistry. Though I'm sure whatever I have done (and will do) the Revd. Dr. C. L. Bray BSc MSc DipTh DPS BSc MRes PhD MRSC PGCE will claim I'm copying him as I don't think there is much he hasn't done… I was set the challenge of citing one of Chris' papers from his MSc studies, you'll have to read on to see if I managed it! (Or just check the references).

There is a bunch of people I haven't named, along with those I have, without whom I wouldn't have been able to produce this tome/would have produced it much more quickly and to a higher standard.

Thank you all.

ABSTRACT

Mycorrhizal fungi play a significant role in primary mineral weathering and soil formation. Due to their direct access to solar energy through symbiotic plant partners, fungi are able to extend into soils, acting as biosensors for nutrients which they subsequently uptake and supply to their plant partners. Mycorrhizal fungi operate at the individual hypha scale, mechanically forcing and chemically altering minerals to extract nutrient elements. The hyphae acidify their local environment by exuding organic acids, which are also involved in mineral breakdown. To extend the work on mycorrhizal fungal biotite weathering completed as part of the Weathering Science Consortium the mechanisms and kinetics of biotite dissolution were investigated. This was done by characterising the biotite surface as a function of fluid composition and measuring dissolution rates.

During contact with dilute solutions, the chemical composition of the biotite surface changed dramatically as a function of pH. The rapid release of elements during these experiments was not stoichiometric but was highly pH dependent. A combination of electrokinetic measurements and potentiometric titrations further highlighted the variable composition of the biotite surface by yielding two values for zero points of charge, separated by ~7 pH units.

Abiotic dissolution of biotite progressed by the formation of a dissolution front depleted in K Mg, Fe and Al, the extent of which varies spatially and with pH. The presence of the organic ligands, citric acid, oxalic acid and DFOB (desferrioxamine B) slightly enhanced the overall biotite dissolution rate in lightly acidic and near neutral pH conditions.

The growth rate of mycorrhizal fungi over the surface of biotite was quantified at two levels of atmospheric CO_2, 350 ppm and 1500 ppm. Initial growth rate calculations in the 1500 ppm experiments revealed hyphae to grow at an average of 10 μm d^{-1}.

Finally, changes in the biochemistry of fungal hypha were observed using μ-FTIR. Results suggested that biochemical changes present could be related to changes in fungal functionality spatially in future work.

CONTENTS

1. FIGURES

2. TABLES

Chapter 1. Introduction

This thesis is part of a wider consortium of work, involving approximately 20 researchers from 4 institutes, to quantify the role of biology in the physical and chemical alteration or rocks and minerals at Earth's surface, forming soil and supplying nutrients to the biosphere. The Weathering Science Consortium (WSC) is a Natural Environment Research Council funded consortium (NE/C004566/1) comprising of groups at the universities of Sheffield, Bristol and Leeds. In the present chapter I will provide the scope of the work in this document and present the objectives, approaches and outline of the remainder of this thesis.

1. 1. BACKGROUND INFORMATION

Soil is an extremely important resource which, due to intense agriculture, deforestation and pollution, is becoming a limited resource. Soil is the unconsolidated mixture of minerals and organic matter that sits at the top of the mixing region of the atmo-, hydro-, bio-, geo- and anthropo-spheres known as the Critical Zone. The chemical and physical characteristics of soil reflect the effects of climate, topography, macro- and microorganisms acting on a parent material through time (Jenny, 1941), and the influence of human activity (e.g. Rutherford and Bray, 1979). It has been estimated that in some areas rates of soil loss are two orders of magnitude greater than soil production (Pimentel et al., 1995). Coupling this with the increasing demands of the global population and the challenges of food security in the 21st century leads to soil being an incredibly important arena for research focus. For soil management strategies to be effective the soil processes, including formation and nutrient cycling need a better understanding (Banwart, 2011). This need for a holistic, science led approach to soil resource management has been highlighted by a recent Royal Society of Chemistry report (Bridge and Banwart, 2012).

The classic view of the soil system holds abiotic processes as key in controlling soil formation and nutrient liberation from minerals and rocks. However, we now know that life plays a significant role in both mineral weathering and soil formation. It has been suggested that mineral weathering rates are 2 to 10 times higher in vegetated soils than non-vegetated soils due to the combined action of plants, particularly vascular plants, and soil dwelling microorganisms. In fact mycorrhizal fungi have been suggested as the main agents of mineral weathering in soils (Landeweert et al., 2001) due to their direct link to solar energy through symbiosis with plants.

Several recent studies have shown the importance of fungi in mineral weathering by quantifying processes at the nano and micro scale (Bonneville et al., 2009; Bonneville et al., 2011; Saccone et al., 2012; Gazzè et al., 2012; Smits et al., 2012; Gazzè et al., 2013) and converting these observations to a global scale (e.g. Taylor et al, 2009; Taylor et al., 2011; Taylor et al., 2012; Quirk et al., 2012). However, there are still many questions to be answered. Of the most important topics are those which will help us to refine our estimates of mineral weathering and nutrient fluxes both in biological and abiotic soil processes. This thesis is focussed on understanding the processes of mineral weathering at the scale of an individual hypha, to provide further experimental data to enlighten our existing interpretations of biologically driven mineral weathering. In the following chapter, I will describe some of the current literature and provide the scope which frames the questions I will address in the remainder of this thesis.

1. 2. RESEARCH OBJECTIVES

We have observed that the fungal driven bio-weathering of biotite involves 'bio-fracking', which is both physical forcing and chemical alteration of the biotite structure to extract nutrients such as K, Mg and Fe. What is not clear, is the mechanisms by which the fungi alter biotite, how these mechanisms promote nutrient element release from the

mineral, and how the fungus behaves both physically (i.e. growth and functionality) and biochemically. To understand how microorganisms are involved in biotite weathering we first need to understand how the biotite interacts with fluids, how the chemistry of biotite is affected by fluid composition, and how this controls mineral dissolution. This will enable us to better understand the processes surrounds organic ligand promoted biotite dissolution, linking to observations of organic acid exudation on minerals surfaces (Saccone et al., 2012; Gazzè et al., 2012). Therefore, the research objectives of this thesis can be divided into three main areas:

I. Determination of the effect of fluid composition on the surface chemistry of biotite. Surface chemistry and net surface charge are inherently linked. One of the proposed mechanisms of organic ligand interaction with mineral surfaces is through adsorption, which is partly charge controlled. We hypothesise that the near surface chemistry of biotite changes as a function of pH, and that this influences organic ligand interaction with biotite.

II. Determination of the rate and mechanism of element release from biotite as a function of fluid composition and organic ligand presence. The release rate of elements from minerals into the bulk fluid is controlled by simultaneous dissolution/precipitation reactions. We hypothesise that element release rates are pH dependent and controlled by the saturation state of the fluid with respect to secondary phases. We also hypothesise that the presence of organic ligands enhances the release of elements to the bulk fluid via a combination of surface and fluid based complexation, lowering the saturation state with respect to secondary phases.

III. To determine the growth kinetics and surface coverage of a mycorrhizal fungus on a mineral surface to obtain growth kinetics and fungal-mineral contact surface area for refinement of fungal mineral weathering as a function of pCO_2. And

determine the spatial biochemistry of a fungal hypha to assess what controls hypha functionality observed during fungal mineral weathering. We hypothesise that fungal growth rates are linked to pCO_2 as the symbiotic plant partners are able to fix more carbon by photosynthesis. We also hypothesise that we can observe spatial changes in fungal biochemistry using μ-FTIR, and that this is linked to the fungal functionality.

These objectives have been addressed using a variety of experimental techniques. All of these techniques and methods are outlined in chapter 3, with accompanying theoretical descriptions where necessary.

1. 3. THESIS OUTLINE

This thesis consists of 7 chapters, the first of which you are reaching the end of. In the second chapter there is an overview of the literature on biotite, including previous dissolution and weathering studies, mycorrhizal fungi and their contribution to mineral weathering. The third chapter contains a detailed description of the experimental and analytical methods used through this PhD project. After the third chapter are three results chapters. Chapter 4 describes the chemical composition of the biotite surface and how this changes as a function of pH, providing information for understanding how biotite dissolves which is discussed in chapter 5. Along with the mechanism of dissolution, chapter 5 also presents data on the effect of known organic exudates on the dissolution kinetics of biotite. Chapter 6 presents the data on fungal growth rates and surface coverage, and the spatial distribution of biochemical functional groups in different section of fungal hyphae. The results from chapters 4, 5 and 6 are summarised and discussed in chapter 7. Finally the appendices hold supplementary information from the results chapters and the reprints of two peer-reviewed publications linked to this thesis.

Chapter 2. Literature Review

This chapter summarizes the literature on biotite dissolution/weathering, biologically driven mineral weathering and the role of organic exudates in promoting weathering.

2. 1. BIOTITE

Biotite is a sub group of the mica group of phyllosilicate minerals, from the Greek '*Phyllo'*, meaning leaf. Phyllosilicates, or sheet silicates, are minerals formed by parallel silicate tetrahedral and octahedral sheets. Mica group minerals are 2:1 phyllosilicates comprised of a tri-octahedral sheet sandwiched between two sheets of tetrahedral, forming T-O-T (tetrahedral-octahedral-tetrahedral) assemblages which are held together by inter layer cations, K^+ for biotite (Fig. 2.1). Biotite has the general chemical formula $K\,(Mg, Fe)_3\,AlSi_3O_{10}\,(F, OH)_2$ forming a solid-solution series between the iron and magnesium endmembers, respectively annite ($K\,Fe_3^{2+}\,AlSi_3O_{10}\,(OH, F)_2$) and phlogopite ($K\,Mg_3\,AlSi_3O_{10}\,(OH)_2$). There is also a secondary, less common, aluminium rich solid-solution series between the Fe rich endmember siderophyllite and Mg rich eastonite

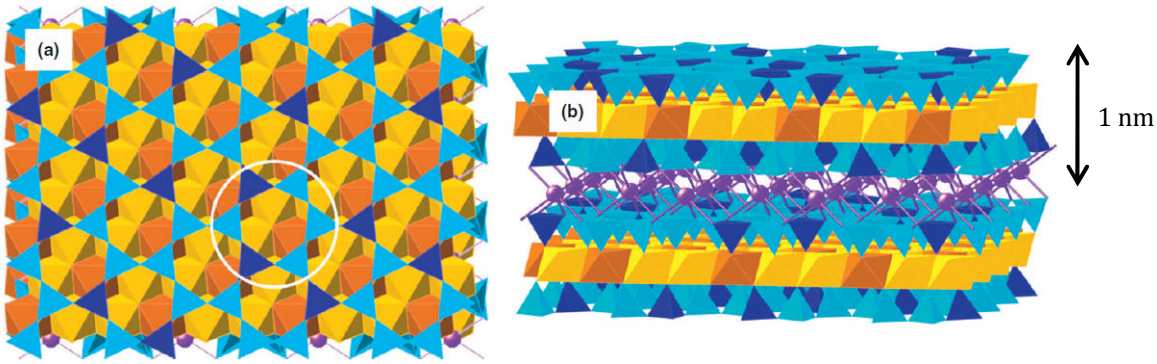

Figure 2.1

Idealised representation of the biotite structure. (a) The basal (001) surface (top-view), with a six-member tetrahedron circled. (b) Side view, with 2 T-O-T sheets bound by K^+ ions. Si^{4+} bearing tetrahedra are light blue; Al^{3+} substituted tetrahedra are dark blue; Mg^{2+} and Fe^{2+} octahedra are respectively yellow and orange, and the K^+ interlayer ions are violet. Generated using Crystal Maker 2.3, from McMaster, 2012.

(Deer et al., 1966). In the case of biotite the octahedral sheets are comprised mainly of tri-octahedrally coordinated Fe(II) and Mg, though in some cases trivalent ions (e.g. Al and Fe(III)) can substitute. The tetrahedral sheet is composed of Si and Al, which gives the sheet a net negative charge due to the charge imbalance cause by Al. The charge imbalance in the tetrahedral sheets holds potassium interlayer ions in place, binding T-O-T layers together. One unit cell of biotite (T-O-T layer and interlayer) is 10 Å, 1nm thick; Fig. 2.1 shows the idealised structure of biotite.

The rather weak binding between T-O-T assemblages interlayer forces cause biotite to have perfect cleavage parallel to the (001) plane, meaning that biotite is often found as flakes in natural settings. Biotite is the most common mica at Earth's surface and it is estimated to count for approximately 7% of exposed crustal surface, approximately 14% of possible K-bearing minerals (Nesbitt and Young, 1984). The composition of biotite means that it is a major source of nutrients for terrestrial organisms. Potassium is a primary nutrient for plants as it is important in controlling stomatal activity, photosynthesis, enzyme activation, and water, sugar and nutrient transport (Amtmann and Rubio, 2012). Iron and magnesium are secondary nutrients; Fe is used in enzyme and chlorophyll production and Mg is part of the chlorophyll molecule (Wilkinson et al., 1990). Biotite is more important to consider than other K-bearing minerals as, for example, K-feldspar dissolution rates are up to 4 orders of magnitude slower than biotite (Malmström and Banwart, 1997; Harouiya and Oelkers, 2004). However, the overall mechanism or pathway linking nutrient release from the biotite structure, via abiotic or biotic weathering reactions, to biochemical changes induced in microorganisms in response to the availability of such nutrients (e.g. fungal metabolism and growth processes) are still poorly defined.

2. 2. BIOTITE DISSOLUTION/WEATHERING

Due to the importance of mica minerals in a variety of geological settings there have been a number of studies over the last 25 years investigating the nature of interactions between biotite (and other micas) and *fluids* (Acker and Bricker, 1992; Turpault and Trotignon, 1994; Kalinowski and Schweda, 1996; Malmström et al., 1996; Malmström and Banwart, 1997; Taylor et al., 2000; Bosbach, et al., 2000; Bickmore et al., 2001; Murakami et al, 2003; Bickmore et al., 2003; Murakami et al, 2004; He et al., 2005; McMaster et al., 2008; Sugimori et al, 2009; Haward et al., 2011; Voinot et al., 2013; Cappelli, et al., 2013; Gazzè et al., 2014; Bray et al., 2014), *microorganisms* (Balogh-Brunstad et al., 2008b; Hopf et al., 2009; Bonneville et al., 2009; Balland et al., 2010; Bonneville et al, 2011), and a combination of both in *field-based measurements and estimations of biotite weathering* (Swodoba-Colberg and Drever, 1993; Murphy et al., 1998; Föllmi, et al., 2009).

These studies have all shown that biotite dissolution kinetics are highly pH dependent both in the acidic and alkaline ranges. At each pH the experimentally derived dissolution rates can vary by up to 2-3 log units, indicating that small variations in the biotite composition, experimental differences of rates calculations may be responsible for these variations. Unsurprisingly, in the case of abiotic experimental results (Fig. 2.2) the pH of minimum dissolution rate is between 5 and 6 at $\sim 10^{-11.5}$ to 10^{-12} moles of biotite m^{-2} s^{-1} as this is the pH of minimum Fe and Al solubility. However, the level of dependency, or the reaction order with respect to H^+ concentration in the acidic pH range, is between 0.34 (Acker and Bricker, 1992) to 0.61 (Kalinowski and Schweda, 1996) when dissolution rates (R)are described by the empirical formula

$$R = k_{\mathrm{H}} a_{\mathrm{H}^+}{}^{q}$$

Eq. 2.1

where k is the apparent rate constant (moles of biotite m^{-2} s^{-1}) and q is the reaction order with respect to the activity of H^+. This is consistent with the general behaviour of other

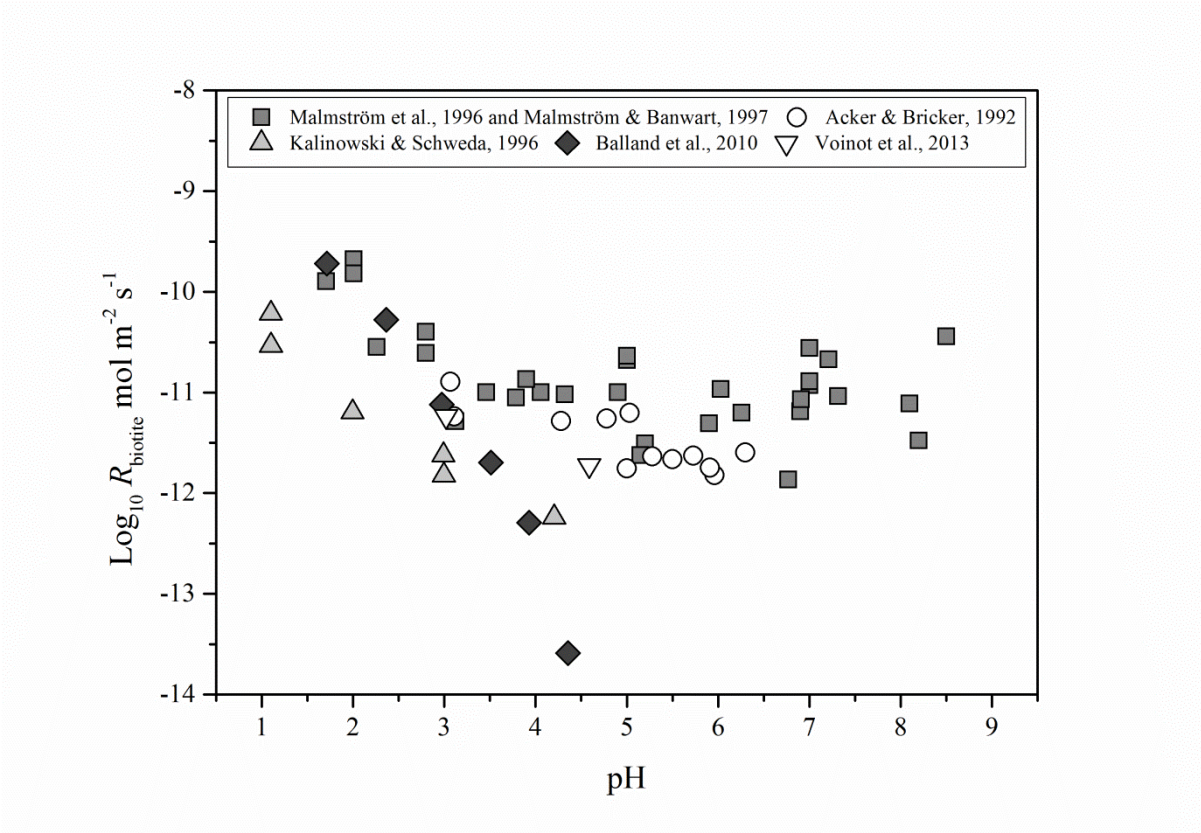

Figure 2.2

A compilation of experimental abiotic biotite dissolution rates as a function of pH from Acker and Bricker (1992), Malmström et al. (1996), Kalinowski and Schweda (1996), Malmström and Banwart (1997), Balland et al., (2010), Voinot et al. (2013).

phyllosilicates, as described by Nagy (1995) in a detailed review of phyllosilicate dissolution. However, what controls the variations in reported abiotic dissolution rates is poorly understood.

Biotite tends to dissolve non stoichiometrically. Stoichiometric release is when elements are released to the bulk fluid in the same mole ratios present in the mineral chemical composition. Potassium and other interlayer cations are released first due to ion-exchange reactions, as in phlogopite (Lin and Clemency, 1981; Turpault and Trotignon, 1994; Malmström and Banwart, 1997; Voinot et al., 2013). Interlayer cation release consistently has the fastest rate through the course of experiments as this reaction is diffusion-limited (Malmström and Banwart, 1997). Structural cation release also appears to be non stoichiometric which has been ascribed to the preferential

release/retention of certain ions in the solid phase, probably due to the speciation of surface sites, and/or the solubility of an ion with respect to the possible precipitation of a secondary phase (Lin and Clemency, 1981; Acker and Bricker, 1992; Turpault and Trotignon, 1994; Kalinowski and Schweda, 1996; Malmström and Banwart, 1997). It has been suggested that ions from the same structural sheet (i.e. tetrahedral or octahedral sheets) dissolve stoichiometrically (Acker and Bricker, 1992) but sheets do not necessarily dissolve stoichiometrically (Malmstrom and Banwart, 1997). However, it has also been shown that element release from the same sheet occurs at different rates (Turpault and Trotignon, 1994; Malmström and Banwart, 1997). This non-stoichiometric release leads to the formation of a surface dissolution front or transformed zone of biotite which, depending on pH and exposure period, can vary in depth and chemical composition (Malmström and Banwart, 1997; Voinot et al., 2013). Schnoor (1990) and Malmström and Banwart (1997) describe that this surface dissolution front forms first through the release of K^+ (Fig. 2.3), leaving the solid phase with approximately stoichiometric concentrations of structural elements. Subsequently, the front extends within biotite by the release of elements in the following order of rate K > Mg, Si, Al > Fe, until the release rate of K^+ decreases due to the greater diffusion pathway. At that point, the release rate of K is stoichiometric with Fe, while Mg, Si and Al continue to release at a higher rate, before gradually decreasing until stoichiometric dissolution occurs and the extent of the surface dissolution front does not change with time. Voinot et al., (2013) suggested that the extent of this surface front is pH dependent and occurs to a greater extent at lower pH, with interlayer cations being preferentially released. The significance of the existence of this surface dissolution front in biotite on the release of cations, both in laboratory and natural settings, is unclear.

Biotite, like other sheet silicates, is highly spatially anisotropic with the basal (0 0 1) and edge (*h k* 0) surfaces differing in reactivity by two orders of magnitude (Turpault

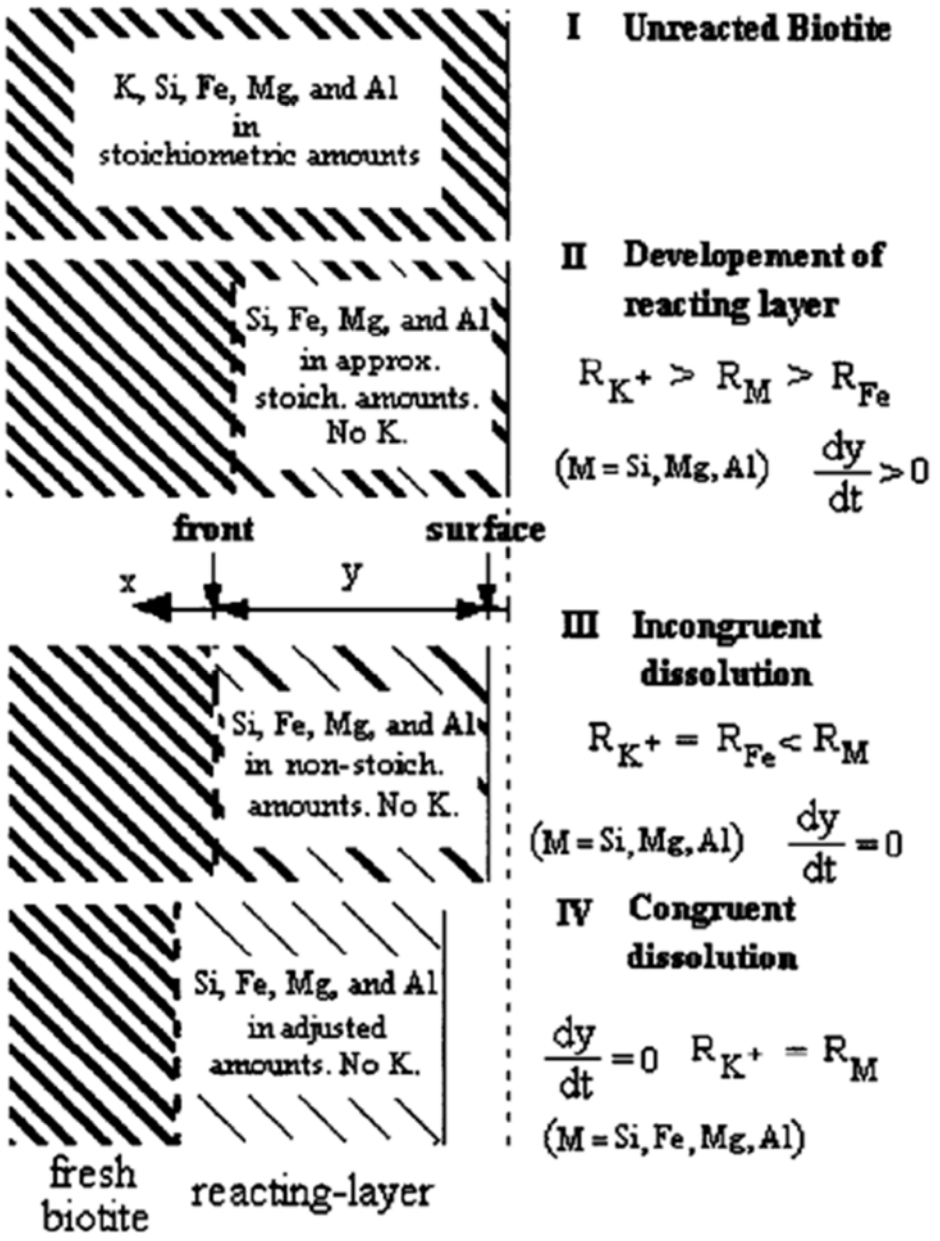

Figure 2.3

A one-dimensional conceptual model of biotite dissolution and surface dissolution front formation. From Malmstöm and Banwart, 1997.

and Trotignon, 1994; Bosbach et al., 2000; Hodson, 2006). The reason for this difference is due to the layered structure and the unsatisfied dangling bonds at the edges of crystallographic sheets (Turpault and Trotignon, 1994). Much work has been conducted using physical (atomic force microscopy, AFM) and optical (vertical scanning interferometry, VSI) approaches to quantify the basal (0 0 1) surface reactivity (Rufe and Hochella, 1999; Bosbach, et al., 2000; Bickmore et al., 2001; Bickmore et al. 2003;

Aldushin et al., 2006; Haward et al., 2011; Cappelli et al., 2013; Gazzè et al., 2014). Based on these studies, it was proposed that the main mechanisms for dissolution of the (0 0 1) surface is the formation and expansion of etch pits (e.g. Haward et al., 2011), and the retreat of surface edges (e.g. Cappelli et al., 2013). Both these mechanisms rely on the exploitation of defects in the mineral surface to promote dissolution of highly reactive areas, and are consistent with the model of biotite dissolution presented by Schnoor (1990), and Malmström and Banwart (1997). However, experimental constraints using AFM and VSI prohibited the derivation of information about the role and effect of mineral edge (*h k* 0) surfaces to element release. This information is still missing despite the fact that Turpault and Trotignon (1994), and Hodson (2006) showed that edge dissolution may be between 30 to 300 times more reactive than the basal (0 0 1) surfaces.

Furthermore, mineral dissolution rates are classically reported as the released moles of a mineral per mineral surface area per unit of time, with surface area either measured via gas adsorption method (BET, Brunauer et al., 1938) or estimated geometrically. Commonly dissolution rates are reported as normalised to an initial surface area, and changes in this parameter during the dissolution are often ignored. In addition, the ratio of the BET surface to the geometric surface area is referred to as the roughness factor (Wolff-Boenisch et al., 2004) and the roughness increases as a mineral dissolves (White and Brantley, 2003). The importance of these parameters for biotite dissolution has been investigated by Hodson (2006), who suggested that the initial BET surface area was the most appropriate for normalising laboratory determined dissolution rates as it best integrated the differences in dissolution rate and area for the basal (0 0 1) and edge (*h k* 0) sites. However, due to the control of edge sites on biotite dissolution, the final geometric edge surface area should be the normalising term when

comparing laboratory (either closed or open systems) and/or field-based biotite dissolution rates.

2. 3. CLOSED VS OPEN SYSTEM DISSOLUTION REACTIONS

There are two main experimental approaches for determining mineral dissolution rates: (i) closed-system experiments (batch reactor) and (ii) open-system experiments (mixed flow reactor, column reactor). A batch reactor is a closed stirred vessel which can be maintained at a constant pH (using buffers or auto-titrator) or changing (drift mode) pH, and can be open or closed to the atmosphere (Brantley, 2003) In closed-systems, dissolution rates are determined by measuring the concentrations of dissolution products as a function of time, correcting these concentrations for the removed solution volume and normalising to initial mineral surface area. Through the course of a batch reactor experiment the system progresses towards equilibrium and as products accumulate in solution the reaction slows. As a result, dissolution rates calculated from closed system experiments are often more difficult to interpret as it requires the consideration of a constantly changing solution composition and possible back-reactions (Oelkers et al., 2001). Furthermore, the duration of such an experiment is often limited due to the progression towards equilibrium.

In contrast, a mixed-flow reactor is a stirred reactor with a constant flow of fresh solution pumped in to the vessel at constant or changing pH. Reaction rates are determined by monitoring the chemical composition of the out-flow solution, and normalising concentrations to the flow rate of the system. Experiments are run until the outlet concentrations reach a steady-state value. The duration of open-system experiments (often many days to weeks) can lead to significant changes in mineral surface area which can be accounted for in the rate calculations by normalising to the final mineral surface area. However, it has been suggested that some phyllosilicates

never reach a steady-state dissolution rate due to the extent of surface area change through an experiment (Köhler et al., 2005). In general, the derivation of mineral dissolution rate is much more straightforward on open-system than closed-system experiments, yet closed-system experiments are far easier to carry out.

Discussion and description of rate calculations from closed and open system experiments can be found in chapter 3. Extensive summaries of different rate determining experimental approaches have been written by Brantley (2003) and Rimstidt (2013).

2. 4. MYCORRHIZAL FUNGI AND MINERAL WEATHERING

It is now widely accepted that the biosphere plays a significant role in mineral weathering and soil formation. Indeed, mineral weathering rates in vegetated soils are estimated to be 2 to 10 times faster than lithologically similar yet non-vegetated soils (Drever and Zobrist, 1992; Arthur and Fahey, 1993; Drever, 1994; Bormann et al., 1998; Moulton and Berner, 1998; Akter and Akagi, 2005). This increased weathering rate is assigned to the combined action of plants, mainly vascular plants, and soil dwelling microorganisms. In unsaturated soils plants tend to form symbiotic relationships with mycorrhizal fungi. Over 90% of plant families and 80% of tree species form these symbiotic mycorrhizal associations (Wand and Qui, 2006). In ectomycorrhizal fungi (EMF) associations, plant roots are completely sheathed with fungal mycelium, through which the majority of water and nutrients taken up by the plant pass through. EMF receive up to 30% of the net photosynthate of plants and extend mycelial networks into the soil to absorb and mobilise nutrients (Read et al., 2004) The vast mycelial networks form the largest biomass in boreal forest soils (Högberg and Högberg, 2002), where it is estimated that 1 kg of soil contains 100 km of mycorrhizal filaments (Whitfield, 2007). The mycorrhizal filaments, or hyphae, actively forage for nutrients in soil by acting as

biosensors distinguishing different grain size and mineralogy, operating at the scale of individual hyphae on individual mineral grains (Leake et al., 2008; Smits et al, 2008). Due to their great expanse, and direct link to solar energy via the photosynthesis of their host, mycorrhizal fungi have been suggested as the main agent of mineral weathering in soils (Landeweert et al., 2001).

Ectomycorrhizal fungi such as *Paxillus involutus* have been shown to mechanically force the crystal lattice of biotite (Bonneville et al., 2009) and create channels up to 3 μm wide and 15 nm deep the basal (0 0 1) surface of chlorite (Gazzè et al., 2012). This physical alteration occurs alongside the secretion of extracellular polymeric substances directly onto the mineral surface in the immediate surroundings of the growing hypha (Saccone et al., 2012; Gazzè et al., 2013), resulting in localised acidification and the removal of nutrients from the biotite structure, perpendicular to the basal (0 0 1) surface (Bonneville et al., 2011). The extent of element removal in the biotite structure by an individual hypha increases with exposure time, up to a maximum depth of 40 nm. The rate of mycorrhizal biotite weathering determined by Bonneville et al. (2011), on the (0 0 1) surface in unsaturated conditions, is comparable to bulk biotite dissolution rates into solution. However, the Bonneville et al. (2011) weathering rate is calculated using an assumed contact time and growth rate of mycorrhizal hyphae. The growth kinetics of fungi over any mineral surface are missing from the literature, and values of hyphal turnover in soils varies from 7 to 145 days (Staddon et al., 2003; Treseder et al., 2010). It is possible that fungal growth kinetics are influenced by atmospheric CO_2 concentrations (Andrews et al., 2010), as at higher pCO_2 plants are able to fix more carbon via photosynthesis which is the source of energy for mycorrhizal fungal activity. However, this effect has not been quantified. It has also been suggested that fungal tips are particularly important for the physical forcing and chemical alteration of the mineral

structure (Bonneville et al., 2009; Gazzè et al., 2012). However, it is unclear if these specific spatial functions of a hypha are reflected in the hypha's biochemistry.

2. 5. ORGANIC EXUDATES OF MYCORRHIZA

As mentioned above, one of the proposed mechanisms by which mycorrhiza fungi enhance biotite weathering is the secretion of organic compounds directly on the mineral surface. Indeed, fungi and soil dwelling bacteria are known to secrete both low molecular weight organic acids (LMWOA) and larger organic chelators such as siderophores (Lapeyrie et al., 1987; Jones, 1998; Renshaw et al., 2002; Ullman and Welch, 2002; Arvieu et al., 2004; van Hees et al, 2005; Adeyemi and Gadd, 2005; van Hees et al., 2006; Gadd, 2007; Buss et al., 2007; Balogh-Brunstad et al., 2008a; Balogh-Brunstad et al., 2008b; Grąz and Wilkołazka, 2009). The concentration of these organic exudates in the natural environment is highly variable, spatially and also at different scales. Citric acid and oxalic acid concentrations in bulk soil solution range from 10^{-5} to

Table 2.1

Amount of organic acids (mmoles L^{-1}) secreted by mycorrhizal fungi *Aspergillus niger*, *Serpula himantioides* and *Trametes versicolor* in the presence of apatite, galena and obsidian. From Adeyemi and Gadd (2005).

Rock type and nutrient state	Fungi	Acetic	Citric	Fumaric	Gluconic	Malic	Oxalic	Succinic (mM)
Apatite – glucose	*A. niger*	–	–	0.0007	–	0.67	0.01	–
	S. himantioides	–	–	–	–	0.23	0.33	–
	T. versicolor	–	–	0.004	–	0.52	0.01	–
Apatite + glucose	*A. niger*	–	–	–	–	0.64	2.21	–
	S. himantioides	–	–	0.002	–	0.59	1.91	–
	T. versicolor	–	–	0.0006	–	0.53	0.45	–
Galena – glucose	*A. niger*	–	–	0.0002	–	0.56	0.080	–
	S. himantioides	–	–	0.0005	–	0.59	0.130	–
	T. versicolor	–	–	0.0003	0.21	0.57	0.070	–
Galena + glucose	*A. niger*	–	0.19	–	0.39	0.29	0.010	–
	S. himantioides	0.01	0.57	–	–	0.64	0.540	–
	T. versicolor	–	0.64	0.001	–	0.46	0.003	–
Obsidian – glucose	*A. niger*	–	–	0.0060	–	0.77	0.0600	–
	S. himantiodes	–	–	0.0002	–	0.36	0.0004	0.02
	T. versicolor	–	–	0.0003	–	0.57	0.0100	–
Obsidian + glucose	*A. niger*	–	–	–	0.70	1.06	0.0100	–
	S. himantiodes	–	0.03	0.0035	0.15	0.30	–	–
	T. versicolor	–	–	0.0010	0.91	0.79	0.0040	–

The figures shown are mean values of three replicates and were calculated by comparing the values derived with the retention times of the different organic acid standards of known concentrations.

10^{-6} moles L^{-1} (Jones, 1998; Ullman and Welch, 2002). Liquid medium cultures of ectomycorrhizal fungi in phosphorus limiting conditions produced 10^{-6} to 10^{-7} moles L^{-1} of oxalic acid (Arvieu et al., 2003). However, it is likely that concentrations of organic acids are significantly higher at the contact zone between fungi and minerals. Indeed, Adeyemi and Gadd (2005) determined the concentration of common organic acids surrounding fungi in mineral-rich agar medium interactions were up to 10^{-3} moles L^{-1} (Table 2.1). Similarly, aqueous concentrations of siderophores in soil solutions are estimated to range from 10^{-5} to 10^{-3} (Hersman et al., 1995; Kalinowski et al., 2000). The disparity in the concentrations reported by these studies is a primarily a result of the methods used. Concentration is obviously controlled by solution volume, however there is no standard method for determining organic acid or ligand production by microorganisms and the volumes of solutions used varies greatly (see references above). Rather than referring to concentration, a more appropriate unit for reporting organic ligand production would be moles of organic ligand per gram of organism biomass. In natural systems where there is minimal solution, for example at the fungi-mineral interface, concentrations of organic acids and other organic ligands could well be much greater than those reported previously (Bonneville et al., 2009; Bonneville et al., 2011; Saconne et al.,2012; Gazzè et al., 2013). *In situ* pH measurements around fungal hyphae have shown a dramatic decrease (from 6.5 to below 4.6) when fungi were in contact with biotite surfaces (Bonneville et al., 2011) which is a product of organic acid production and fungal respiration.

The predominant organic acids secreted by microorganisms in soils have carboxylic acid groups which can be protonated or deprotonated as a function of pH. Following deprotonation the resulting anions readily adsorb to mineral surfaces and form soluble and insoluble complexes with mono-, di-, and tri-valent metal cations, discussed further below. The most common groups of siderophores secreted by

microorganisms are hydroxamates and catecholates, which are secreted into the soil in response to Fe limitation (Winkelmann, 1991; Bergeron and McManis, 1991). Siderophores are powerful chelators of $Fe^{(III)}$ but are also able to chelate other di- and tri-valent metal ions such as Al (Borgais et al., 1989; Kalinowski et al., 2000; Brantley et al. 2001; Saha et al., 2012).

The effect of organic ligands on mineral dissolution is complicated because even the simple interactions between LMWOA and metals/metalloids at different pH values, or how LMWOA and mineral surfaces interact are poorly understood. In a number of cases the presence of organic ligands enhances the dissolution of *silicates* (Huang and Kiang, 1972; Barman et al., 1992; Welch and Ullman, 1993; Drever and Stillings, 1997; Ullman and Welch, 2002; Cama and Ganor, 2006; Neaman et al., 2006; Golubev et al., 2006; Buss et al., 2007; Wolff-Boenisch and Traina, 2007a; Pokrovsky et al., 2009; Kiczka et al., 2010; Balland et al., 2010; Ramos et al., 2011; Voinot et al., 2013), *oxides* (Hersman et al., 1995; Holmén and Casey, 1996; Kraemer et al., 1999; Cocozza et al., 2002; Cheah et al., 2003; Rosenberg and Maurice, 2003; Kraemer 2004; Reichard et al., 2007; Wolff-Boenisch and Traina 2007b; Simanova et al., 2010) and *sulfides* (Cornejo-Garrido et al., 2008). In the acidic range the effect of organic acids on dissolution kinetics is modest, the enhancing action of LMWOA becomes significant as pH enters into the slightly acidic and circumneutral ranges (Welch and Ullman, 1993). Dissolution enhancement is also assumed to be organic ligand concentration dependant, with a suggested threshold of 10^{-3} moles L^{-1} required for a significant effect (i.e. doubling) on the dissolution rate of smectite and wollastonite to occur (Golubev et al., 2006; Pokrovsky et al., 2009). In some cases (e.g. for forseterite) the effect of organic ligands on cation release is negligible even at a large range of concentrations (Declerq et al., 2013). However, negligible solution based evidence does not mean that no effect of organic ligands. Loring et al. (2008) presented that under certain conditions, in the absence of increased dissolved Fe

concentrations, $Fe^{(III)}$-oxalate complexes readsorb to the mineral surface, creating a highly mobile pool of Fe.

There are two mechanisms by which organic ligands are suggested to enhance dissolution, surface adsorption and cation complexation (Drever and Stillings, 1997; Cheah et al., 2003; Buss et al., 2007). Adsorption of a ligand to a mineral surface depends on its aqueous speciation as well as on the surface charge and speciation (Kubicki et al., 1997; Ullman and Welch, 2002) As mentioned above, ligands change their speciation as a function of pH. If the dominant dissolved ligand species is neutral or has the same charge as the mineral surface, the ligand will tend to be repelled by electrostatic forces, inhibiting adsorption (Morel and Hering, 1993). Once adsorbed to metal surface sites, ligands disrupt the metal ion's lattice bond strengths, weakening the structure. Organic ligands are also able to act in solution by enhancing the chemical affinity of a system. Ligands complex with dissolved cationic species, shifting the system away from equilibrium, therefore allowing dissolution reactions to progress faster (Wolff-Boenisch and Traina, 2007a). As with surface adsorption, the speciation of a dissolved ligand species will determine their ability to form complexes with dissolved metal cations. This effect is most likely to be evident in closed-system or poorly mixed open-system experiments as these may approach equilibrium with respect to the primary or a secondary phase.

There is currently very little data on the effect of organic ligands on the dissolution of biotite. Particularly on the mechanism by which LMWOA and siderophores interact with the biotite in solution. This information is important for understanding the how organic exudates contribute to fungal mineral weathering in the natural environment.

2. 6. SUMMARY

There are several areas of the literature which currently lack the data to aid our understanding of the biological mineral weathering, and its importance in the natural environment. Firstly, it is currently unclear how mycorrhizal fungi liberate nutrient elements from biotite. To address this we need a greater understanding of what controls element release from biotite in abiotic systems, and to link to fungal weathering, quantify if and how known organic exudates contribute positively to the bio-weathering process.

Secondly, mycorrhizal fungi respond to the presence of nutrients by colonising mineral surfaces and extracting nutrients. It has been suggested that specific sections of hyphae have particular functions in the weathering process. It is unclear what controls this functionality and if it is reflected in spatial changes in biochemistry of the organism.

Finally, for a greater understanding of the soil system, micron-scale biological mineral weathering processes need to be applied to a variety of scales and climatic conditions. This requires a robust quantification of bio-weathering processes, which are currently limited by a lack of accurate fungal growth rates and mechanisms.

The following chapters describe the work I have completed to attempt to plug these knowledge gaps.

Chapter 3. Methods

In this chapter, the experimental and analytical methods used in this thesis are described. There is some overlap with descriptions in the results chapters, yet here in many cases details area also given about the theoretical aspects related to some of the methods. This is done to ensure the results chapters are internally consistent and can be read alone. The methods described in this chapter include information about the characterisation of the biotite samples used this thesis. Described are methods to assess the chemical composition, mineralogical purity and geometric properties of the biotite (section 3.1). This is followed by a description of the experimental approaches used in the potentiometric, electrokinetic and dissolution experiments (section 3.2), which is accompanied by the methods used for solution analysis in the solution based experiment (section 3.2). Furthermore, a description of how the solution data was processed to calculate dissolution kinetics, and how geochemical modelling was used to address observations from the solution based experiments (section 3.4) Finally, sections 3.5, 3.6 and 3.7 of this chapter, provide details about the plant-fungus experimental microcosm, the fungal growth experiments and details about the infrared spectroscopic methods used in evaluating biochemical changes during fungal growth across biotite surfaces.

3. 1. MINERAL CHARACTERISATION

For the interpretation of results in chapters 4 and 5 it is important to determine the chemical composition and characteristics of the mineral phases present at the start and end of experiments. The following sections describe the origin of the two biotite samples and outline the techniques used and methods in their chemical and physical characterisation.

3. 1. 1. Mineral samples

Two biotite samples were used in this thesis, the Grasåsen biotite (chapters 4 and 5) and the Moen biotite (chapters 5 and 6). The Grasåsen biotite, originated from the Grasåsen feldspar quarry, Moen, Arendal, Aust-Agder, Norway, and was provided by the Agder Naturmuseum, Kristiansand. The Moen biotite, originally from Moen, Norway, was obtained from Krantz, Bonn (sample X01481).

3. 1. 2. Electron microprobe analysis (EMPA)

Both mineral specimens were characterised using similar methods. The Moen biotite sample has already been described in an publication before my thesis (Bonneville et al., 2009). Only those analyses of the Moen since that publication are outlined below.

A polished block of the Grasåsen biotite was imaged by scanning electron microscopy (SEM) to identify and characterise the biotite and identify areas of inclusions and alteration using backscattered electron emission (BSE) and energy dispersive X-ray spectroscopy (EDX). The instrument used was a Field Emission Gun Scanning Electron Microscope (FEG-SEM) FEI Quanta 650 equipped with an Oxford X-Max silicon drift detector (SDD) and operated at 20kV. As the electron beam is pointed at a sample some electrons are reflected, or backscattered, following interactions with atoms in the specimen. The intensity (amount of electrons) of backscattering is dependent on the atomic mass of the atom; therefore areas with atoms of high atomic mass appear brighter than atoms with low atomic mass. EDX measures the X-rays emitted from a sample which has been excited by an electron beam. The X-rays emitted are characteristic to elements present in the sample. Combined, these two techniques give an indication of areas of different chemical composition within a sample.

The bulk chemical composition of the Grasåsen biotite was determined by electron microprobe analysis (EMPA) of the polished block using a Jeol JXA-8230 microprobe running with a tungsten source at 15 kV and 15 nA. The electron microprobe allows the determination of chemical composition by measuring the X-rays emitted by a sample that

is being bombarded with an electron beam. The inner shell electrons of elements are ejected and replaced by outer-shell electrons while emitting X-rays at energy levels characteristic of each element. With calibration, an electron probe allows the determination of element abundances in a mineral sample. In the case of the Grasåsen biotite, the electron microprobe was calibrated for each element using in-house standards. Si, Mg and Ca were calibrated with diopside, Fe with haematite, Al with kyanite, K with K-feldpsar, Ti with rutile, Mn with rhodonite, Cr with chromite, and Na with jadeite. 40 areas of the biotite, identified using BSE and EDX, were analysed and provided chemical composition expressed in percentage oxide weights (wt. %), with a theoretical quantity of H_2O having been added and assuming all Fe present in the sample was $Fe^{(II)}$. Of the 40 point measurements, 15 had a cumulate oxide wt. % between 99.1 and 100.9, from which the elemental concentrations were calculated, normalised to $O_{10}(OH)_2$ formula units. The average composition of the Grasåsen biotite was calculated from the elemental concentrations of the 15 point measurements and is presented in Table 5. 1, Chapter 5, along with the chemical composition of the Moen biotite which was previously determined following the same method and described in Bonneville et al. (2009). EMPA, BSE, and EDX are all non-destructive analytical techniques.

3. 1. 3. X-ray fluorescence (XRF)

A crushed portion of the Grasåsen biotite was also analysed by X-ray fluorescence (XRF) using an Olympus Innov-x X-5000 portable XRF at 10kV. X-Ray fluorescence is a non-destructive technique which characterises the chemistry of a sample using a similar principle to EDX and EMPA (see 3.1.2). Analysis of the Grasåsen sample was performed using beam 2 of the 'Mining Plus' mode which provides concentrations in wt. % of Si, P, K, Ca, Ti, Mn, and Fe. This method was used primarily to determine the amount of Calcium present in the powdered sample of biotite. The Olympus Innov-x X-5000 portable XRF is unable to provide accurate data on elements with low molecular weights, < ~28 g mol^{-1}, these lighter elements are reported as LE (light elements). The accuracy of this method for

elements with higher molecular weight was tested by analysing the Natural Resources Canada certified reference material, STSD-1 to STSD-4: Stream Sediment yielding a maximum uncertainty of 3.75%.

3. 1. 4. X-ray diffraction (XRD)

X-ray diffraction is a non-destructive which uses an X-ray beam to analyse minerals, revealing their internal lattice structures. The principle of XRD relies on the repetitive nature of crystal structures for determination of sample characteristics. A crushed sample of the Grasåsen biotite was analysed using a Bruker D8 X-ray powder diffractometer with a scan range from 5° to 75° 2θ and a step size of 0.009° 2θ to give an indication of sample purity but also to identify possible impurities in the bulk mineral sample. The obtained spectra was Reitveld refined using the software code Topas (version 4.2, Bruker AXS) and fitted with phases from the biotite solid-solution series, as well as quartz and carbonates as major impurities.

3. 1. 5. Biotite sample preparation for solution-based experiments

Both the Moen and Grasåsen biotite samples were crushed, separately, using a jaw crusher, pestle and mortar, ball mill, and agate disk mill, removing visible inclusions throughout the process. The crushed biotite samples were subsequently sieved to obtain the 75-150 μm (Moen), and 25-53, 53-180 and 180-500 μm (Grasåsen) size fractions. Each size fraction was then repeatedly washed by sonication and gravitational settling using 18.2 MΩ water, and dried at 40 °C for 48 hours. The lower limit of the 25-53 μm size fraction was calculated using Stokes' law during the gravitational settling stage, using an average biotite density of 3.09 g cm^{-3} (webmineral.com). These size fractions were used in open and closed system experiments described in chapter 5.

A portion of the 25-53 μm size fraction was crushed further by agate mill for use in the electrokinetic measurements and potentiometric titrations presented in chapter 4,

because these techniques require samples with a much larger surface area. The resulting size fraction was submicron to 10 μm.

3. 1. 6. Geometric surface area evaluations through imaging

The 75-150 μm (Moen), and 25-53, 53-180 and 180-500 μm (Grasåsen) size fractions described above were imaged using FEG-SEM (see 3.1.2) However, for the purpose of evaluating the geometries of the biotite particles the FEG-SEM stage was tilted to an angle of 45°. It is worth noting that this technique only works if particles are flat on the SEM stub. By using the stage at an angle the dimensions of both the (0 0 1) basal plane and the lateral or edge (*h k* 0) surfaces perpendicular to the (0 0 1) can be measured. The size of a representative population sample was calculated to be 18, 47, 48, and 25 for the 75-150, 25-53, 53-180, and 180-500 μm respectively, based on a 95% confidence level. To calculate the length of a two dimensional vector v_i (*x, y*), Pythagoras informs us that

$$v_i = \sqrt{(v_x^2 + v_y^2)}$$

Eq. 3.1

where v_x and v_y are the *x* and *y* dimensions to the vector *v* separated by 90° on a 2 dimensional plane. In the scenario of a 2 dimension vector (*x, y)* in a 3 dimensional space, such as a FEG-SEM stage angled at 45° dipping away from the viewer looking into the *z* dimension, the *x* dimension of the vector will be unaffected. However, the *y* dimension will be affected and the apparent *y* dimension (v'_y) can be converted to v_y by

$$v_y = \frac{v'_y}{\cos\theta}$$

Eq. 3.2

where θ is the angle of the stage and the scenario is representative of Fig. 3. 1A. Using this method to calculate the length of vectors a, b and c in Fig. 3.1B, the surface areas of the (0 0 1) basal surface (2ab, SA_{basal}, %) and (*h k* 0) edge surface (2ac + 2bc, SA_{edge}, %) of measured grains, and geometric specific surface area (SSA_{geo}, $m^2\ g^{-1}$) can be calculated:

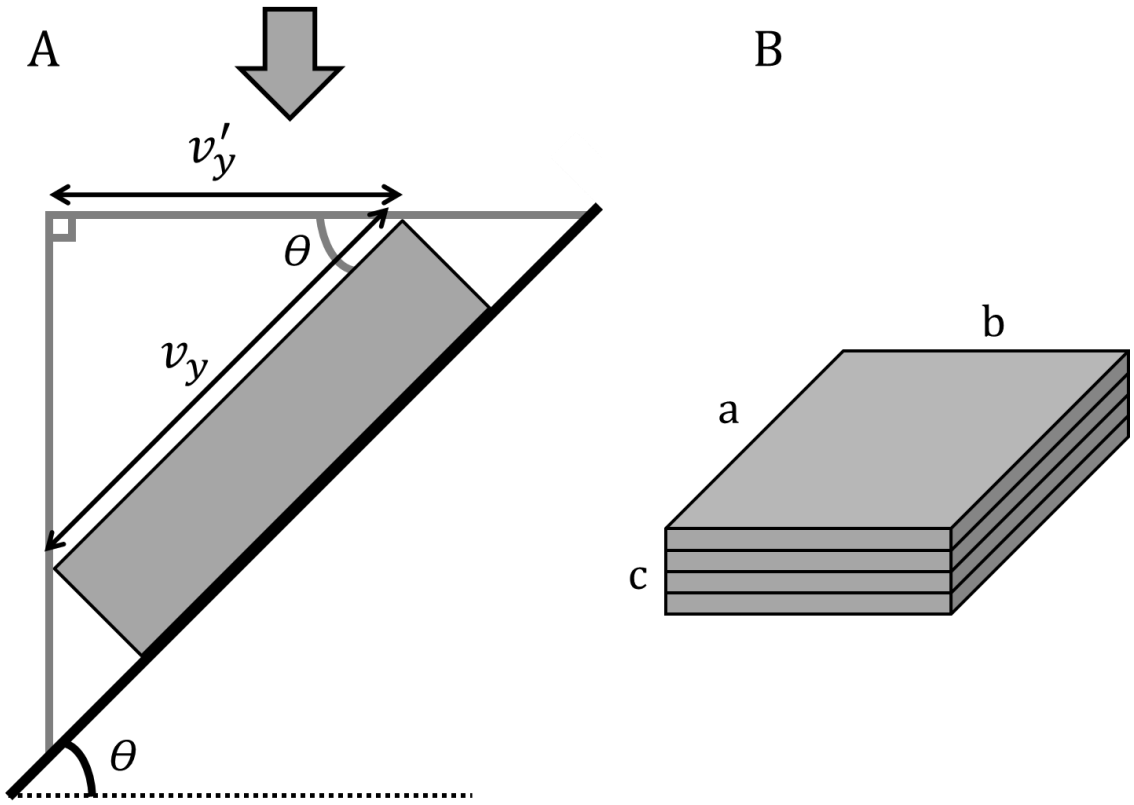

Figure 3.1

Schematics of (A) the angles and trigonometric system of a FEG-SEM stage at angle θ; and (B) the geometry of a biotite flake with dimensions a, b, c.

$$\mathrm{SA_{basal}} = \frac{2\mathrm{ab}}{2\mathrm{ab} + 2\mathrm{ac} + 2\mathrm{bc}} \times 100$$

Eq. 3.3

$$\mathrm{SA_{edge}} = \frac{2\mathrm{ac} + 2\mathrm{bc}}{2\mathrm{ab} + 2\mathrm{ac} + 2\mathrm{bc}} \times 100$$

Eq. 3.4

$$\mathrm{SSA_{geo}} = \frac{(4\mathrm{AC} + 2\mathrm{AB})}{\rho_{\mathrm{biotite}} \cdot \mathrm{ABC}}$$

Eq. 3.5

where a, b and c are biotite grain dimension measured via FEG-SEM; A, B and C are the average dimension of an ideal biotite grain of a cuboid shape, where the A and B dimensions are equal in length and that length is governed by the mid-point between the limits of each size fraction e.g., A = 39 μm for the 25-53 μm size fraction. The C dimension is the average of the c measurements for a given size fraction. The term ρ represents the

average density of biotite (3.09, webmineral.com). The geometric surface area terms SA_{basal}, SA_{edge} and SSA_{geo} are used in chapter 5.

3. 1. 7. Specific surface area (SSA) quantification

Another method of quantifying the specific surface area of a sample is by the gas adsorption method described by Brunauer et al. (1938). This method, called the BET (Brunauer-Emmet-Teller) specific surface area (SSA_{BET}, $m^2\ g^{-1}$) is calculated by determining the volume of gas adsorbed on the surface of a solid and then calculating the area this represents by using an assumed projected cross section of an adsorbed gas molecule. The volume of gas adsorbed can be determined using an adsorption isotherm, described by Brunauer et al. (1938):

$$\frac{1}{\mathrm{v}\left[\left(\frac{p_0}{p}\right)-1\right]} = \frac{c-1}{\mathrm{v}_m c}\left(\frac{p_0}{p}\right) + \frac{1}{\mathrm{v}_m c}$$

Eq. 3.6

where p and p_0 are the equilibrium and saturation pressures, v the volume of adsorbed gas, v_m the monolayer adsorbed gas quantity and c the BET constant. Plotting Eq. 3.6 with $1/v\ [(p_0/p) - 1]$ against p/p_0 gives a straight line ($0.05 < p/p_0 < 0.35$) with gradient A and intercept I which can be used to calculated v_m:

$$\mathrm{v}_m = \frac{1}{A + \mathrm{I}}$$

Eq. 3.7

from which we can calculate SSA_{BET}:

$$\mathrm{SSA_{BET}} = \frac{(\mathrm{v}_m N \mathrm{s})}{\mathrm{V} \cdot m}$$

Eq. 3.8

where N is Avogadro's number, s the projected cross section of adsorbing gas, V the molar volume of adsorbing gas, and m the mass of adsorbent, or solid sample. These calculations were used to determine the SSA_{BET} of the size fractions described in section 3. 1. 5.

The SSA_{BET} of the 25-53, 53-180, 180-500 μm (Grasåsen) and 75-150 μm (Moen) size fractions were measured via a 9 point N_2 adsorption isotherm between 0.05 and 0.25

p/p_0 at 77 K using a Micromeritics Gemini V analyser. Samples were degassed with N_2 for 20 hours before analysis and SSA_{BET} was calculated based on an assumed cross section of adsorbed N_2 of 0.162 nm^2. Replicate measurements of 76 sub-samples of the 53–180 μm size fraction yielded a relative standard deviation (RSD) of 4.6%. These SSA_{BET} values are used in chapter 5. The accuracy of this technique was routinely determined through the measurement of the Micromeretics Surface Area Reference Material, black carbon. Results were consistently within the range of specific surface area acceptable for the standard, 21.0 ± 0.75 $m^2\ g^{-1}$.

The SSA_{BET} of the submicron to 10 μm size fraction was determined via an 11 point krypton adsorption isotherm between 0.046 and 0.30 p/p_0 at 77 K using a Quantachrome AUTOSORB-1. Samples were degassed with Kr at 120 °C for 23 hours before analysis and the surface area was calculated based on an assumed cross section of adsorbed Kr of 0.205 nm^2. The SSA_{BET} for the < 10 μm size fraction is used in chapter 4.

3. 2. EXPERIMENTAL SETUP AND SOLUTION BASED MEASUREMENTS

The experiments described in the following section outline the methods used to understand the mechanisms by which biotite reacts with an aqueous fluid phase. Sections 3. 2. 1 and 3. 2. 2 outline the experimental approaches used to characterise biotite surface in solution (chapter 4); sections 3. 2. 3 and 3. 2. 4 outline the experimental approaches employed to quantify the dissolution kinetics of biotite (chapter 5).

3. 2. 1. Batch potentiometric titration

A batch potentiometric titration series is a collection of time limited, mineral-bearing batch experiments performed at a constant temperature and ionic strength with varying concentrations of H^+, covering a range of pH (e.g. Pokrovsky et al., 1999; Chaïrat et al., 2007; Oelkers et al., 2009). During the mineral-fluid reactions, protons are consumed by a combination of element release from the mineral, hydrolysis and adsorption processes. By measuring the pH of a batch reaction after a predetermined period of time, and measuring the concentrations of dissolved elements, it is possible to calculate the net proton consumption of each of the above mentioned processes. Performing a time-limited but pH dependent series of batch reactions allows the reconstruction of a potentiometric titration with the added ability of monitoring changes in the solution chemistry as a function of pH. These experiments were conducted to quantify the pH of zero net proton charge (pH_{ZNPC}) of the biotite surface and to also characterise the changes in element release and proton consumption through the pH range. The experiments are described in detail in chapter 4 where corresponding theoretical calculations of proton consumption by the various processes are also given.

In brief, 20g/L of biotite was equilibrated while stirred in a polypropylene reactor with a NaCl electrolyte of known ionic strength (I) for at least 12 hours under a N_2 atmosphere (5.0 grade, < 0.00001% impurity). Batch reactions were performed by mixing ~7 mL aliquots of this pre-equilibrated biotite suspension with a known quantity of analytical grade HCl or NaOH in 15ml polypropylene vials. Experiments were conducted

under a N_2 atmosphere, for either 20 or 60 minutes and were shaken constantly at 140 rpm, with addition manual shaking every 10 minutes. At the end of each titration experiment, the pH in each vial was measured using a Metrohm 713 pH Meter, calibrated with certified reference buffer solutions of pH 4.005, 6.866, and 9.183 (CertiPUR, Merck) at 25 °C.

A control titration series was obtained through otherwise identical experiments using biotite-free fluids, i.e., using the pre-equilibrated biotite suspension but with the biotite removed by filtered through a 0.2 μm cellulose acetate Nalgene filter unit. The control titration series was performed to determine a baseline for data interpretation.

Full details of all biotite-bearing and biotite-free batch titration experiments can be found in Tables A-1 and A-2, respectively, in Appendix A. Details include mineral suspension concentration, fluid ionic strength, experiment duration, suspension volume, and titrant concentration at the start of the experiment; and, pH and fluid composition at the end of each titration.

3. 2. 2. Electrokinetic measurements

Electrokinetic measurements are another method of evaluating the zero point of charge (pH_{ZPC}) of a mineral through the determination of its zeta-potential (ζ-potential, mV) via measurements of electrophoretic mobility. Particles in solution are surrounded by ions, H^+, OH^-, and other constituent ions, forming the electrical double layer (DL). The DL consists of a first layer or adsorbed ions (stern layer) and a second layer of loosely associated ions, the outer edge of which is referred to as the slipping plane. Zeta-potential is the electric potential between the fluid in the stationary DL layer of a particle and the disperse solution and is calculated from the electrophoretic mobility using the Schmoluchowski equation (Hunter, 1989). The ζ-potential is influenced by pH and ionic strength (Fig. 3.2). Changing the pH of a solution changes the net charge in the DL and therefore the ζ-potential. Ionic strength changes the absolute value of ζ-potential at a given pH because solutions of different ionic strengths have different electric potentials. The –ζ-

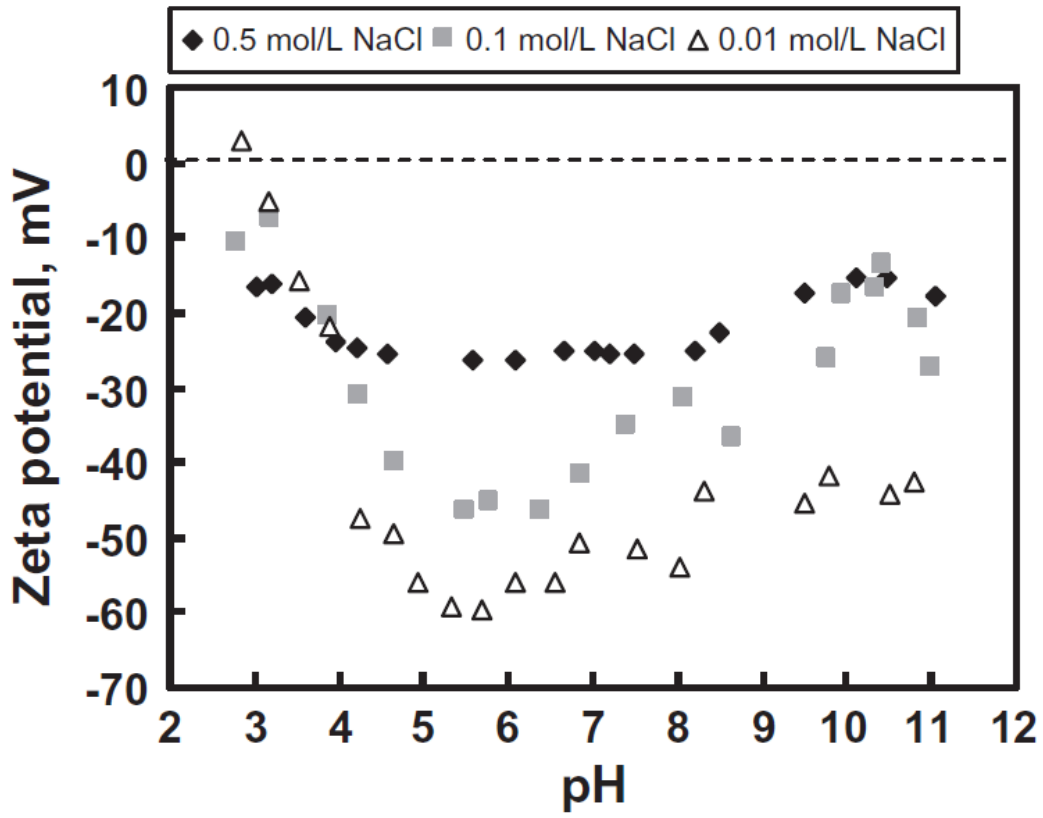

Figure 3.2

An example of ζ-potential data. This plot shows the ζ-potential of live *R. steppense* A-20s cells as a function of pH and ionic strength, from Bundeleva et al. (2011). Note the effect of ionic strength on measured ζ- potential.

potential decreases in intensity with increasing ionic strength, however, ζ-potential curves over a range of ionic strengths should converge at the point of zero ζ, or the isoelectric point (pH_{IEP}). Electrokinetic measurements were performed to determine the net surface charge of biotite to be used in conjunction with the batch potentiometric titrations. This experiment is described in chapter 4 along with a discussion of various points of zero charge.

The electrophoretic mobility of the biotite powder samples was measured at 25°C using a Zetaphoremetre IV, model Z3000 microelectrophoremeter with a dielectric constant of 80 ±1 V. For each measurement, biotite powder was added to individually prepared aqueous NaCl or HCl solutions (I = 10^{-1} to 10^{-3} M) with pH from 1 to 12 and measured within 5 minutes by electrophoresis. As in the batch titrations, the pH range for electrophoretic measurements was attained through the addition of analytical grade HCl

or NaOH. The pH of each fluid sample was measured externally during electrophoresis. Zeta-potentials calculated by the Schmoluchowski equation (Hunter, 1989) are presented in Table A-3 in Appendix A, along with the details of solutions used for electrophoretic measurement.

3. 2. 3. Closed-system dissolution experiments

Closed-system dissolution experiments were conducted to monitor the release of elements during the initial stages of dissolution, expanding the timeframe of the batch potentiometric titrations of (chapter 4). A comparison of closed- and open-system reactors for studying mineral dissolution is outlined in section 2.3 of chapter 2.

Biotite was reacted with solutions of ionic strength 0.01 M in high density polyethylene (HDPE) bottles (Nalgene) at 25 ± 1 °C, maintained by a shaking incubator at a rotation rate of 140 rpm. Bottles were inverted a minimum of every hour for the duration of the 12 hour experiment. Experiments were started by adding 1-2 g of crushed biotite to 1 L of reaction solution and samples were taken with decreasing frequency over the course of the experiment. Reaction solutions were prepared using solid $CaCl_2$ (AnalaR NORMAPUR, VWR) or Potassium Hydrogen Phthalate (KHP, CertiFied AR, Fisher) at an ionic strength of 0.01 M in 18.2 MΩ water and HCl/NaOH (Aristar/AnalaR NORMAPUR, VWR) to fix the pH. KHP was used as a background electrolyte to fix the ionic strength and buffer the pH as initial experiments showed a strong pH buffering ability of the Grasåsen biotite.

Details of the 91 closed-system biotite dissolution experiments can be found in Table 5. 3. Experiments were conducted using reaction solutions containing 500 μmoles/L of organic ligand (either citric acid, DFOB or oxalic acid) from pH 2 to 6 with an average pH variation of ± 0.08 pH units (based on average of 2σ of pH for each experiment, 95% confidence). Samples were filtered through 0.2 μm polyethersulfone filters (Sartorius) and quenched in 3% HNO3 (Aristar, VWR), HCl (Aristar, VWR) or NaOH (AnalaR NORMAPUR, VWR) depending on analysis. Experiments were halted by siphoning off remaining

reaction solution after centrifugation and reacted biotite powder was recovered for subsequent imaging and analysis.

3. 2. 4. Open-system dissolution experiments

Open-system dissolution experiments were conducted to quantify the steady state element release rates during biotite dissolution. These experiments were conducted with different apparatus for the Moen and Grasåsen biotite samples but the principle is the same. By feeding in fresh fluid at a consistent and continuous rate the system is maintained at a steady state. In this study, steady state iss defined by the outlet fluids maintaining a constant concentration of Al, Fe, Mg, and Si, within 5% (analytical and experimental uncertainty) for a minimum of 3 residence times (reactor volume/flow rate). The two experimental setups are described below. Details of the experiments can be found in table 5. 4.

The Moen biotite was reacted with a $CaCl_2$ solution of 0.01M ionic strength at pH 3.3 in a 300 mL titanium Parr™ mixed-flow reactor with continuous pH monitoring and controlled temperature, pressure and stirring, as described previously (e.g. Wolff-Boenisch et al., 2004). Briefly, 3 to 6 g of the 75-150 μm biotite size fraction was added to the reactor and stirred at 400 rpm and was allowed to react for up to 260 hours with solution continuously pumped through the reactor by a high performance liquid chromatography pump (HPLC) at flow rates between 0.07 and 0.13 L h^{-1}. At the system outlet the fluid passed through a 2 μm titanium filter and was further filtered using 0.2 μm polyvinylidene fluoride (PDVF) Whatman™ filters before being collected in acid washed HDPE sample bottles. Solution samples were acidified with HNO_3 (Aristar, VWR), solid samples were recovered after centrifugation and were subsequently dried.

The Grasåsen biotite was reacted in solutions of pH 2 to 4 at an ionic strength of 0.01 M, fixed using NaCl or KHP. Experiments were conducted in 35 mL Teflon mixed flow reactors and were continuously stirred with floating Teflon magnetic stir-bars (Fig. 3.3). The reactors consisted of identical base and head compartments holding the reactor

chamber together by threaded connection. Material was kept in the reactor chamber by placing 0.45 μm GN-6 Metricel MCE membrane filters at the connection of the reactor chamber with the base and head compartments (Fig. 3.3). The reactors were submersed in a water bath at a constant temperature of 25 ± 1 °C and solutions were input to the reactors by peristaltic pump at rates from 0.1 to 0.6 g/min. The pH of the inlet and outlet solutions was measured using a Metrohm 713 pH Meter, calibrated with certified reference buffer solutions of pH 4.005, 6.866, and 9.183 (CertiPUR, Merck) at 25 °C. pH measurement precision was 0.02 pH units.

3. 3. ANALYTICAL METHODS FOR DISSOLVED SPECIES

The chemistry of the solution sampled during the experiments outlined in section 3. 2 was analysed using a number of techniques, outlined below.

3. 3. 1. Inductively Coupled Plasma Mass Spectrometry (ICP-MS)

The concentration of a selection of dissolved elements in the solution samples was analysed using Inductively Coupled Plasma Mass Spectrometry (ICP-MS). This instrument ionises the sample before it is passed into a mass spectrometer where ions are separated based on their atomic mass. All calibration standards were made in the same matrix as the samples (i.e. NaCl and HNO_3) and blind samples of known concentration standards, as well as experimental and analytical blanks were included in each set of analysis, to evaluate precision and accuracy of the analyses and to aid interpretation and reliability of the experimental results.

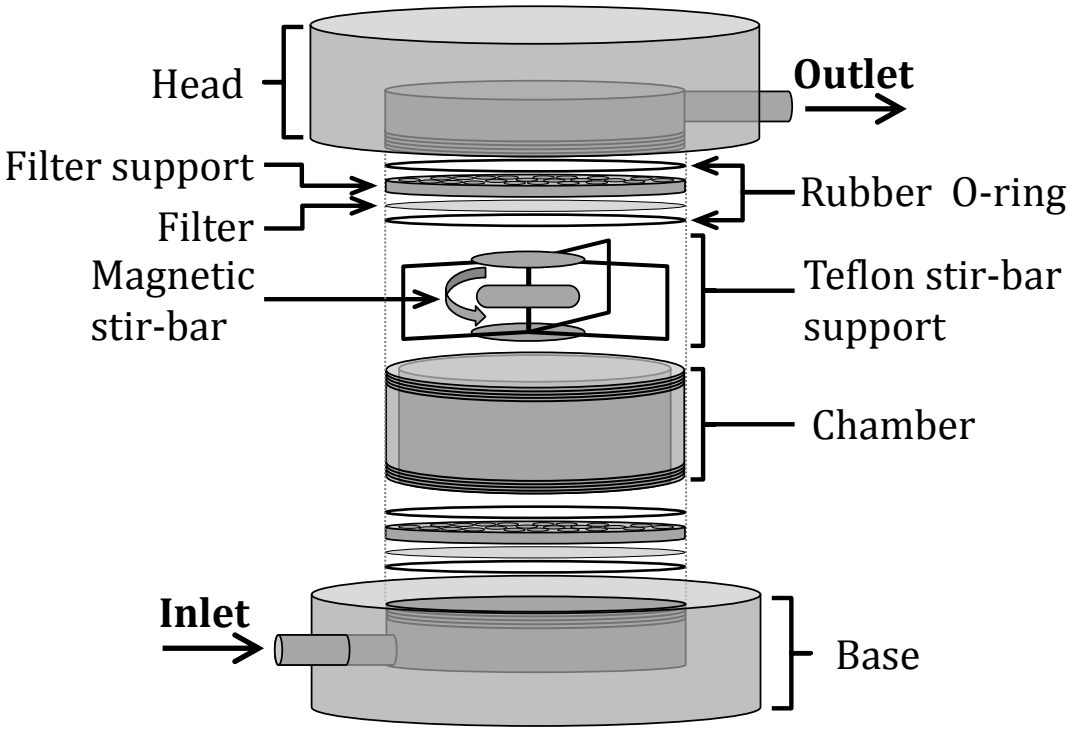

Figure 3.3

Schematic of the 35 mL Teflon reactor used in the open-system Grasåsen dissolution experiments.

Samples from the batch potentiometric titration experiments (3. 2. 1) were analysed for dissolved concentrations of Na, Mg, Al, K, Ca, Ti, Cr, Mn, and Fe using a Thermo Agilent 1700C ICP-MS. The limit of quantification for Na, Mg, Al, K, Ca, Ti, Cr, Mn, and Fe, determined from calibration curves, was 2.4, 1.2, 0.8, 4.1, 1.6, 1.1, 1.2, 1.1, and 1.3 μg kg^{-1} respectively. The average analytical uncertainty for Na, Mg, Al, K, Ca, Cr, Mn, and Fe, measured against the SLRS-5 certified reference material (National Research Council Canada) was 7.6, 5.1, 1.2, 4.4, 7.6, 10.1, 17.2, and 1.9% respectively.

Samples from the closed-system dissolution experiments (3. 2. 3) were analysed for dissolved Al, Fe, Mg and Si concentrations using an Agilent 7500ce ICP-MS with an integrated auto-sampler (I-AS). The limit of quantification for Al, Fe, Mg, and Si, determined from calibration curves, was 0.8, 0.6, 5.3, and 4.7 μg kg^{-1} respectively. The average analytical uncertainty, measured against two certified reference materials for Al, Fe and Mg (SLRS-5 CRM, National Research Council Canada; NWTM-27.3, LGC Standards), and an inhouse standard for Si, was determined to be 5.7, 6.7, 1.1, and 7.9% respectively.

The 7500ce uses an octopole reaction system to eliminate spectral interferences (Planquette et al., 2009).

3. 3. 2. Atomic Absorption Spectroscopy (AAS)

Some elements were also analysed by atomic absorption spectroscopy (AAS) in order to both cross correlate the ICP-MS data (e.g. Mg, Fig. 3.4), and to be able to test any effects of matrix on experiments (i.e., KPH, NH_4Cl, $CaCl_2$, NaCl and Na-Citrate). AAS is a technique for determining the concentration of elements in a sample by measuring the absorption of light by atoms in a gaseous state. A solution sample is atomised by using a flame or furnace atomiser, heating the sample to > 2000 °C, before it is passed through the light path, where absorption of radiation by a certain element has a corresponding wavelength. The intensity of absorption correlates with element concentration and is calculated using a series of calibration standards.

AAS was used to determine the Al, Fe, K, and Mg concentrations in solution samples from the closed- and open-system dissolution experiments described in 3. 2. 3 and 3. 2. 4. The analyses were performed either on an Analytik Jena Contraa 700 by flame AAS, or on a Perkin Elmer 5100PC in both flame and graphite furnace AAS mode. The limit of quantification for K and Mg on the Analytik Jena Contraa 700 was 14.3 and 2.6 μg kg^{-1} respectively, and 5.1, 0.14, and, 0.02 mg kg^{-1} respectively on the Perlom Elmer 5100PC. The maximum analytical uncertainties from the AAS analysis were 5.4, 7.8, 4.9, 11.1, and 2.1% for K, Mg (Analytik Jena Contraa 700), Al, Fe, and Mg (Perkin Elmer 5100PC) respectively.

To assess the quality of the analysis, identical samples were measured by both AAS and ICP-MS, these are plotted in Fig. 3.4. A linear regression of the magnesium concentrations from AAS and ICP-MS yields a line with a gradient of 1.1 and a coefficient of determination (R^2) of 0.95, p=0.0003.

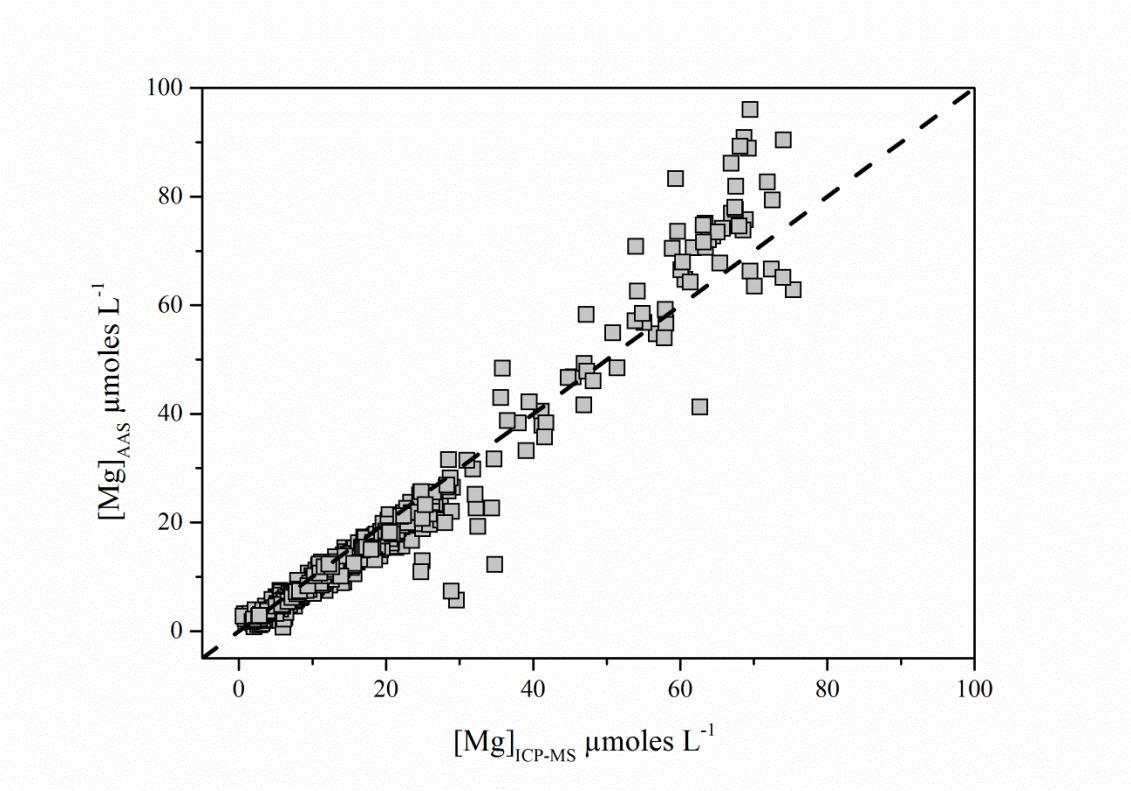

Figure 3.4

Aqueous magnesium concentrations measured by AAS plotted against the corresponding value as measured by ICP-MS in this study. The dashed line represents a 1:1 ratio. Linear regression of the plotted data yields a gradient of 1.1 with a Pearson's R^2 value of 0.95, p=0.0003.

3. 3. 3. Spectrophotometric Fe and Si analysis

Dissolved Fe and Si concentrations were also determined using spectrophotometric methods. Simply, spectrophotometry relies on the formation of a metal/metalloid coloured complex which absorbs light. The peak of absorption can be in the ultraviolet-visible light range, and the intensity of absorption is dependent on element concentration.

Aqueous Fe concentration was measured using the ferrozine method (Viollier et al., 2000) measured at 562 nm using a Uvikon XL double beam UV-visible spectrophotometer. Aqueous Si concentrations was also measured spectrophotometrically using the molybdate blue method (Tréguer and Le Corre, 1975; Coradin et al., 2004; Eaton et al., 2005) at 815 nm using a Uvikon XL double beam UV-visible spectrophotometer, and at 660 nm using a Bran & Luebbe Technicon AutoAnalyser III. The limit of quatification for Fe and Si was 2.6 and 12.1 μmoles kg^{-1} respectively.The maximum analytical uncertainty for analyses, determined by in house standards was 4.4% and 3.5 % for Fe and Si respectively.

3. 4. KINETIC CALCULATIONS AND SOLUTION MODELLING

3. 4. 1. Closed-system experiment kinetics

The measured fluid concentration of element $\boldsymbol{i}$ time t ($\boldsymbol{c}_{i,t}$) in the closed-system are used to calculate the number of moles of each element, $\boldsymbol{i}$, in the fluid phase at time t ($m_{i,t}$) normalised to the mineral surface area present in the reactor, and the stoichiometry of the dissolving biotite ($\boldsymbol{m'}_{i,t}$), as follows

$$\boldsymbol{m'}_{i,t} = \frac{\boldsymbol{m}_{i,t}}{\boldsymbol{s} \cdot M \cdot n_{\boldsymbol{i}}} = \frac{\boldsymbol{c}_{i,t} \cdot \boldsymbol{V}_t}{\boldsymbol{s} \cdot M \cdot n_{\boldsymbol{i}}}$$

Eq. 3.9

where $\boldsymbol{V}_t$ refers to the mass (kg) of reactive fluid in the reactor at time t, the symbol $\boldsymbol{s}$ represents the specific surface area of biotite powder ($m^2\ g^{-1}$, either SSA_{BET} or SSA_{geo}), M the mass of biotite powder (g), and n_i the stoichiometry of the *ith* element in the biotite formula. The number of moles released into the fluid phase at time t can also be described by the equation:

$$\boldsymbol{m'}_{i,t} = k' t^{q}$$

Eq. 3.10

where k' is a release rate constant (moles of biotite m^{-2} s^{-q}), t the time in seconds and q, a number between 0 and 1 which describes the decay of the release rate (dimensionless). Eq. 3.10 is based on the formalism described by Oelkers et al. (2001) for the interpretation of closed-system dissolution experiments, which are described below.

In the absence of a dissolution plateau, constant pH, far from equilibrium dissolution rates are consistent with the empirical formula (Lasaga et al., 1994; Oelkers, 1996)

$$-\frac{d\boldsymbol{m}_M}{dt} = \frac{d\boldsymbol{m}_i}{dt}\frac{1}{n_i} = k_+ \boldsymbol{S} \prod_i \boldsymbol{m'}_i^{\,q'_i}$$

Eq. 3.11

Where $\boldsymbol{m}_M$ is the number of moles of dissolving mineral, $\boldsymbol{m}_i$ the number of moles of the ith element released by dissolution, n_i the stoichiometric number of moles of the ith element in one mole of the dissolving mineral, k_+ represents a rate constant, $\boldsymbol{S}$ the mineral surface area, and q'_i the reaction order with respect to the ith aqueous element concentration. Eq. 3.11 can be applied to all elements released by dissolution of the Mth mineral. If the mineral dissolves independently of the aqueous concentration of the jth element then q'_j can be set to zero. In closed-system mineral dissolution experiments with solution of mass M_s, where initial dissolution of the mineral is stoichiometric and the fluid contains no dissolved ith or jth elements such that

$$\frac{\boldsymbol{m'}_i}{q'_i} = \frac{\boldsymbol{m'}_j}{q'_j}$$

Eq. 3.12

Which can be rearranged to

$$\boldsymbol{m'_i} = \frac{q'_i}{q'_j}\boldsymbol{m'_j}$$

Eq. 3.13

Substituting Eq.3.13 into Eq. 3.11, and accounting for the solution mass, leads to

$$-\frac{dm_M}{dt} = \frac{M_s}{n_j}\frac{d\boldsymbol{m'_j}}{dt} = k_+\boldsymbol{S}\prod_i\left(\frac{q'_i}{q'_j}\right)^{q'_i}\boldsymbol{m'_j}^{\sum_i q'_i}$$

Eq. 3.14

Dividing the equation by $\boldsymbol{m'_j}^{\sum_i q'_i}$ and rearranging leads to

$$\boldsymbol{m'_j}^{-\sum_i q'_i}d\boldsymbol{m'_j} = \left(\frac{\left(n_j k_+\boldsymbol{S}\prod_i\left(\frac{q'_i}{q'_j}\right)^{q'_i}\right)}{M_s}\right)dt$$

Eq. 3.15

Integration of Eq. 3.15 for all $\sum_i n_i \leq 0$ gives

$$\frac{\boldsymbol{m'_j}^{(1-\sum_i q'_i)}}{(1-\sum_i q'_i)} = \left(\frac{\left(n_j k_+\boldsymbol{S}\prod_i\left(\frac{q'_i}{q'_j}\right)^{q'_i}\right)}{M_s}\right)t$$

Eq. 3.16

Multiplying by $(1-\sum_i q'_i)$ and taking then taking the $(1-\sum_i q'_i)$th root, leading to

$$\boldsymbol{m'_j} = \left(\frac{(1-\sum_i q'_i)\left(n_j k_+\boldsymbol{S}\prod_i\left(\frac{q'_i}{q'_j}\right)^{q'_i}\right)}{M_s}\right)^{\left(\frac{1}{(1-\sum_i q'_i)}\right)} t^{\left(\frac{1}{(1-\sum_i q'_i)}\right)}$$

Eq. 3.17

Subsequently, by letting

$$k' = \left(\frac{(1 - \sum_i q'_i)\left(\mathrm{n}_j k_+ \boldsymbol{S} \prod_i \left(\frac{q'_i}{q'_j} \right)^{q'_i} \right)}{M_\mathrm{s}} \right)^{\left(\frac{1}{(1-\sum_i q'_i)} \right)}$$

Eq. 3.18

and

$$q = \left(\frac{1}{(1 - \sum_i q'_i)} \right)$$

Eq. 3.19

Eq. 3.17 can be written as in Eq. 3.10. These equations imply that the rate of biotite dissolution is controlled by the concentration of released elements.

$$\log_{10}[\mathrm{M}_i] = \log_{10} k' + q \log_{10} t$$

Eq. 3.20

The logarithmic equivalent of Eq. 3.10 plots a straight line with a gradient of q and intercept of k'. Values of q allow the assessment of the order of reaction with respect to the *i*th element. A gradient of 1 indicates a zeroth order reaction, values less than 1 indicate a negative reaction order with respect to the *i*th element. The order of reaction with respect to a single element is difficult to assess as there are 5 major elements released during dissolution which could have an effect on the dissolution, K, Mg, Fe, Al and Si.

Being able to describe the concentration of released elements at a given point in time allows the calculation of the release rate of the *i*th element at any time *t* ($r_{i,t}$) by taking the derivative of Eq. 3.10, such that

$$r_{i,t} = \frac{\partial \boldsymbol{m'_i}}{\partial t} = q k' t^{(q-1)}$$

Eq. 3.21

where $r_{i,t}$ is the release rate of the *i*th element at time *t*.

The closed-system element release rates are discussed further in chapter 5, Along with the open-system kinetic calculations.

3. 4. 2. Open-system experiment kinetics

The calculation of element release kinetics is more straightforward in open-system experiments, where the rate of release of the *i*th element (r_i) at a given point in time is calculated by the equation

$$r_i = \frac{\mathrm{f} \cdot \boldsymbol{c_i}}{\boldsymbol{s} \cdot M \cdot n_i}$$

Eq. 3.22

where f represents the flow rate (kg s^{-1}), $\boldsymbol{c_i}$ the aqueous concentration of the *ith* element in the outlet fluid (mol kg^{-1}), $\boldsymbol{s}$ stands for the initial specific surface area (m^2 g^{-1}, SSA_{BET} or SSA_{geo}) of the mineral powder of mass M (g), and n_i the stoichiometric coefficient of the *ith* element in the biotite formula.

The use of the open-system element release rates are discussed further in chapter 5, along with the assessment of steady-state element release.

3. 4. 3. PHREEQC 3 modelling

To complement the analytical data and assess solution based processes in chapters 4 and 5 the measured chemistry of fluid samples from the batch potentiometric titrations and closed- and open-system experiments were modelled using PHREEQC 3 (Parkhurst and Appelo, 2013). The first phase of modelling was conducted to determine the speciation of metals in the solution samples of the batch potentiometric titrations and to assess the potential of secondary phase formation in the batch potentiometric titrations and closed-system dissolution experiments. The second phase of modelling was conducted to understand the likely metal-organic ligand interactions in the experiments described in sections 3. 2. 3 and 3. 2. 4, to better understand the role of organic ligands in controlling element release rates.

3. 4. 3. 1. Metal speciation and secondary phase potential

One of the important processes controlling protons in solution is hydrolysis. This is outlined in chapter 4 but the calculations of proton consumption rely on speciation of

elements in solution. The speciation of elements in each batch experiments was calculated based on the measured element concentrations and pH values using the wateq4f.dat database in PHREEQC.

Solutions were also modelled for the potential formation of secondary phases during the course of the batch potentiometric titrations and closed-system experiments. These calculations were performed similarly by inputting the measured concentrations and pH values and calculating the saturation index (Ω) of all possible phases, focussing on quartz (SiO_2), amorphous silica (α-SiO_2), sepiolite ($Mg_4Si_6O_{15}.(OH)_2.6H_2O$), kaolinite ($Al_2Si_2O_5(OH)_4$), gibbsite ($Al(OH)_3$), and goethite (FeOOH), as these are the phases most likely to form in the experimental conditions. The results of these calculations are discussed in chapters 4 and 5.

3. 4. 3. 2. Metal-organic ligand complexes

The calculation of metal-organic ligand complexes was completed in two stages. First, the organic ligand speciation was calculated as a function of pH between 1 and 10. Secondly the speciation of ligands and metals were calculated together using measured concentrations from experimental samples and acid dissociation constants, obtained from Martell and Smith (2007), National Institute of Standards and Technology (NIST) reference database 46, version 8 (Martell et al., 2004) and Wolff-Boenisch and Triana (2006). These calculations also revealed the saturation indices (Ω) the species mentioned in section 3.4.3.1.

3. 5. PLANT-FUNGI CONTINUUM AXENIC MICROCOSM

In this section I will describe the preparation and setup process of the plant-fungi continuum axenic experimental microcosms involving *Pinus sylvestris* (Scots pine) and *Paxillus involutus*. These experimental microcosms are the central part of the work described in chapter 6 that aims at evaluating the growth rates of fungi over biotite surfaces in different conditions, and to provide samples for characterisation of the biochemical changes during the growth of a fungi over biotite surfaces.

Experiments were set up at different levels of pCO_2 to evaluate the effect of elevated CO_2 on fungal growth, yet all other aspects of these experiments were identical and are described below.

Prior to the start of the growth observations there are 4 stages of preparation; seed germination, fungal cultivation, mycorrhizal synthesis, and the transfer to experimental microcosm setup. Collectively these stages take approximately 6 months to carry out. Each stage of the setup has the potential to irreversibly damage the seedlings and fungal colonies, so every care was taken to handle the systems delicately and aseptically, to avoid contamination. In what follows, each stage of microcosm setup will be described.

3. 5. 1. Seed germination

Seeds of *Pinus sylvestris* from Roseisle, Grampian (SP.08 RP2051 A70, purchased from the Forestry Commission, UK) were washed by vortex in 30 % H_2O_2 for 10 minutes, then washed in sterile distilled water, and subsequently dried. The washing process serves two purposes: a) to sterilize the coat of the seeds to prevent contamination within the growth agar and b) to scarify the seed coat which encourages germination.

Seeds were then transferred in sterile conditions to plates containing 1.2% plant agar (Fig. 3.5). Seed plates were sealed with parafilm and placed in two climate controlled growth chambers for germination over 4 to 6 weeks at 15 °C and 60% humidity (day), and 10 °C and 75% humidity (night), with an 18 hour photo period (550 μmol m^{-2} s^{-1} irradiance) and either 350 or 1500 ppm CO_2. Germination plates were checked regularly

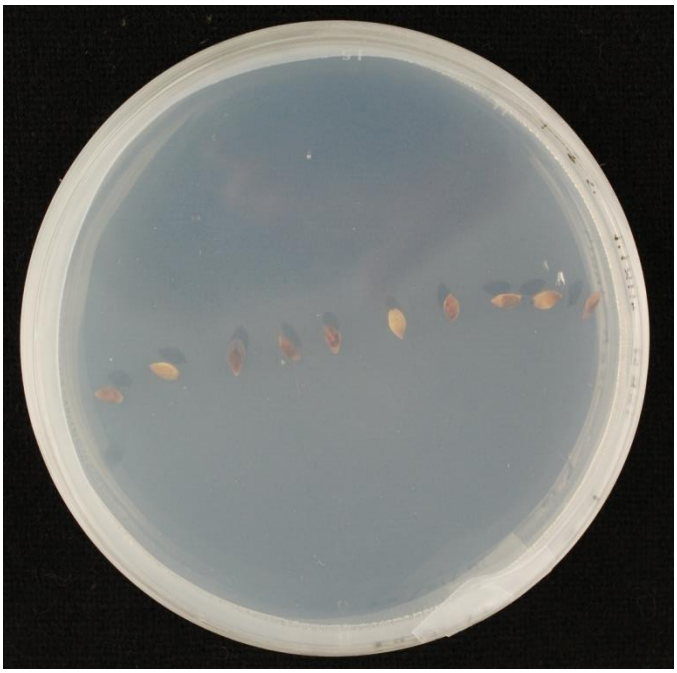

Figure 3.5

Pinus sylvestris seeds on 1.5% plant agar plate ready for germination

for contamination and any found was removed by cutting the contaminated agar out of the plate. This treated contamination problems and did not adversly affect seed germination or growth.

3. 5. 2. Fungal cultivation

To test growth viability, established *P. involutus* colonies, grown on modified Melin Norkrans (MMN) nutrient agar (Table 3.1), were sampled using a sterile cork borer and with sample discs were transferred to a Petri dish containing a 1/10 strength MMN nutrient agar covered by an acid washed and autoclaved cellophane sheet. Petri dishes were sealed with parafilm and stored at 20 °C for one week to allow the fungi to 'fluff' (Fig. 3.6), demonstrating new growth of hyphae. Individual plugs were subsequently transferred to square Petri dishes and allowed to grow at 20 °C for 3 weeks in preparation for synthesis with seedlings.

Table 3.1

Compositions of agar solutions used for seed germination and fungus cultivation

Chemical	1.2% Plant agar	MMN
	mmol L^{-1}	
$CaNO_3$	2	-
$MgSO_4$	1	6.0×10^{-2}
K_2HPO_4	1.2	$3.7\ 10^{-1}$
$(NH_4)_2SO_4$	8.0×10^{-2}	-
FeEDTA	2	-
$MnSO_4$	9.0×10^{-3}	-
H_3BO_4	5.0×10^{-2}	-
$(NH_4)_6Mo_7O_{24}$	1.5×10^{-4}	-
$ZnSO_4$	1.5×10^{-3}	-
$CuSO_4$	1.5×10^{-3}	-
$(NH_4)_2HPO_4$	-	1.9×10^{-1}
$CaCl_2$	-	4.3×10^{-2}
$FeCl_3$	-	2.2×10^{-2}
	g L^{-1}	
Malt extract	-	10
Glucose	-	1
Agar	12	15

3. 5. 3. Mycorrhizal synthesis

After approximately 4 weeks of growth the *Pinus sylvestris* seedlings were transferred, aseptically, to the 1/10 strength MMN plates, previously colonised by the fungus. The seedlings were placed so that their roots were in contact with both the cellophane sheet and the growth front of the fungal colony, to enable the plant to both settle on the new plate and form the mycorrhizal symbiosis.

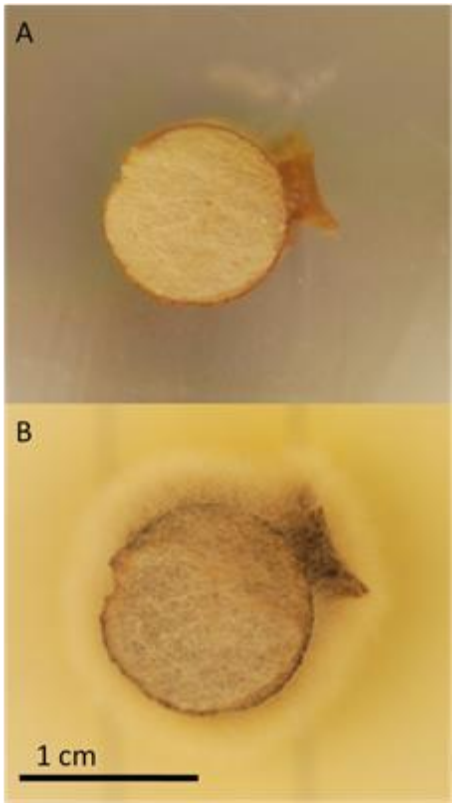

Figure 3.6

Paxillus involutus disk (A) after cutting, t = 0 and (B) showing new 'fluffy' hyphal growth, t = 1 week. The 'fluff' are the light fibres extending from the fungal plug.

At this stage, the shoot of the plant protrudes the square Petri dish through a hole sealed with sterilized lanolin and two layers of parafilm (Fig. 3.7). The plates were wrapped in aluminium foil to prevent light from penetration. This is the stage at which mycorrhizal symbiosis occurs and it is characterised by the formation of short 'T' shaped roots entangled in hyphal strands. The synthesis takes ~ 8 to 10 weeks to form a strong mycorrhizal relationship as shown in Fig. 3.7. This symbiotic growth occurs under the same conditions as seed germination.

3. 5. 4. Experimental microcosm

After the 8 to 10 weeks of mycorrhizal synthesis, plant-fungi symbionts are ready for the transfer to the experimental microcosm (Fig. 3.8). The experimental microcosms were prepared by pouring 80 mL of 1.2 %plant agar with the chemical concentration listed in Table 3.1 into a sterile square Petri dish which was then covered with an acid washed and autoclaved sheet of cellophane. These Petri dishes were incubated for 1 week at 25 °C to check for any microbial contamination. For the sterile plates in which no contamination was observed, an additional 20 mL of plant agar medium was poured on

Figure 3.7

Pinus sylvestris and Paxillus involutus after 8 weeks of mycorrhizal synthesis showing the formation of characteristic 'T' shaped short roots.

top of the cellophane sheet. Before cooling and solidifying, 6 empty plastic wells were added to the plant agar medium at even spacing and approximately 50 g of acid washed, rinsed and autoclaved perlite of 2.0 to 2.4 mm grain size was scattered over the agar in a single layer. Perlite is a relatively inert amorphous volcanic glass from which the organisms do not obtain nutrients.

Seedlings well colonised with fungus were then transferred aseptically to the experimental microcosm with roots spread across the perlite layer and shoots protruding outside the dish through a hole sealed with sterile lanolin. Experimental microcosms were sealed with parafilm, wrapped in aluminium foil and allowed to grow for 2 weeks to ensure that the plant-fungi settled in to the system. The empty plastic wells were replaced with wells containing autoclaved ~1cm^2 flakes of freshly cleaved biotite. The biotite was adhered in the wells with a silicon based sealant so that the flake was level with the top of the well. The remaining area in each well was filled with 1.2% plant agar medium and covered in a single layer of sterile perlite grains.

The final experimental microcosms (Fig. 3.8) were then grown in growth chambers for up to 6 months, with the initial stages of fungal colonisation of the biotite chips being used for the evaluation of fungal growth rates on biotite through time resolved observations by light microscope (section 3.6) and for monitoring changes in biochemical composition of the fungal hyphae by synchrotron based infrared microspectroscopy (section 3.7).

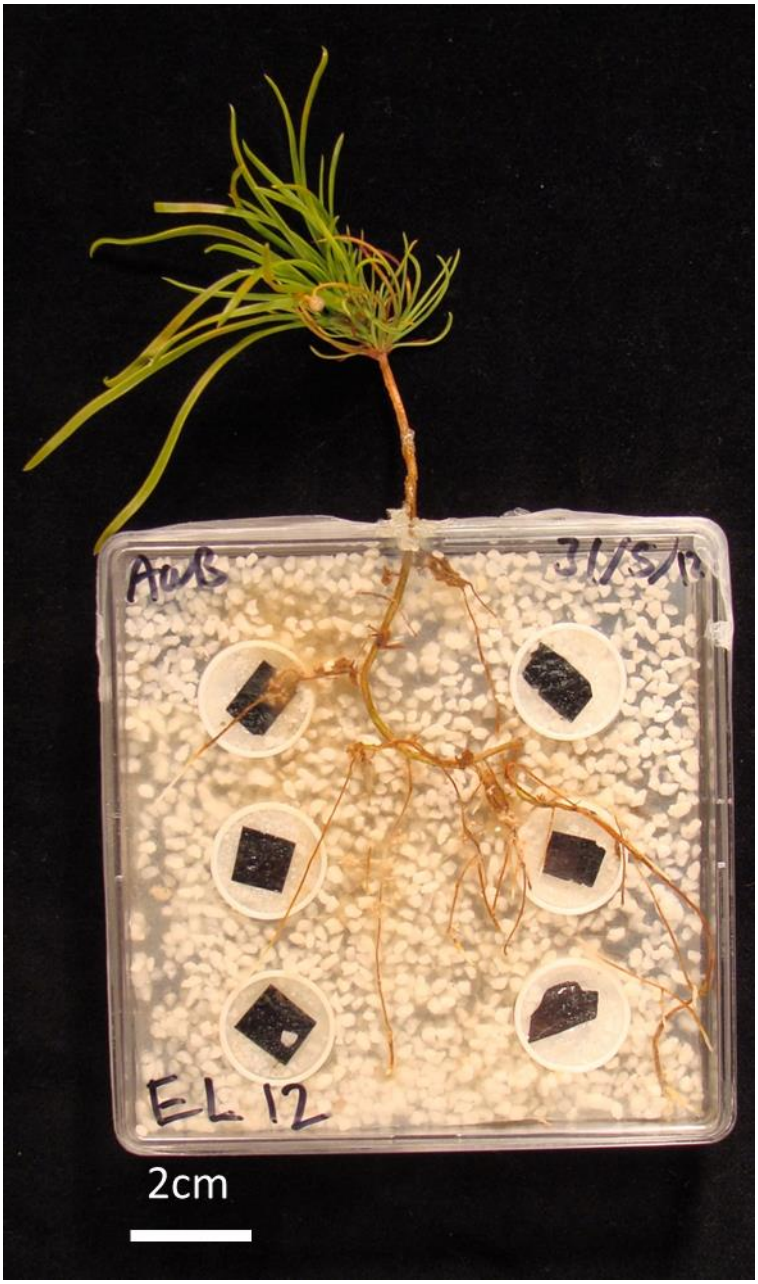

Figure 3.8

Experimental microcosm after 3 months of growth. The orange haze visible is the mycelial network extending between the white perlite grains and colonising the black biotite flakes.

3. 6. FUNGAL GROWTH OBSERVATIONS

From the first research output of the Weathering Science Consortium describing the fungal weathering processes at the nanometer scale (Bonneville et al, 2011) it became clear that an important, and as yet unmeasured, term for quantifying the fungal bio-weathering rates was a precise understanding of the rate and geometric characteristics of fungal hyphae growth over a mineral nutrient source, such as biotite. To obtain data on the geometric characteristics for ease of modelling we can assume that an individual fungal hypha is a line which branches at nodes along the hyphal length forming new hyphae. We can therefore quantify the number of nodes and hyphal tips per total hyphal length, for each of the pCO_2 conditions. Practically obtaining this dataset involved capturing time resolved images of the biotite surface colonised by mycorrhiza and, processing of the image series to extract of geometric parameters. These methods are described below.

3. 6. 1. Image acquisition

To quantify growth rates and characteristics of fungal growth, images of the fungi in contact with the mineral were collected over time using light microscopy. The microscope used was a Nikon Eclipse ME600 microscope fitted with a Nikon CF Plan 20X extra-long working distance (ELWD) objective and a Newport motion controlled stage. The 20X ELWD objective allows the imaging of samples through the plastic lid of the Petri dish at a working distance of 11.00 mm which is necessary as a standard objective requires a working distance of approximately 3mm. This ELWD objective permitted the high-resolution imaging of colonized biotite surfaces without opening/disturbing the system, therefore, minimising the risk of contamination of the microcosm.

The 20X objective gave a field of view of 500 X 500 μm and was selected due to the need to compromise between a higher resolution but shallow depth of field (50X), and greater depth of field but lower magnification (10X). Although the surface of cleaved biotite flakes is predominantly flat, the growth of a hypha is not necessarily level, hypha often grow ‘aerially’ to avoid obstacles such as water droplets. A higher magnification

objective has a shallower focal depth, which means that not all the hypha can be in focus in a single field of view. The Newport motion controlled stage consisted of a Newport Universal Motion Controller ESP300 and two UTM50CC motors working in the *x* and *y* dimensions. This setup allowed the accurate and precise control of movement to the micrometre scale, offering the possibility to move the stage by known distances and return to previously visited locations on a sample. To secure microcosms in the microscope setup and allow reliable relocations of samples the stage was fitted with a custom made square Petri dish holder.

Experimental microcosms were imaged using the above microscope setup on a daily to weekly basis to assess the start of fungal colonisation of the biotite flakes. Once the fungi had reached a biotite flake the area of initial colonisation was mapped by acquiring between 20 to 200 images, moving 400 μm in either the *x* or *y* direction between each image. The coordinate location of each image was noted. The images were aquired using a BestScope BUC2-500C down eye-piece camera. The microcosms were imaged over a time period of 5 to 10 days and several fungal hyphae were tracked in experimental systems at both low and high CO_2 conditions

The main limitation of this approach was that through the course of observation, by light microscope, condensation formed on the lid of the Petri dish gradually obscuring light. After approximately 30 minutes the amount of condensation was too high to accurately observe the hyphae on the surface of the mineral. The formation of condensation on the mineral surface also causes the hyphae to grow differently. Hyphae appear to grow aerially upon interaction with surface based condensation droplets.

3. 6. 2. Image processing and analysis

The large number of images for each time step were stitched together manually using a graphics programme. Initially, images were positioned by the coordinates of movement noted from the motion controlled stage. Once in the correct coordinate location, images were adjusted so that features in neighbouring images were aligned. The

movement in each direction left space for overlap between images, aiding the stitching process. Most graphics software packages have a feature which auto-stitches or merges images based on common and individual features of each image. This method was tried for these images but the number of similarities was so great the software could not stitch the pictures together.

Once a time step image composite was fully stitched, individual fungal hyphae were measured for width and traced using vectors which were subsequently exported to ImageJ (Rasband, 1997; Abramoff et al., 2004). Using the "Measure" command hyphal lengths in each time step were quantified, along with a count of nodes. Differences in hyphal lengths from each composite image set were used to calculate growth rates by normalising to the experimental growth time between each observation. This data is presented and discussed in chapter 6.

3. 7. SYNCHROTRON BASED μ-FTIR

Various publications from other members of the NERC Weathering Science Consortium also highlighted the role and importance of fungal hyphae in physically forcing and chemically altering the mineral (Bonneville et al., 2009; Bonneville et al., 2011; Gazzè et al., 2012). However, no information on biochemical changes in the hypha themselves was available, Therefore, we used synchrotron based fourier transform infrared microscpectroscopy (μ-FTIR) to assess changes in the biochemical composition of fungal hyphae with the view to link this to hyphal functionality in mineral weathering. These measurements were carried out at station B22 at the Diamond Light Source, UK on samples obtained from the plant-fungi microcosm experiments described in section 3.5. The basic theory and methods used are described below and results are discussed further in chapter 6.

3. 7. 1. Synchrotron radiation

There are many advantages in performing FTIR measurements using synchrotron radiation over laboratory based globar radiation sources. Synchrotron light is very intense

(brightness is ~ 1000 times more than globar source), the signal to noise ratio (S/N) is much lower and measurements can be spatially resolved. All these characteristics, allow measurement to be done at a much higher spatial and S/N resolution than conventional infrared measurements using a conventional globar source. Full details of station and instrument characteristics as well as data acquisition and processing and interpretation are given in chapter 6.

Chapter 4. Biotite surface chemistry as a function of aqueous fluid composition

This chapter is a reproduction of a peer-reviewed publication in *Geochimica et Cosmochimica Acta*: Bray A. W., Benning L. G., Bonneville S., Oelkers E. H. (2014) *Geochim. Cosmochim. Acta* **128**, 58-70. It addresses the first research objective from the introduction, to determine the chemical composition of the near surface of biotite after interaction with fluids for a short period of time. The surface chemistry is highly pH dependent and cations are extremely mobile at all pH. This is important for our understanding of mineral surface interactions with fluids and organisms in natural systems.

Abstract

The chemical composition and charge of the biotite near-surface, in contact with NaCl bearing aqueous solutions at 25 °C from pH 1 to 12, has been derived via zeta potential measurements and potentiometric titrations performed for 20 and 60 minutes in batch reactors. Zeta potential measurements yielded an isoelectric point of pH 3.0 (± 0.2) and batch potentiometric titrations yielded a pH of immersion of 9.66 (S.D. 0.24). From batch potentiometric titrations both the proton consumption and the metal release from the biotite surface was determined as a function of pH. Potassium removal from the near-surface of biotite is only slightly dependent on pH with a minimum of ~ 6 atoms nm^{-2} removed at the immersion pH, corresponding to an of average depletion depth of ~ 1.5 nm. In contrast, the release of Mg, Al and Fe is strongly pH-dependent as those metals are preferentially removed from the biotite surface at pH less than 9 (Mg) and 4 (Al, Fe). The average depletion depth of Mg, Al, and Fe increases with decreasing pH, reaching on average ~ 2 nm at pH ~1. The removal of K, Mg, Al, and Fe is not charge conservative, resulting in a relative negative charge in the biotite near-surface. Taken together, these

results indicate that the composition of the biotite surface varies dramatically as a function of pH. At basic conditions, the biotite near-surface is K depleted and likely hydrogen enriched. At near-neutral conditions, the biotite near-surface is comprised of only the Si and Al tetrahedral, and the $Fe^{(II)}$ octahedral framework, following the removal of both alkali metals and Mg. Finally, at acidic conditions, the biotite near-surface is comprised exclusively of a remnant Si, O and H framework. The results of these experiments give an indication of the composition and charge of the biotite surface in the natural environment, following contact with water, for example in the vadose zone, and can help the understanding of weathering reactions in these systems.

4. 1. INTRODUCTION

Mineral surface composition and charge are often linked to mineral reactivity and adsorption properties (e.g. Pokrovsky et al., 1999; Sverjensky, 2004). Among the most significant minerals in the subsurface, in terms of controlling the chemical composition and evolution of surface waters, are the phyllosilicates (including clays). This is due to their large surface areas and high ion-exchange capacity (Sposito, 1984; Davis and Kent, 1990; Drever, 1997; Bowser and Jones, 2002). Several recent studies reported that due to metal exchange reactions, the composition of the near-surface of multi-oxide minerals depends strongly on the composition of its surrounding aqueous phase (e.g. Pokrovsky and Schott, 2000; Chaïrat et al., 2007; Oelkers et al., 2009). In an attempt to extend these concepts to phyllosilicates, we have performed a series of batch potentiometric titration experiments and electrokinetic measurements on biotite surfaces as a function of aqueous solution pH from 1 to 12. The purpose of this paper is to report the results of these experiments aimed towards the improved understanding of how the surface compositions of phyllosilicate minerals are influenced by the aqueous phase composition.

Mineral surface chemistry has often been linked to dissolution rates (Morel and Hering, 1993). Early studies attempted to correlate mineral surface charge to the concentration of surface-sites, determined via potentiometric titrations as a function of pH (e.g. Furrer and Stumm, 1986; Brady and Walther, 1990; Pokrovsky and Schott, 2004). This approach has subsequently been questioned by observations that in addition to proton absorption and desorption a large number of reactions influence proton consumption during potentiometric titrations (e.g. Oelkers et al., 2009). Furthermore, dissolution rates of a wide range of minerals can depend on the activity of aqueous metals present in solution (e.g. Oelkers et al., 1994; Gautier et al., 1994; Devidal et al., 1997; Gislason and Oelkers, 2003; Wolff-Boenisch et al., 2004; Carroll and Knauss, 2005; Saldi et al., 2007). A further motivation of this study is therefore to characterise the reactions controlling the surface chemistry of a reference phyllosilicate, biotite, to improve our understanding of the overall dissolution mechanism of this widespread family of minerals.

A further motivation for a quantitative understanding of the surface properties and dissolution behaviour of phyllosilicates is due to their significance as a nutrient source in the terrestrial environment. A number of studies have reported on the crucial role of micro-organisms in weathering primary minerals and acquiring key nutrients (e.g. Leyval et al., 1991; Drever and Stillings, 1997; Wallander and Wickman, 1999; Adeyemi and Gadd, 2005; Gadd, 2007; Buss et al., 2007; Lian et al., 2008, Smits et al. 2012). Several studies focussed on biotite weathering and metal acquisition by bacteria (e.g. Balland et al., 2010) and fungi (e.g. Balogh-Brunstad et al., 2008b; Bonneville et al., 2009, 2011). Remarkably, for fungi, the weathering process is a combination of mechanical forcing of the biotite near-surface and several chemical alteration pathways. These studies also demonstrated that the near-surface properties of biotite are crucial in controlling the initiation of weathering processes. Yet, how the chemistry of the biotite

near-surface influences both nutrient availability and the mechanism of micro-organism nutrient acquisition is still unknown.

In this study, we have assessed the degree to which the biotite near-surface chemistry is influenced by the composition of its surrounding aqueous phase. This has been done through a series of batch potentiometric experiments at 25 °C and between pH 1 and 12, which were also complimented through electrokinetic measurements. Titration results were interpreted to (i) evaluate the main contributing reaction types occurring at the biotite surface and (ii) determine how the composition of the biotite surface varies as a function of pH.

4. 2. EXPERIMENTAL METHODS

4. 2. 1. Mineral sample

The biotite used in this study originated from the Grasåsen feldspar quarry, Moen, Arendal, Aust-Agder, Norway (sourced from Agder Naturmuseum, Kristiansand). A large piece (~ 600g) was broken into chunks and all visible inclusions were removed. For the chemical characterization, a polished block of the biotite was imaged using a field emission gun scanning electron microscope (FEG-SEM, FEI Quanta 650 equipped with Oxford an X-Max silicon drift detector, SDD and operated at 20 kV). The biotite, along with inclusions and areas of alteration, was imaged and characterised using backscattered electron emission (BSE) and energy-dispersive X-ray spectroscopy (EDX). The bulk chemical composition of the biotite was characterised by electron microprobe analysis (EMPA, Jeol JXA-8230 running with a tungsten source at 15kV and 15nA) using the average of 15 point measurements ($\sum$ oxide weight > 99%) and $O_{10}(OH)_2$ formula units. The electron microprobe analysis of the Grasåsen biotite yielded the following chemical composition $(K_{0.913}\ Na_{0.011}\ Ca_{0.0002})(Mg_{1.436}\ Mn_{0.004}\ Fe^{(II)}_{1.098}\ Cr^{(II)}_{0.0004})(Al_{1.312}\ Ti^{(IV)}_{0.184}\ Si^{(IV)}_{2.832})(OH)_2(O)_{10}$. The formula is written assigning the cations into their likely

structural setting, interlayer sites (K, Na, and Ca), tri-octahedral sites within the octahedral layer (Mg, Mn, Fe, and Cr), and di-octahedral and tetrahedral sites within the tetrahedral layer (Al, Ti, and Si).

The remaining biotite was crushed using a ball mill, jaw crusher, and agate disk mill, removing visible inclusions throughout. The < 53 μm size fraction was separated and further crushed for use in the batch potentiometric and electrokinetic measurements. Crushed biotite grains were imaged using FEG-SEM and grains were observed to be between sub-micron and 10 μm in size (Fig A-1). The specific surface area (*s*) of this crushed biotite fraction was measured via an 11 point krypton adsorption isotherm that was run from 0.046 to 0.30 p/p_o (equilibrium pressure/saturation pressure) at 77 K, on a Quantachrome AUTOSORB-1. Samples were degassed with Kr at 120 °C for 23 hours before analysis and the surface area was calculated using the BET method (Brunauer et al., 1938) based on an assumed cross section of absorbed Kr of 0.205 nm^2. The specific surface area of the Grasåsen biotite was calculated to be 13.43 m^2g^{-1}. The average metal site density at the biotite surface was estimated to be 10 nm^{-2} using VESTA (Momma and Izumi, 2011) for visualising the biotite structure as presented by Brigatti et al. (2000). The crushed biotite was also analysed by X-ray fluorescence (XRF, Innov-x X-5000) at 10 kV (Table A-4) and X-ray diffraction (XRD, Bruker D8) with a scan range from 5 to 75° 2θ and a step size of 0.009° 2θ, to give an indication of any impurities within the crushed fraction. Reitveld refinement of XRD patterns by Topas software version 4.2 (copyright 1999–2009 Bruker AXS) indicated the presence of 3.7 wt. % (± 0.5%) calcite, supported by 1.36 wt. % calcium (≈ 3.4% calcite) as measured by XRF.

4. 2. 2. Batch potentiometric titrations

A total of 65 time limited, biotite-bearing batch experiments were performed at 25 °C which, when taken together, represent a potentiometric titration series, as previously described by Pokrovsky et al. (1999) and Oelkers et al. (2009). In brief, 20g/L of biotite was equilibrated while stirred in a polypropylene reactor with a NaCl electrolyte of known ionic strength (*I*) for at least 12 hours under a N_2 atmosphere (5.0 grade). Batch reactions were performed by mixing ~7 ml aliquots of this pre-equilibrated biotite suspension with a known quantity of analytical grade HCl or NaOH in 15ml polypropylene vials. Experiments were conducted under a N_2 atmosphere, for either 20 or 60 minutes and were shaken constantly at 140 rpm, with additional manual shaking every 10 minutes. At the end of each titration experiment, the pH in each vial was measured using a Metrohm 713 pH Meter, calibrated with certified reference buffer solutions of pH 4.005, 6.866, and 9.183 (CertiPUR, Merck) at 25 °C.

After pH measurement, the fluid from each batch experiment was filtered through 0.2 μm cellulose acetate Sartorius Minisart filters (and stored at 4°C analysis. The concentrations of Na, Mg, Al, K, Ca, Ti, Cr, Mn, and Fe in the filtered reactor fluids were determined by inductively coupled plasma mass spectrometry (ICP-MS, Thermo Agilent 1700C; maximum analytical uncertainty ± 5%) while aqueous silicon, Si, was determined using the colorimetric molybdate blue method (Bran & Luebbe AutoAnalyzer 3, maximum analytical uncertainty ± 3.5%).

A control titration series was obtained through otherwise identical experiments using biotite-free fluids, i.e., from the pre-equilibrated biotite suspension filtered through a 0.2 μm cellulose acetate Nalgene filter unit. The control titration series was performed to determine a baseline for data interpretation.

Full details of all biotite-bearing and biotite-free batch titration experiments can be found in Tables A-2 and A-3, respectively, in Appendix A. Details include mineral

suspension concentration, fluid ionic strength, experiment time, suspension volume, and titrant concentration at the start of the experiment (t=0); and, pH and fluid composition at the end of each titration.

4. 2. 3. Electrokinetic measurements

The electrophoretic mobility of the biotite powder was measured at 25°C using a Zetaphoremetre IV, model Z3000 microelectrophoremeter with a dielectric constant of 80 ±1 V. For each measurement, biotite powder was added to individually prepared aqueous NaCl or HCl solutions (I = 10^{-1} to 10^{-3} M) with pH from 1 to 12 and measured within 5 minutes by electrophoresis. As in the batch titrations, the pH range for electrophoretic measurements was attained through the addition of analytical grade HCl or NaOH. The pH of each fluid sample was measured externally during electrophoresis. Measured electrophoretic mobilities were converted to ζ-potentials using the Smoluchowski equation (Hunter, 1989) and are presented in Table A-4 in Appendix A, along with the details of solutions used for electrophoretic measurement.

4. 3. THEORETICAL BACKGROUND

This study builds from our current understanding of the mineral-fluid interface (c.f. Parks, 1965; Parks 1967; Davis and Kent, 1990; Parks, 1990; Sposito 1998; Pokrovsky and Schott, 2000; Oelkers et al., 2009; Brown and Calas, 2012). A large number of terms are necessary to describe these interfaces, and their definitions can be ambiguous, thus, we briefly review some of these here.

The zero point of charge (pH_{ZPC}) is the pH value where, regardless of source, the net charge at the surface of a material is zero.

There are three primary methods for determining the pH_{ZPC} of minerals. (1) The isoelectric point (pH_{IEP}), as determined by electrokinetic measurements, indicates the pH

at which there is no net charge at the hydrodynamic shear-plane of a particle in solution; and therefore, the point at which there is no movement of particles in an electric field (note that ions can adsorb to the mineral surface and hence contribute to the charge at the hydrodynamic shear-plane and, therefore, to pH_{IEP}). (2) Acid-base potentiometric titrations of a mineral yield the point of zero net proton charge (pH_{ZNPC}), the point at which the concentrations of H^+ and OH^- ions consumed by a surface are equal, therefore giving the surface a net neutral charge. This is synonymous with the pH of an aqueous solution in equilibrium with a mineral, when no titrant has been added, also referred to in this study as the immersion pH (pH_{imm}). (3) The common intersection point of acid-base titration curves at two or more ionic strengths yields the point of zero salt effect (pH_{PSZE}).

When there is no internal net charge on the mineral and in the absence of ions for adsorption, other than H^+ and OH^-, $pH_{IEP} = pH_{ZNPC} = pH_{PZSE} = pH_{ZPC}$ (Sposito, 2004). However, in a large number of cases $pH_{IEP} \neq pH_{PZSE}$ (c.f. Sverjensky, 2004) and in such cases the pH_{IEP} determined at low ionic strengths (e.g. 0.001-0.01 M) may be more representative of pH_{ZPC} (Sverjensky, 1994). Furthermore, to accurately model the mineral surface, both the surface composition and the electrochemical state must be considered. Both these parameters can be determined via potentiometric titrations by quantifying proton consumption at both the mineral surface and in all other proton-consuming reactions. These in turn can all be determined from accurate pH measurements in combination with aqueous analysis of the dissolved species present during the titration.

In this study, the total amount of protons consumed, normalized to mineral surface area, ($[H^+_{tot}]$, atoms nm^{-2}) during timed batch titration experiment was derived from the difference between the calculated proton concentration in each reactor at the start of each titration ($[H^+]_{t=0}$, mole kg^{-1}) (from the volume and concentration of acid/base

added) and the concentration of protons determined from the measured pH of the aqueous suspension, after its interaction with biotite powder ($[H^+]_{t=t}$, mole kg^{-1}). The value of $[H^+]_{t=0}$ was calculated using:

$$[H^+]_{t=0} = \frac{\left((\boldsymbol{m}_a \boldsymbol{M}_a) + (\boldsymbol{m}_e \boldsymbol{M}_e)\right)}{(\boldsymbol{M}_a + \boldsymbol{M}_e)}$$

Eq. 4.1

where m_a and m_e (mol kg^{-1}) correspond to the concentration of protons in the added titrant and the mineral-electrolyte suspension, respectively, while M_a and M_e (kg) designate the masses of these fluids. Proton concentration at the end of each experiment $[H^+]_{t=t}$ was calculated from the measured pH, such that

$$[H^+]_{t=t} = \left(\frac{10^{-pH}}{\gamma_{H^+}}\right) - \left(\frac{10^{-(-\log(K_{H_2O})-pH)}}{\gamma_{OH^-}}\right)$$

Eq. 4.2

where γ_i (kg mol^{-1}) designates the activity coefficient of the ith aqueous species, calculated using the Davies equation (Davies, 1962), and $\boldsymbol{K}_{H_2O}$ stands for the water ionisation constant (10^{-14}; IUPAC, 2006). Combining Eqs. (4.1) and (4.2) leads to $[H^+_{tot}]$ which can be represented as:

$$[H^+_{tot}] = ([H^+]_{t=0} - [H^+]_{t=t})\left(\frac{\boldsymbol{N}}{\boldsymbol{Ms10^{18}}}\right)$$

Eq. 4.3

where N designates Avogadro's number (6.02×10^{23}), M (kg) the mass of mineral powder, and s ($m^2\ kg^{-1}$) the biotite powder specific surface area (adapted from Oelkers et al., 2009). The quantity of protons consumed due to the presence of biotite ($[H^+_s]$, atoms nm^{-2}) was calculated by subtracting from $[H^+_{tot}]$ the protons consumed in an equivalent biotite-free titration at each corresponding pH ($[H^+_0]$, atoms nm^{-2})

$$[H^+_s] = [H^+_{tot}] - [H^+_0]$$

Eq. 4.4

where $[H^{+}_{0}]$, for a given pH, was interpolated from a regression of the biotite-free titration curve (after an immersion period of 12 h, see section 4.2.2).

During each batch titration, protons were consumed or produced by reactions occurring either in the aqueous solution ($[H^{+}_{sol}]$) or through incorporation into/onto mineral surfaces ($[H^{+}_{surf}]$), such that:

$$[H^{+}_{s}] = [H^{+}_{sol}] + [H^{+}_{surf}]$$

Eq. 4.5

During the titration, three proton related, aqueous solution-based reactions occur (Eq. 4.6): (i) biotite dissolution, $[H^{+}_{dis}]$, (ii) calcite dissolution $[H^{+}_{carb}]$ and (iii) hydrolysis of aqueous cations, $[H^{+}_{hy}]$, such that $[H^{+}_{sol}]$ can be written as:

$$[H^{+}_{sol}] = [H^{+}_{dis}] + [H^{+}_{carb}] + [H^{+}_{hy}]$$

Eq. 4.6

Similarly, two reactions can incorporate protons onto or into the mineral surface (Eq. 4.7): (i) metal exchange reactions, $[H^{+}_{ex}]$, and (ii) proton adsorption, $[H^{+}_{ad}]$ and therefore $[H^{+}_{surf}]$ can be written as:

$$[H^{+}_{surf}] = [H^{+}_{ex}] + [H^{+}_{ad}]$$

Eq. 4.7

Combining Eqs. (4.5), (4.6), and (4.7) allow formulation of the following expression for the total number of protons consumed via aqueous solution-based and mineral surface reactions (Eq. 4.8):

$$[H^{+}_{s}] = [H^{+}_{dis}] + [H^{+}_{carb}] + [H^{+}_{hy}] + [H^{+}_{ex}] + [H^{+}_{ad}]$$

Eq. 4.8

Details on these five proton-related reactions are presented below with representative worked examples outlined in Appendix B.

4. 3. 1. Biotite dissolution reactions

In this study, biotite dissolution was assumed to be stoichiometric and consistent with Si release, thus the dissolution reaction can be represented as:

$$\sum_{i}(\boldsymbol{n}_i z_i)H^+ + \sum_{i}(\mathrm{M_i})_{\boldsymbol{n}_i}\mathrm{SiO}_{2+\sum_i\left(\frac{\boldsymbol{n}_i z_i}{2}\right)} = \sum_{i}\left(\boldsymbol{n}_i \mathrm{M_i}^{z_i}\right) + \mathrm{SiO_2}(aq) + \sum_{i}\left(\frac{\boldsymbol{n}_i z_i}{2}\right)\mathrm{H_2O}$$

Eq. 4.9

where n_i refers to the stoichiometric coefficient of metal M_i in the biotite formula, normalized to one Si, and z_i the charge of the M_i *th* free ion in aqueous solution. Through the dissolution of one biotite molecule $\sum_i(\boldsymbol{n}_i z_i)$ protons are consumed. Therefore, the number of protons consumed by dissolution, $[H^+_{dis}]$, is proportional to the number of Si atoms released to the fluid, so that:

$$[\mathrm{H^+_{dis}}] = \sum_{i}(\boldsymbol{n}_i z_i)\,[\mathrm{Si_s}]$$

Eq. 4.10

where $[Si_s]$ (atoms nm^{-2}) is the surface area normalized number of Si atoms released into aqueous solution during the titration.

4. 3. 2. Calcite dissolution reactions

The quantitative XRD analyses of our starting material revealed the presence of 3.7 wt % calcite. The release of 1 mole of Ca from calcite dissolution is accompanied by the release of 1 mole of CO_3^{2-}. The released CO_3^{2-} is present in solution as either CO_3^{2-}, HCO_3^- or H_2CO_3, depending on pH, with the latter two species consuming 1 and 2 protons respectively. In a CO_2 free system, the total carbonate concentration $[carbonate_s]$ (atoms nm^{-2}) is equal to the calcium concentration released from calcite dissolution $[Ca_{carb,\ s}]$ (atoms nm^{-2}). This can be calculated from:

$$[\text{carbonate}_s] = \left[\text{Ca}_{\text{carb,s}}\right] = [\text{Ca}_s] - \boldsymbol{n}_{\text{Ca}}[\text{Si}_s]$$

Eq. 4.11

where, $[Ca_s]$ represents the surface area normalised total calcium concentration, $n_{Ca}[Si_s]$ represents the contribution of Ca released from biotite dissolution. The concentrations of the carbonate species are calculated using the PHREEQC 3 computer code (Parkhurst and Appelo, 2013) and proton consumption by calcite dissolution $[H^+_{carb}]$ based on:

$$[\text{H}^+_{\text{carb}}] = ([\text{H}_2\text{CO}_3] \times 2) + [\text{HCO}_3^-]$$

Eq. 4.12

where, $[H_2CO_3]$ and $[HCO_3^-]$ represent the concentrations of carbonic acid and bicarbonate in aqueous solution, respectively.

4. 3. 3. Aqueous Hydrolysis

The hydrolysis of aqueous metals in aqueous solution can be written as:

$$\text{M}_\text{i}^{z+} + \boldsymbol{n}_\text{H}\text{H}_2\text{O} = \text{M}_\text{i}\text{OH}^{(z_\text{i}-\boldsymbol{n}_\text{H})}_{\boldsymbol{n}_\text{H}} + \boldsymbol{n}_\text{H}\text{H}^+$$

Eq. 4.13

where n_H is the stoichiometric coefficient. In addition, above pH 9, silicic acid dissociates following:

$$\text{SiO}_2 + 2\text{H}_2\text{O} = \text{H}_3\text{SiO}_4^- + \text{H}^+$$

Eq. 4.14

and therefore the net proton change induced by hydrolysis, normalised to mineral surface area, can be written:

$$\left[\text{H}^+_{\text{hy}}\right] = \left(\frac{\boldsymbol{N}(\boldsymbol{M_a} + \boldsymbol{M_e})}{\boldsymbol{Ms}10^{18}}\right)\left(-\sum\left(\boldsymbol{n}_\text{H}\boldsymbol{m}_{\text{M}_\text{i}\text{OH}^{(z_\text{i}\boldsymbol{n}_\text{H})+}_{\boldsymbol{n}_\text{H}}}\right) - \boldsymbol{m}_{\text{H}_3\text{SiO}_4^-}\right)$$

Eq. 4.15

$[H^{+}_{hy}]$ (atoms nm^{-2}) is calculated by combining Eq. (4.13) with speciation calculations performed using the PHREEQC 3 computer code (Parkhurst and Appelo, 2013).

4. 3. 4. Metal-proton exchange reactions

In addition to stoichiometric dissolution of biotite, a fraction of total dissolved metals can be attributed to metal-proton exchange reactions. The amount of dissolved metals solubilised via exchange reactions can be calculated as:

$$[M_{i,ex}] = [M_{i,s}] - \boldsymbol{n}_i[Si_s]$$

Eq. 4.16

where $[M_{i,ex}]$ (atoms nm^{-2}) represents the number of M_i atoms exchanged from biotite during each batch titration experiment and $[M_{i,s}]$ (atoms nm^{-2}) represents the number of M_i atoms released to aqueous solution, normalised to the measured biotite surface area, while $n_i[Si_s]$ represents the concentration of the *ith* element ascribed to stoichiometric dissolution. Metal exchange from a surface can coincide with proton consumption:

$$> M_i + \boldsymbol{n}_{M_{i,ex}} H^{+} = M_i^{z_i+} + > H^{\left(\boldsymbol{n}_{M_{i,ex}} - z_i\right)+}_{\boldsymbol{n}_{M_{i,ex}}}$$

Eq. 4.17

where $>M_i$ and $> H^{\left(\boldsymbol{n}_{M_{i,ex}} - z_i\right)+}_{\boldsymbol{n}_{M_{i,ex}}}$ stand for a mineral surface site filled with a metal or proton respectively, and $\boldsymbol{n}_{M_{i,ex}}$ denotes the number of protons consumed by the mineral surface for the exchange of one M_i atom. Therefore, the total number of protons that could be consumed by all exchange reactions ($[H^{+}_{ex}]$), if charge is conserved, is equal to:

$$[H^{+}_{ex}] = \sum_i \left(\boldsymbol{n}_{M_{i,ex}}\right)[M_{i,ex}]$$

Eq. 4.18

The reaction in Eq. 4.17 allows for the replacement of M_i with more or less protons than is necessary for charge balance. A number of previous studies have concluded that charge balance is not always retained during metal-proton exchange reactions. For example, Oelkers et al. (2009) reported that 3.8 protons are consumed by the removal of each Mg from forsterite, 3.1 to 3.3 protons are consumed by the removal of each Mg or Ca from diopside or enstatite, and 1.4 protons are consumed by the removal of Ca from wollastonite. Yet, such a non-conservation of charge is not necessarily true for all metal exchange reactions, and for example, albite dissolution has been interpreted to proceed via charge conservation with respect to Al exchange (Oelkers et al., 2009). This aspect is discussed in more detail below.

4. 3. 5. Surface adsorption

The last aspect of proton consumption that needs to be considered is the adsorption and desorption of protons from hydroxyl surface sites, following the generic reactions:

$$> M_iOH^0 + H^+ = > M_iOH_2^+$$

Eq. 4.19

and

$$> M_iOH^0 = > M_iO^- + H^+$$

Eq. 4.20

The proportion of these reactions to the total proton consumption ($[H_{ad}^+]$) can be calculated using Eq. (4.8), after first calculating the contributions from dissolution, hydrolysis and metal-proton exchange processes. Eqs. 4.1 to 4.20 are used below to interpret proton consumption by reactions occurring at the biotite surface during batch titration reactions. Results are discussed in terms of atoms nm^{-2}, allowing ready comparison to pre-existing literature data on mineral surface reactive site density.

4. 4. RESULTS

Results show that the concentration of protons consumed by biotite, during the titration series, increases with decreasing pH. The minimum proton consumption occurs at pH ~ 10, consistent with the immersion pH (pH_{imm}). The total amount of metals released from dissolution and metal-proton exchange reactions increases with decreasing pH. Electrokinetic measurements performed over 3 orders of magnitude of ionic strength yielded an isoelectric point at pH ~ 3. These results will be presented in detail below.

4. 4. 1. Batch potentiometric titrations

4. 4. 1. 1. Proton consumption

Total proton consumption during the 65 biotite-bearing batch experiments performed in this study is shown in Fig. 4.1. It can be seen that proton consumption during the 20 minute titration series are identical, within uncertainty, to the corresponding proton consumption during the 60 minute titrations (Fig. 4.1A). The pH values of the biotite suspension after the immersion period (pH_{imm}, also depicted in Fig. 4.1A) yield an average of 9.66 (S.D. 0.24; n = 7). The batch titration series from biotite-bearing and biotite-free experiments yield two distinct functions and are presented on a plot of $\log[H^+]_{t=0}$ against pH in Fig. 4.1B. The results shown in Fig. 4.1B appear to be independent of the fluid ionic strength (e.g., NaCl concentration). In all cases, the pH of the biotite-free series is lower than the corresponding pH in the biotite-bearing reactors, indicating that fluid-biotite interaction consumed protons during the titrations. At a given pH, the difference between these two curves corresponds to $[H^+_s]$, as defined in Eq. (4.4), and calculated using the cubic regression of the biotite-free titration results shown in Fig. 4.1B.

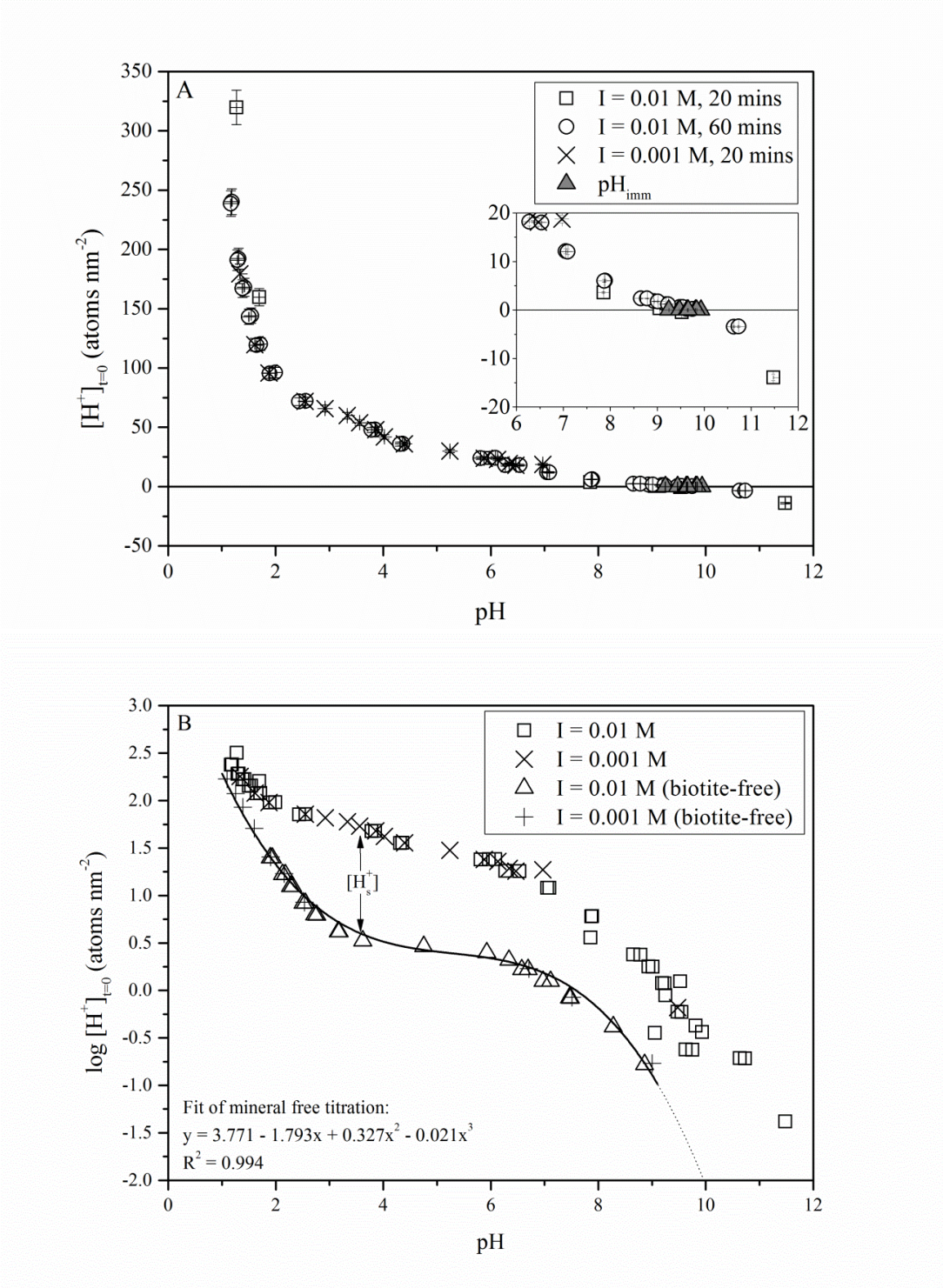

Figure 4.1

Concentration of protons in the batch titration reactors at time zero ($[H^+]_{t=0}$, atoms nm^{-2}) against final measured pH (t=20 or 60 minutes) at 25 °C and *I* of 0.01 or 0.001M. Note the difference in y-axis of the plots with A) linear, and B) logarithmic. Values of 0 $[H^+]_{t=0}$ in Fig. 4.1A indicate the immersion pH (pH_{imm}), shown more clearly in the inset graph. Note also the two distinct curves in Fig. 4.1B, the lower curve represents data from biotite free titrations ($[H^+_0]$ and is fitted with a cubic regression resulting in the formula given, p=0.003. The difference between the two curves in Fig. 4.1B is the value of $[H^+_s]$ as calculated in Eq. (4.4). The uncertainty of each data point yields error bars within the symbol (± 4.5% for $[H^+]_{t=0}$ and ± 0.002 pH).

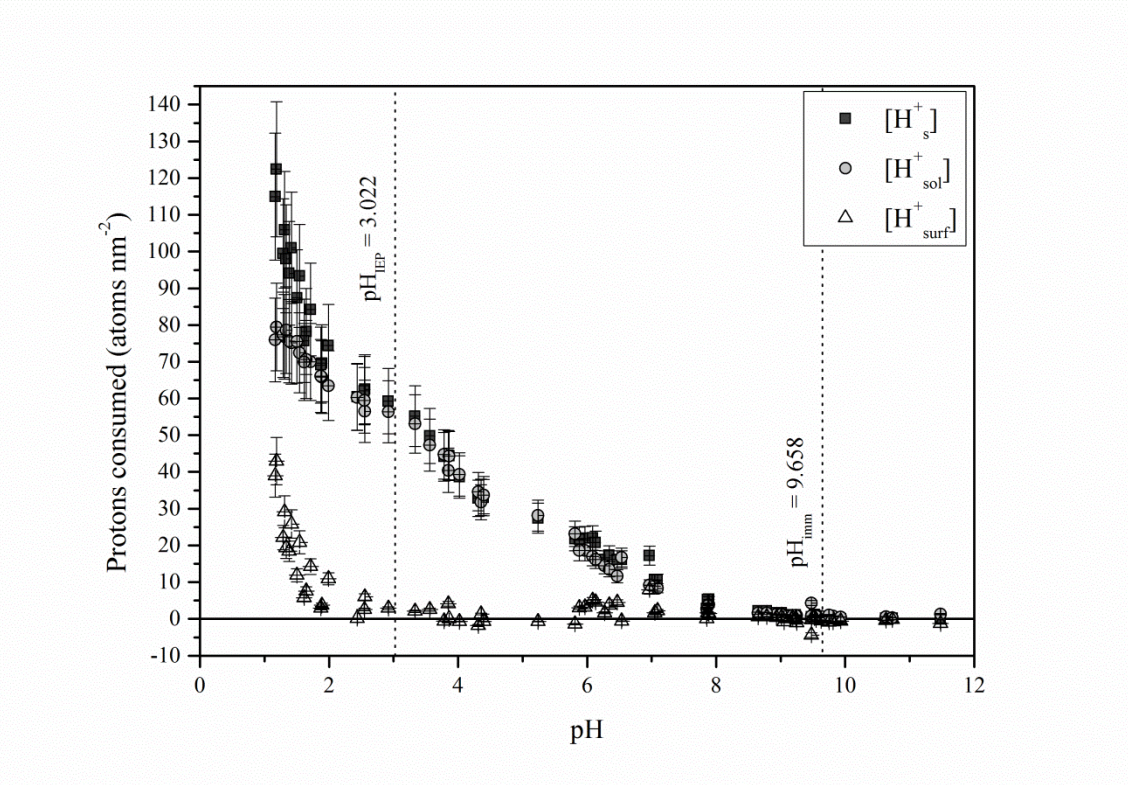

Figure 4.2

Number of protons consumed by [H^+_s], [H^+_{sol}] and [H^+_{surf}] (atoms nm^{-2}) plotted as a function of pH. Error bars represent a 15% [H^+] and 0.002 pH unit uncertainties. The dashed lines correspond to the pH_{IEP} and pH_{imm} for the Grasåsen biotite, as determined in this study.

The number of protons consumed by all reactions occurring in the presence of the biotite, [H^+_s], dramatically changes with pH (Fig. 4.2). At pH ~ 1, this value exceeds 100 atoms nm^{-2}, and decreases to zero at the immersion pH (pH_{imm}). The [H^+_{sol}] and [H^+_{surf}] values shown in Fig. 4.2 were calculated using Eqs. (4.5) and (4.6) and correspond to the number of protons consumed via dissolution and metal hydrolysis, and metal-proton exchange and adsorption, respectively. It should be noted that [H^+_{sol}] is similar to [H^+_s] above pH ~3, meaning that the contribution of [H^+_{surf}] is approximately 0 in this region.

4. 4. 1. 2. Dissolution dependent and independent metal release

The surface area and biotite-stoichiometry normalised concentration of metal M_i removed from the biotite near-surface during the timed batch titrations ([$M_{i,s,b}$], Fig. 4.3),

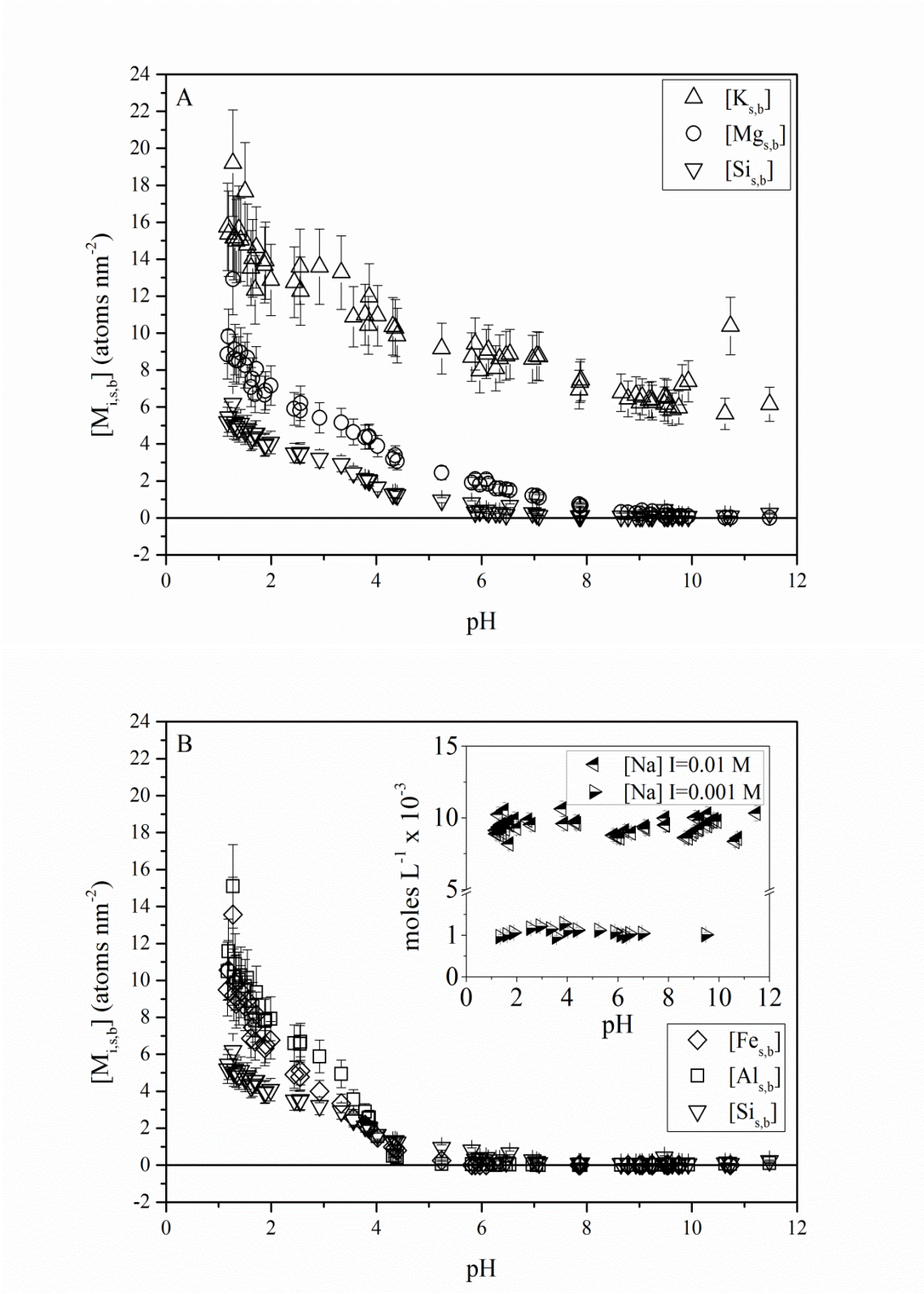

Figure 4.3

Quantity of metals released from the biotite surface during batch titrations, normalised to mineral surface area present in the reactor and mineral stoichiometry, ([$M_{i,s,b}$], atoms nm^{-2}) plotted as a function of pH for; (A) [$K_{s,b}$], [$Mg_{s,b}$] and [$Si_{s,b}$], and (B) [Fe_{sb}], [$Al_{s,b}$] and [$Si_{s,b}$]. The concentration the background electrolyte (Na, corrected for NaOH addition, moles L^{-1} x 10^{-3}) is plotted as a function of pH in the inset of B. Error bars represent uncertainty of 15% [$M_{i,s,b}$], [Na] and 0.002 pH units.

decreases with increasing pH. From 16 to 6 atoms nm^{-2} of potassium is removed from the biotite surface from pH 1 to 12 respectively (Fig. 4.3A). Approximately 6 atoms nm^{-2} of K are released immediately at the start of the titration as indicated by the value of K released at pH_{imm}. The release of magnesium, iron, aluminium, and silicon (Fig. 4.3A and 4.3B), systematically increases with decreasing pH, with silicon being released least from the biotite near-surface when normalized to the solid phase composition. Consistent with the theoretical formalism described above (section 4.3.1, Eqs. 4.9 and 4.10), Si release is attributed solely to biotite dissolution, while the release of the other metals is attributed to a combination of dissolution and metal-proton exchange reactions. The concentrations of several minor and trace metals released from the biotite near-surface during batch titrations are listed in Table A-1 along with the concentration of the background electrolyte (NaCl, see Na) which is also presented in the inset of Fig. 4.3B. It is worth noting that the high concentrations of Ca found in the aqueous solutions is consistent with the dissolution of approximately 3.2 ± 0.5 wt. % calcite, comparable to the 3.4 to 3.7 wt. % calcite present in the biotite powder, as determined by XRF and XRD.

The release of metals from the biotite near-surface by exchange reactions ($[M_{i,ex}]$) is also highly pH dependent (Fig. 4.4). Using Fig. 4.4 we can highlight a number of important observations. First, by definition, a metal exchange, $[M_{i,ex}]$, value of 0 atoms nm^{-2} indicates stoichiometric dissolution, while $[M_{i,ex}] > 1$ indicates preferential release and $[M_{i,ex}] < 1$ indicates preferential retention (Fig. 4.4). Results show that at the pH of immersion (pH_{imm}, 9.66) ~6 K atoms nm^{-2} are released. As the stoichiometric release of K from dissolution (based on the average Si concentration at pH_{imm}) is 0.16 atoms nm^{-2}, at the immersion pH, ~97% of the K in solution is a result of metal-proton exchange. With decreasing pH, $[K_{ex}]$ increases systematically, attaining a maximum value of approximately 10 atoms nm^{-2} at pH 1, where dissolution contributes only ~38% of dissolved K in the fluid. In contrast, $[Mg_{ex}]$, $[Fe_{ex}]$, and $[Al_{ex}]$ are close to 0 atoms nm^{-2} at

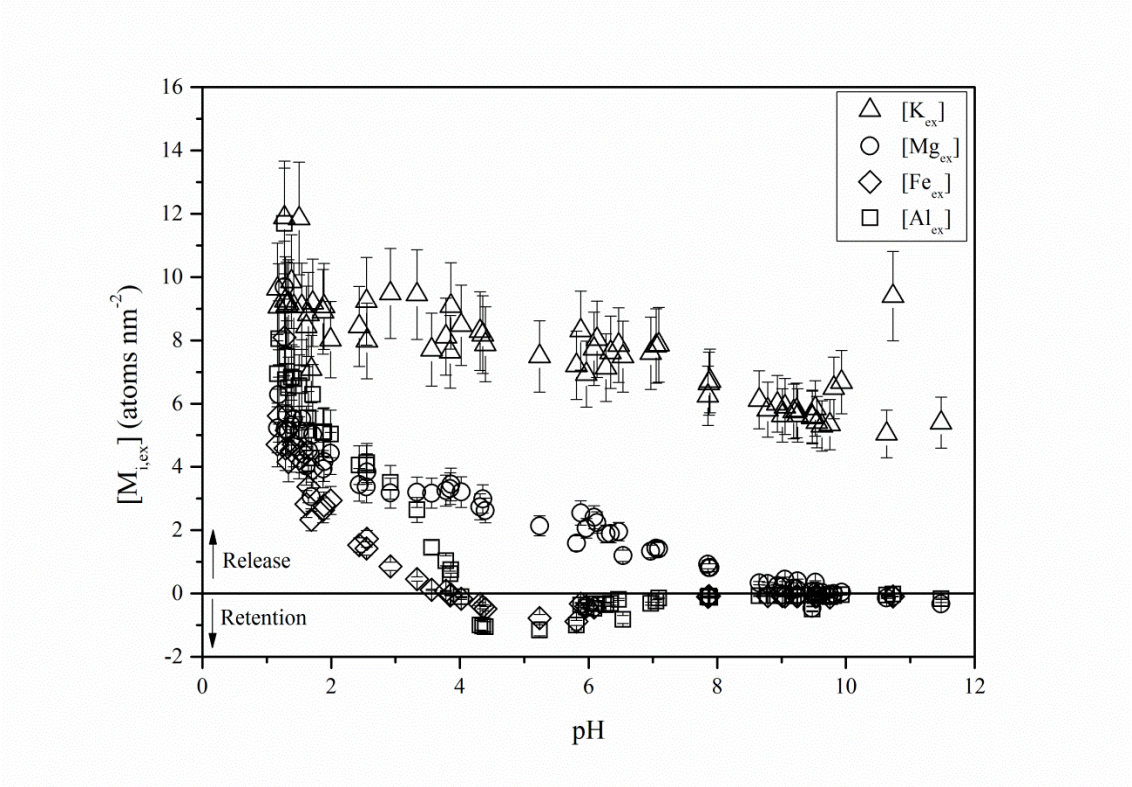

Figure 4.4

Quantity of metals exchanged from the biotite surface, normalised to surface area, ($[M_{i,ex}]$, atoms nm^{-2}, Eq. 4.14) as a function of pH. The solid line where $[M_{i,ex}] = 0$ indicates stoichiometric biotite dissolution. Error bars represent an uncertainty of 15% in $[M_{i,ex}]$ and 0.002 pH units.

the pH_{imm}. With decreasing pH, $[Mg_{ex}]$, $[Fe_{ex}]$, and $[Al_{ex}]$ increase steadily with decreasing pH when pH is less than ~9, ~4 and ~4, respectively, reaching between 6 to 10 atoms nm^{-2} at pH ~ 1. Furthermore, $[Fe_{ex}]$ and $[Al_{ex}]$ are both negative at pH between 4 and 8, while $[Mg_{ex}]$ is negative at the most alkaline pH values (> 10.5). This suggests that at these conditions, these metals are preferentially retained by the biotite surfaces.

4. 4. 2. Electrokinetic measurements

The ζ potential values of the ground biotite particles in aqueous solutions of ionic strength from 0.001 to 0.1M NaCl converge at zero ζ (Fig. 4.5). The point of zero ζ is the isoelectric point (pH_{IEP}) and occurs at pH 3.02. The pH_{IEP} of biotite in this study is listed in Table 4.1 together with the values of pH_{IEP} of other comparable minerals from

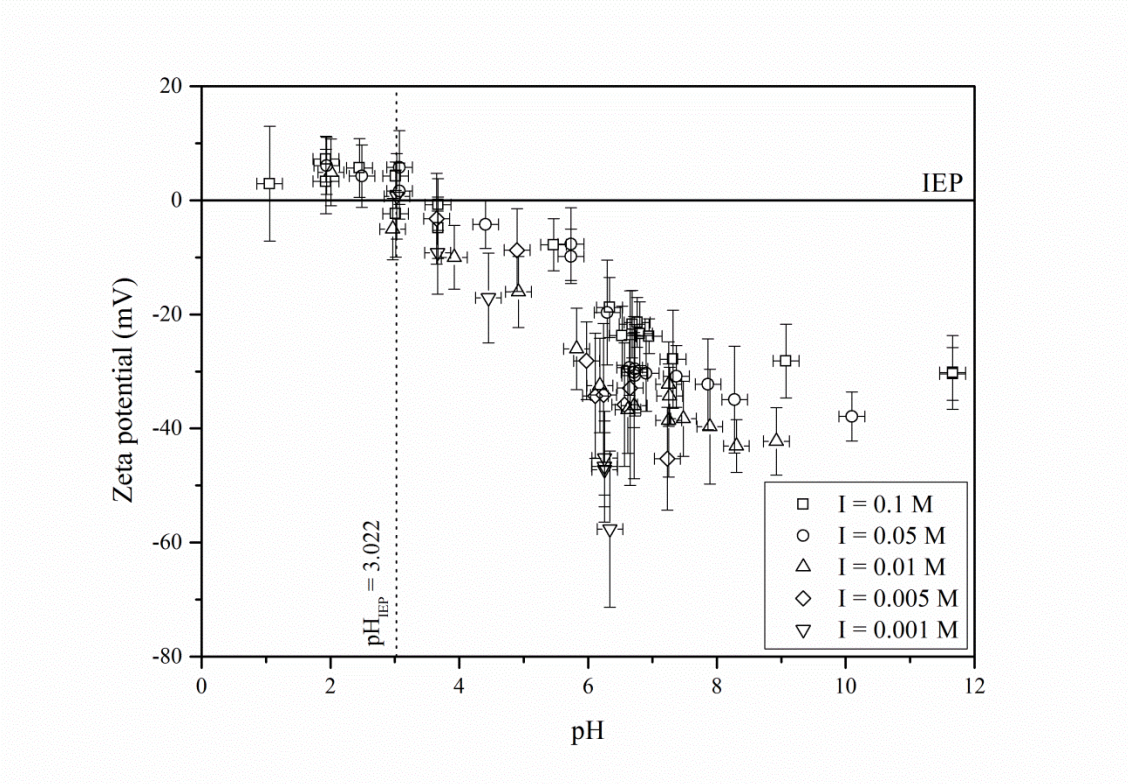

Figure 4.5

Zeta potential (mV) at five ionic strengths plotted against pH. The dashed line corresponds to the pH where zeta potential = 0, pH_{IEP}. Error bars represent 2 standard deviations of each zeta potential and 0.2 pH units.

literature. The full list of electrophoretic motilities measured, and corresponding ζ-potential can be found in Table A-3 in Appendix A.

4. 5. DISCUSSION

4. 5. 1. Non-stoichiometric metal release and charge conservation

The degree to which metal exchange reactions are charge balanced by protons can be assessed with the aid of Fig. 4.6. For charge balance, the sum of equivalence of the released metals (concentration of exchanged metals multiplied by corresponding charge) should correspond to the number of protons consumed by surface reactions [H^+_{surf}], indicated by y = x line. Charge balance can occur either by H^+ incorporation into the structure [H^+_{ex}] or H^+ adsorption onto the mineral surface, both of which are accounted

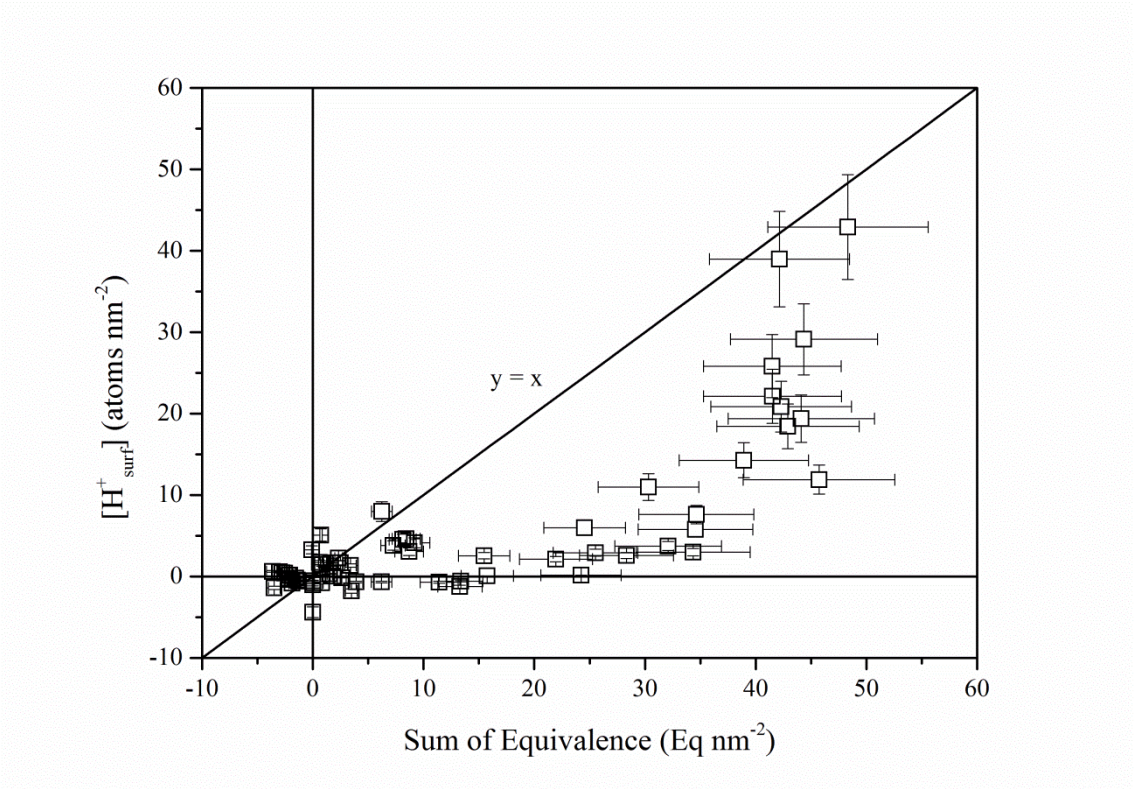

Figure 4.6

Plot of $[H^{+}_{surf}]$ (atoms nm^{-2}) against the sum of equivalence for exchanged metals, $\sum([M_{i,ex}] \times z_{M_i})$, excluding K_{ex}. Error bars 15% uncertainty in the calculation of both $[H^{+}_{surf}]$ and the sum of equivalence.

for in $[H^{+}_{surf}]$. As can be seen in Fig. 4.6, the relationship between total equivalence and $[H^{+}_{surf}]$ is far from 1:1. As there is a proton consumption deficit, it appears that metals are removed from the biotite structure without significant charge conservation.

The non-conservation of charge due to metal release is supported by the pH_{IEP} value of 3.02 obtained for this biotite. This value is lower than the calculated pH_{ZPC} and pH_{ZNPC} (see section 5.3 for details) and can be explained by the observed metal release. If metals are released without a compensating incorporation of protons, the surface becomes increasingly negative. The combination of a relatively negative near-surface and the tendency of the surface to become Si-O rich, causes the isoelectric point (pH_{IEP}) to be at a lower pH than that which would be estimated from a sum of oxide mineral pH_{ZPC} and pH_{ZNPC} values.

At pH < pH_{IEP} (pH < ~3) [H^{+}_{surf}] increases significantly (Fig. 4.2). This can be attributed to the consumption of protons by adsorption onto the biotite surface. Consistent with the non-conservation of charge of metal release, the remaining consumption of protons by surface reactions [H^{+}_{surf}] corresponds to proton adsorption. In this pH region, where the surface of biotite is predominantly Si, the adsorption of H^{+} forms partly detached silanol groups.

The relative contributions of proton consumption are presented in Fig. 4.7. Dissolution reactions, [H^{+}_{dis}] and [H^{+}_{carb}] dominate proton consumption (Fig. 4.7A). The contribution from metal hydrolysis [H^{+}_{hy}] is negligible at all pH, as at low pH, metals in solution are present as single ions and at high pH, the aqueous concentration of dissolved metals is too low to contribute significantly. As mentioned above, [H^{+}_{ex}] and [H^{+}_{ad}] are relatively insignificant at pH > 3 (Fig. 4.7B).

4. 5. 2. Biotite surface composition as a function of pH

The results summarised above provide insight on how the surface chemistry of biotite varies as a function of the pH of the adjacent fluid. An understanding of the degree to which the biotite near-surface is altered by interaction with the adjacent fluid phase is aided by the calculation of the average bulk depletion depth of the major constituent metals (Dep_{M_i}).

$$Dep_{M_i} = \frac{[M_{i,ex}]}{\boldsymbol{nb}_{M_i}\left(\frac{\boldsymbol{\rho}_{biotite}}{m_{biotite}} \cdot \frac{\boldsymbol{N}}{10^{21}}\right)}$$

Eq. 4.21

The average bulk depth of metal M_i depletion (Dep_{M_i}) is calculated by dividing [$M_{i,ex}$] by the average density of metal atoms M_i in the biotite structure (atoms nm^{-3}), where $\boldsymbol{nb}_{M_i}$ represents the stoichiometric coefficient of the M_i*th* metal in the bulk biotite, $\rho_{biotite}$ (g cm^{-3}) signifies the biotite density (3.09, average from webmineral.com) and

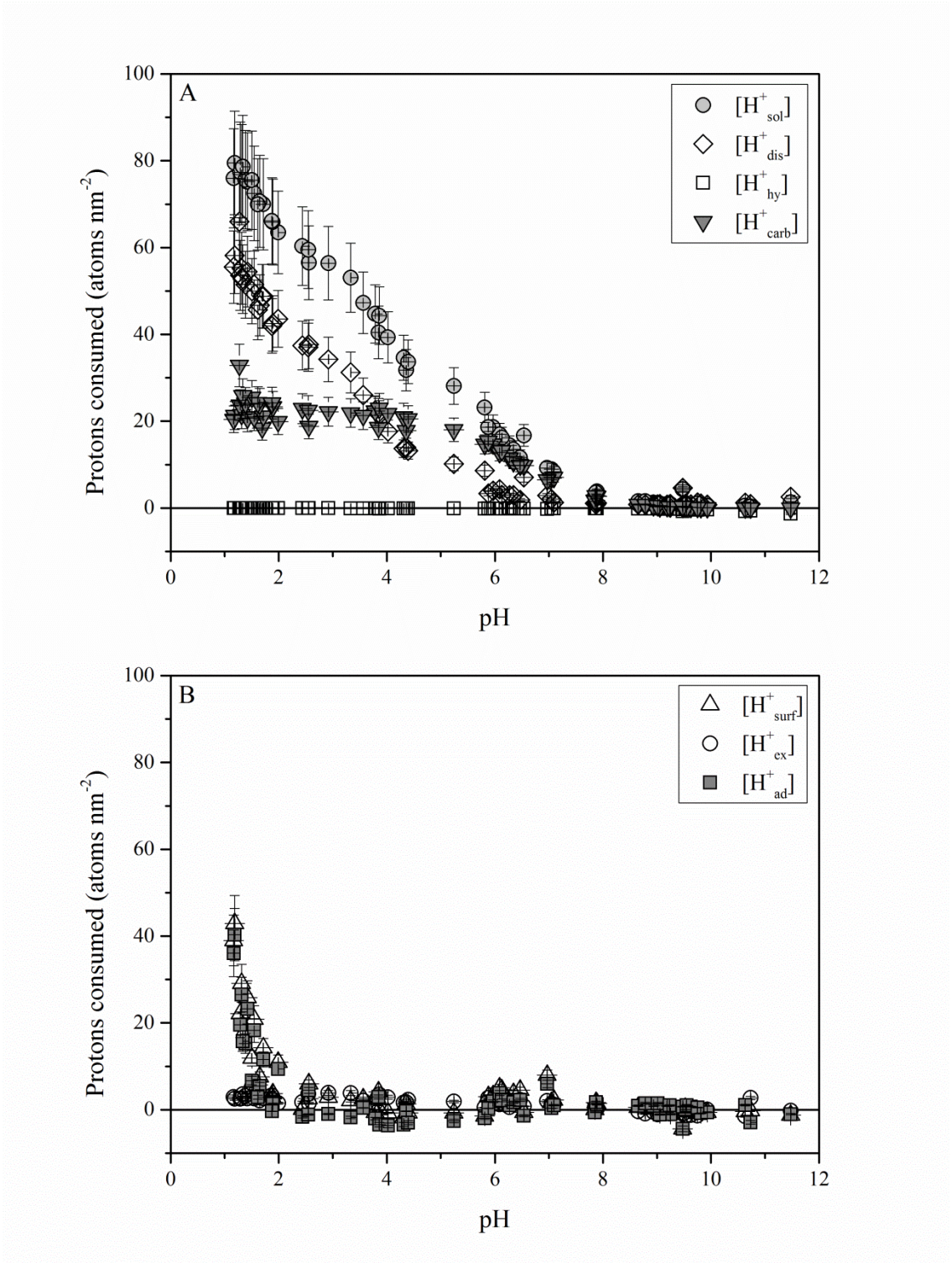

Figure 4.7

Proton consumption as a function of pH for A) [H^+_{sol}] reactions and, B) [H^+_{surf}] reactions. [H^+_{sol}] reactions in 4.7A include dissolution reactions ([H^+_{dis}] and [H^+_{carb}]) and aqueous metal hydrolysis ([H^+_{hy}]). [H^+_{surf}] reactions in 4.7B include metal exchange reactions ([H^+_{ex}]) and proton adsorption ([H^+_{ad}]). Error bars represent 15% uncertainty in [H^+] and 0.002 pH unit uncertainty.

$m_{biotite}$ (g mol^{-1}) the molecular mass of biotite (450.15 g mol^{-1}, for the Graså sen biotite). Dep_{M_i} is calculated assuming that there is an abrupt change between the near-surface that is affected by the metal exchange reactions (i.e. a metal-free zone) and the bulk, non metal exchanged, mineral. The average depletion depth of each metal is illustrated as a function of pH in Fig. 4.8

As can be seen in Fig. 4.8, potassium is calculated to be totally removed from biotite to a depth of ~1.5 nm at pH_{imm}. The Dep_K due to the titration alone can be calculated by subtracting the value of Dep_K at pH_{imm}. Charge balance constraints suggest that this K removal is accompanied by the incorporation of compensating positive ions into the biotite. This compensating positive charge can be partially attributed to the incorporation of H^+ into the interlayer sites, as demonstrated by the values of pH_{imm}

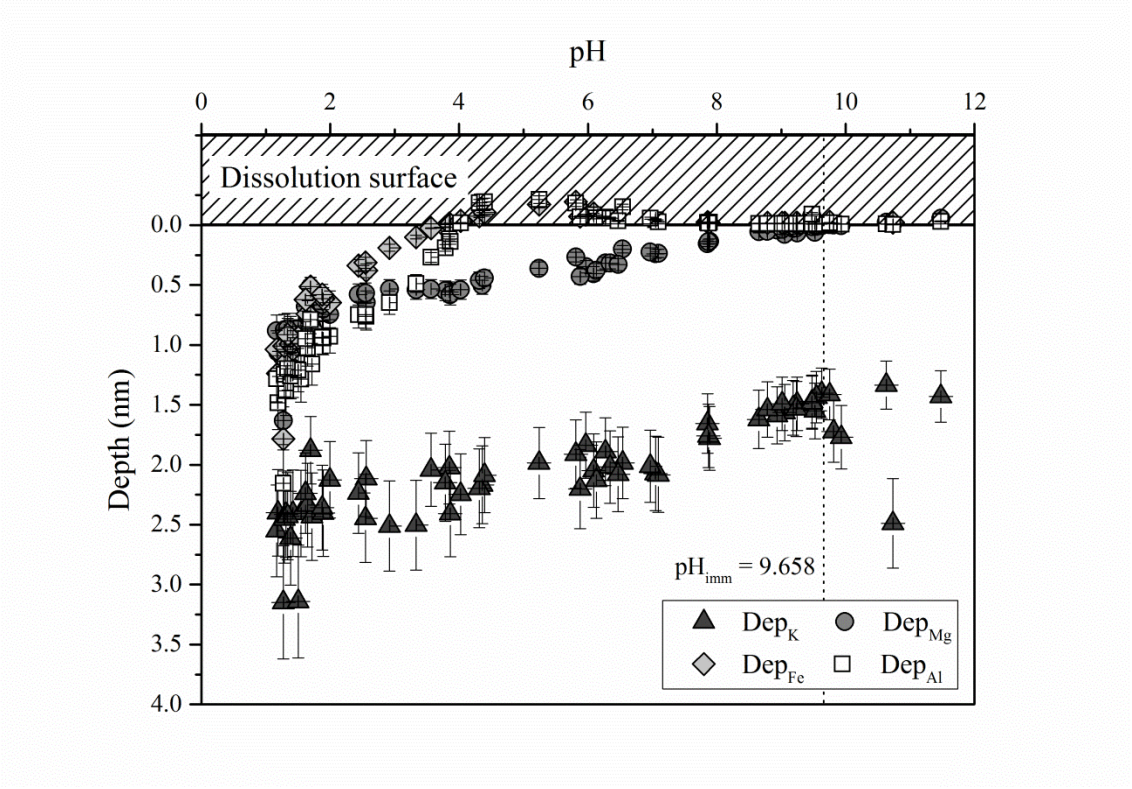

Figure 4.8

Average bulk depth of depletion of exchanged metals from the dissolution surface as a function of pH. Depletion depth was calculated using Eq. (4.19). Error bars represent a 15% uncertainty in calculated depth and 0.002 pH uncertainty.

ranging from pH 9.2 to 10 (Table A-1). However, a 1:1 charge compensation would require 10^{-3} protons, far exceeding the observed increase in pH from a theoretical pH 7 (computed due to the absence of CO_2) to pH_{imm}. This, therefore, leaves two possibilities, either (1) the charge is compensated by a different mono or divalent cation, or (2) K^+ release is not completely charge conservative. Taking the first option, it is possible that Na from the background electrolyte could substitute in the structure for K. If Na for K substitution was responsible for a complete charge compensation then it could be expected that Na concentrations would change substantially from the original concentration during the immersion period. The degree to which this happens can be assessed through figure 4.3B and Table A-1. As the concentration of Na does not significantly change with pH it is more feasible that the release of K^+ is non charge conservative.

In contrast, Dep_{Mg} from the biotite surface increases continuously with decreasing pH. Similar to the behaviour of the magnesium in diopside and fosterite (Oelkers et al., 2009), magnesium in biotite is preferentially retained by the mineral at pH >10, and increasingly depleted at pH < 8. Notably, the average magnesium depletion depth at neutral conditions ranges from 0.2 to 0.5 nm. As the concentration of Mg in the biotite structure is 5.9 atoms nm^{-3} (Eq. 21), the depletion depth results (Fig. 4.8) suggest that 1 to 3 atoms nm^{-2} of Mg would have been removed from the biotite surface at the pH of most natural waters. This depletion corresponds to 20 to 50% Mg removal from the first unit cell of biotite.

The behaviour of Dep_{Al} and Dep_{Fe} exhibit similar variations with pH at the biotite surface (Fig. 4.8). Both metals are present in the mineral in close-to-stoichiometric quantities at pH greater than 8. Al and Fe are preferentially retained by the solid phase from pH 4 to 8 and removed to an increasing depth with decreasing pH when pH < 4. This preferential retention of Fe and Al by the solid phase at pH 4 to 8, and Mg above pH

10, may originate from either secondary phase precipitation or preferential retention by the biotite. The former possibility is supported by the calculated saturation state of the fluid phase during the titrations (Fig. 4.9). Between pH 4 and 11, aluminium and iron oxy-hydroxides are both supersaturated in the fluid phase while some Mg-rich clays are supersaturated in the fluid phases of the titrations performed at pH > 9. Comparing the dissolved concentrations of Al and Fe at pH (4-8) to that found at the pH_{imm} indicates precipitation. It is therefore likely that Al and Fe oxy-hydroxides formed in these experiments on the biotite surfaces.

These values of Dep_{M_i} are calculated assuming an isotropic biotite structure. Phyllosilicates are, however, highly anisotropic. The actual metal depletion depth (Dep_{M_i}) in biotite is likely to be highly heterogeneous due to the nature of the biotite surfaces (e.g., edges vs. basal surfaces). Turpault and Trotingnon (1994) and Hodson (2006) have shown biotite edge surfaces are between 36 and 240 times more reactive than the [001] basal. This phenomena suggests that depletion in the current study is likely far greater at the edges than at the basal surfaces. For example, if we assume that the edges comprise 5% of the total geometric surface area (e.g. Bonneville et al., 2011), and the edge:basal surface reactivity ratio is 71:1 (Hodson, 2006), we can calculate the relative depletion depths at the edge and basal surfaces. Note the assumption that edge surfaces are 5% of the total surface area may be a conservative estimate as this ratio increases with decreasing particle size. In the case of potassium, such a calculation presents depletion depths between 30 to 40 nm at the edges and up to 0.5 nm at the basal surface (Fig. A-2).

Taken together, these observations demonstrate that the biotite surface composition depends strongly on fluid pH. At basic conditions (pH > 8), biotite surfaces contain approximately stoichiometric proportions of Mg, Fe, Al and Si, but K seems to be completely depleted to a bulk average depth of 1.5 nm. At neutral conditions (pH 4 to 8),

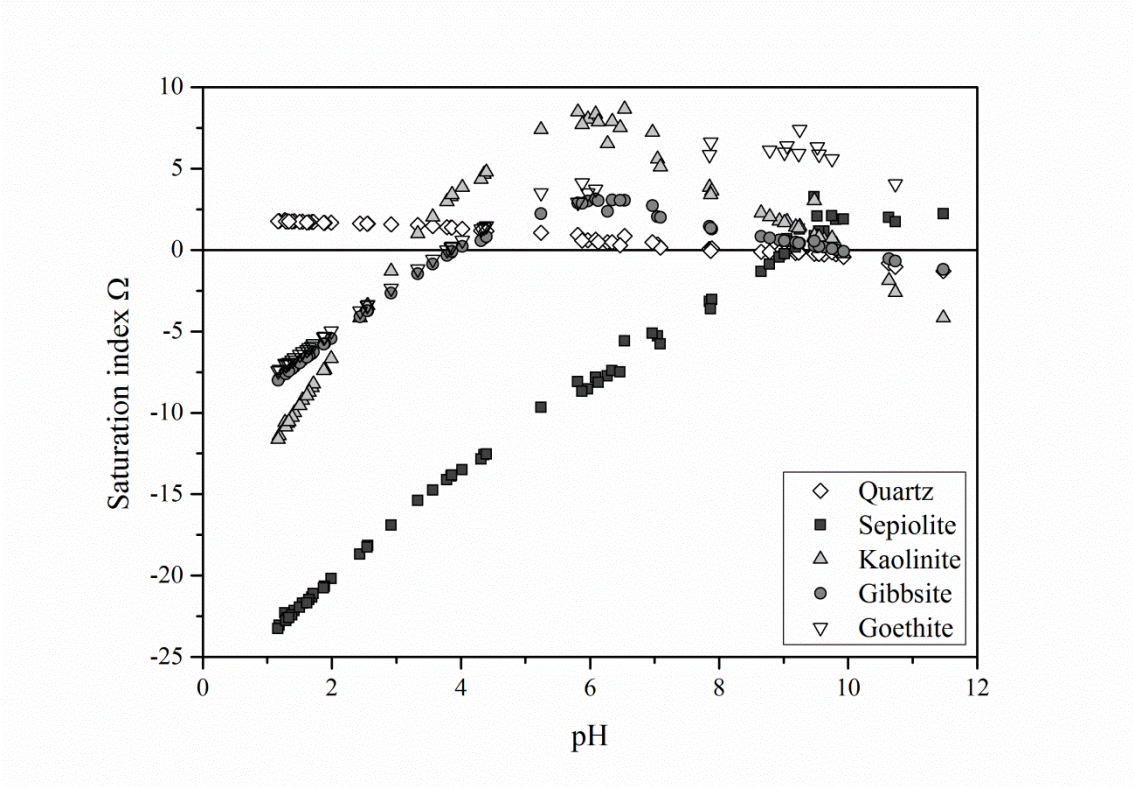

Figure 4.9

A plot of saturation index of possible secondary phases in the titration experiments, as a function of pH. Phases include, Quartz (SiO_2), Sepiolite ($Mg_4Si_6O_{15}.(OH)_26H_2O$), Kaolinite ($Al_2Si_2O_5(OH)_4$), Gibbsite ($Al(OH)_3$) and Goethite (FeOOH). Saturation indicies were calculated using PHREEQC 3 (Parkhurst and Appelo, 2013).

biotite surfaces are Fe and Al enriched and Mg and K poor, relative to Si. At acid conditions (pH < 4), the biotite surfaces contain partly detached silanol groups, >Si-OH^0, following the removal of most of the univalent, divalent and trivalent metals. Additionally, at very low pH (< 2) the bulk average metal depletion depth appears to increase dramatically (from 0.5 to 1.5 nm) with decreasing pH. Sheet silicates have been observed to preferentially dissolve parallel to the basal plane at low pH, promoting the removal of metals from deep within the mineral structure (Kaviratna and Pinnavaia, 1994; Turpault and Trotignon, 1994; Bickmore et al., 2001; Bickmore et al., 2003; Saldi et al., 2007). Saldi et al. (2007) presented photomicrographs displaying the fanning out of talc edges, exposing an increased reactive surface area. Such a mechanism could be

responsible for the increased metal release from biotite we observe below pH 2 (Figs. 4.3, 4.4 and 4.8).

4. 5. 3. Biotite surface chemistry and charge

The results described above indicate that the surface composition of biotite differs significantly from the bulk, implying that the adsorption properties of biotite and phyllosilicates in general, likely differ significantly from predictions made solely from the bulk mineral compositions. For example, the pH_{ZPC} is commonly used to discuss surface charge. Although this has not been directly determined in this study, a number of approaches can be used to estimate pH_{ZPC}. For example, Parks (1967) suggested that the surface charge of multi oxide minerals can be estimated from the weighted sum of the constituent oxides, as used by Jara et al. (2005),

$$pH_{ZPC} = \sum_{i} pH_{IEP,i} \boldsymbol{X_i}$$

Eq. 4.22

where X_i corresponds to the mole fraction of the ith oxide and $pH_{IEP,i}$ refers to the isoelectric point of the ith oxide. Using this approach, the pH_{ZPC} for biotite can be estimated to be 4.12 (Table 4.1). In contrast, the measured pH_{IEP} for biotite is 3.02, a value which is likely influenced by the observed metal depletion. Note the presence of calcite has little effect on the pH_{IEP} as it appears to have completely dissolved at pH < 4.

The biotite pH_{imm} value observed in this study (9.66), is vastly different from the measured pH_{IEP} (3.02) and calculated pH_{ZPC} (4.12). In a number of past studies, pH_{imm} has been assumed to equal pH_{ZNPC} (e.g. Amerhein and Suarez, 1988; Blum and Lasaga, 1991). The value of pH_{imm} is likely to not be influenced greatly by the presence of calcite as very little calcite dissolution occurred during the immersion period due to the high fluid pH. As discussed in section 4.5.2, a pH_{imm} of 9.66 for biotite can be attributed to the partial charge conservation of K release during the immersion period.

Table 4.1

pH of various zero points of charge determined in this study unless otherwise stated.

Mineral	pH_{imm}	pH_{IEP}	pH_{zpc}
α-SiO_2	-	1.3[a], 2.0[b]	2.91[c], 2.3 - 3.8[d]
MgO	-	12.4[e]	12.24[c]
α-Fe_2O_3	-	5.4 - 6.9[e]	6[d]
$^{IV}Al_2O_3$	-	6.8[f]	8.5 - 9[d]
Muscovite	-	0.95[a]	6.6[c]
Phlogopite	-	-	8[c]
Biotite	-	0.41[a], 2.6[g]	6.5[h], 6 - 7[i]
Grasåsen Biotite	9.66	3.02	4.12[j], 7.50[k]

[a] Cases (1967)

[b] James and Healy (1972)

[c] Sverjensky (1994)

[d] Kosmulski (2009)

[e] Parks (1965)

[f] Parks (1967)

[g] Rath and Subramanian (1997)

[h] Alonso (2003, as cited by Filby et al., 2008)

[i] Alonso et al. (2009)

[j] Calculated from component single oxide pH_{IEP} values using Eq. 4.22 (c.f. Jara et al., 2005)

[k] pH_{ZNPC} Calculated correcting for H^+ consumed during immersion by dissolution and hydrolysis reactions, non stoichiometric K release, and carbonate equilibria.

By subtracting the net number of protons consumed by this exchange reaction, the dissolution of both biotite and calcite and metal hydrolysis from $[H^+]_{t=0}$ we have calculated a pH_{ZNPC} for biotite of 7.50, comparable to reported pH_{ZPC} values for biotite 6.5 (Alonso, 2003 (as cited in Filby et al., 2008)) and 6–7 (Alonso et al., 2009), muscovite 6.6, and phlogopite 8 (Sverjensky, 1994), as summarised in Table 4.1.

However comparable our values for the various points of zero charge of biotite are to literature data, it is clear that the sole use of the ZPC, IEP, ZNPC or immersion pH to infer the surface charge of biotite at a given pH could provide an ambiguous picture of biotite surface chemistry. As previously proposed in Oelkers et al. (2009), accurate

modelling the surfaces of complex multi-oxide silicates, e.g. phyllosilicates, requires the consideration of a changing surface composition as a function of the surrounding fluid chemistry.

4. 5. 4. Implications of biotite surface chemistry for dissolution kinetics as a function of aqueous solution composition

The dissolution mechanism of minerals has often been related to the chemical composition of the surface and the reactions occurring at the mineral-fluid interface (e.g. Furrer and Stumm, 1986; Brady and Walther, 1990). For the case of biotite, dissolution rates as a function of pH are similar to that of other aluminosilicates, in that they decrease with increasing pH in acidic conditions (i.e. up to pH 7) and increase thereafter with increasing pH (Lin and Clemency, 1981a; Lin and Clemency, 1981b; Acker and Bricker, 1992; Turpault and Trotignon, 1994; Kalinowski and Schweda, 1996; Malmström et al., 1996; Malmström and Banwart, 1997; Brandt et al., 2003; Balogh-Brunstad et al., 2008; Balland et al., 2010; Haward et al. 2011; Cappelli et al., 2013; Voinot et al., 2013). As the pH of minimum biotite dissolution rate (~ pH 7) differs from both pH_{IEP} (3.02) and pH_{imm} (9.66), it is clear that the biotite dissolution rates are not directly related to proton consumption at the surface. In contrast, the biotite surface reactivity appears to be dominated by non charge-conservative metal release, shown above to alter the surface composition of biotite as a function of pH. Such metal release involves the breaking of metal-oxygen bonds, both at the biotite surface and at a varying depth within the mineral, with a shift towards a relatively negatively charged biotite near-surface. The breaking of such bonds and the charge imbalance would weaken the biotite structure near the fluid interface, facilitating the mineral's eventual dissolution. As such, it seems likely that such metal release reactions are critical in controlling, biotite dissolution rates, consistent with the dissolution pathways of a wide variety of other

multi-oxide silicates (e.g. Oelkers et al., 1994; Gautier et al., 1994; Devidal et al., 1997; Gislason and Oelkers, 2003; Wolff-Boenisch et al., 2004; Carroll and Knauss, 2005; Saldi et al., 2007).

4. 5. 5. Implications for nutrient availability and bio-acquisition.

As described above, a K depleted zone exists at all pH, extending to a bulk average depth of 2.5 nm, though this occurs primarily at the edges of the mineral grains (Fig S-2). Indeed, the depletion depth of K at the edges of biotite grain varies from 25 up to 40 nm from a pH 0.5 to 11.5 while the K depletion on the basal planes barely exceed 0.5 nm maximum at pH 0.5. This potassium depletion zone formed upon contact with water during the immersion period and this depth appears to be time independent for at least 60 minutes.

In a previous study (Bonneville et al., 2011), we have shown that biotite basal plane can also be depleted in K and other elements such Al, Fe and Mg due to mycorrhizal alteration. Upon direct contact with biotite surface, fungal hypha can mobilize K up to a depth of 20 nm for pH range of 4.6 to 5.8 in the hypha near-environment. For the same pH range, the present study in an abiotic, water-saturated system shows that the basal plane K mobilization is much more restricted, approximately 20 times less. This observation highlights the effectiveness of fungi to remove potassium from the biotite interlayer through a combination of the mechanical and chemical alteration pathways of the biotite in direct contact with hyphae. This alteration, or 'bio-fracking', comes in 4 forms: (i) forcing the crystallographic lattice of phyllosilicates (Bonneville et al., 2009), (ii) the creation of channels at the basal surface (Gazzè et al., 2012), (iii) the secretion of a biolayer up to 35nm in thickness (Saccone et al., 2012) and, (iv) acidification of the hyphae near-environment at the biotite surface (Bonneville et al., 2011).

4. 6. CONCLUSION

A combined approach of electrokinetic measurements, potentiometric batch titrations, and aqueous solution chemistry analyses have provided insight into the interaction of protons with the biotite surface. In brief, our results demonstrate the complex and variable nature of the biotite surface as a function aqueous fluid composition. Indeed, the ZPC, IEP, and immersion pH have vastly different values for biotite and therefore the sole use of zero points of charge provide an inaccurate depiction of biotite surface chemistry. Our study emphasizes the need to consider the variable composition of the multi-oxide surface as a function of pH to accurately model the surface chemistry of those minerals and understand their chemical reactivity. The processes occurring at the biotite near-surface observed in this study help us to understand and interpret weathering reactions in microbially dominated natural systems. The results of this study will be also be used further to aid the interpretation of biotite dissolution kinetics in chapter 5.

Chapter 5. Biotite weathering rates

The effect of pH, grain size and organic ligands on biotite weathering rates

This chapter is a reproduction of a manuscript submitted for review in *Geochimica et Cosmochimica Acta*: Bray A. W., Oelkers E. H., Bonneville S., Wolff-Boenisch D., Potts N. J., Fones G., Benning L. G. It addresses the second research objective outlined in the introduction, to determine the release rate of elements from biotite as a function of pH, grain size and organic ligand presence. Biotite edge surfaces are up to 120 times more reactive than basal surfaces. Biotite dissolved non stoichiometrically, and the order of element release is pH dependent. This study aids our understanding of fluid-mineral interactions, and the possible role of organic ligands in bio weathering.

Abstract

The dissolution kinetics of two distinct biotite samples were determined at 25 °C, from pH 2 to 6, and as a function of grain size and aqueous organic ligand concentration. Dissolution rates were measured using both open- and closed-system reactors in fluids having a constant ionic strength. Element release was non-stoichiometric and followed the general trend of Fe, Mg> Al>Si. At near-neutral pH in the closed-system experiments, the release of Al was stoichiometric and Fe was preferentially retained in the solid phase likely due to secondary mineral precipitation. Biotite dissolution rates in the acidic range, generated from Si release rates, are consistent with the empirical rate law:

$$r_i = k_{\mathrm{H},i} a_{H+}^{xi}$$

where $k_{\mathrm{H},i}$ refers to the apparent rate constant, a_{H^+} designates the activity of protons, and x_i stands for a reaction order with respect to protons. Rate constants range from 30.6 x 10^{-10} to 2.15 x 10^{-10} ($moles_{biotite}$ m^{-2} s^{-1}) with reaction orders ranging from 0.31 to 0.58.

Biotite dissolution is highly spatially anisotropic with edges 120 times more reactive than basal planes. Aqueous organic ligands slightly enhance biotite dissolution in the lightly acidic and near neutral pH range. Results are applied to the greater understanding of the mineral-fluid-organism chemical interactions which occur in the natural environment, and how organic exudates mobilise nutrients for organisms.

5. 1. INTRODUCTION

The weathering of silicate minerals controls the chemical composition of natural waters, supplies nutrients to the biosphere and is an important regulating process for the global carbon cycle at geological time-scales (Berner and Berner, 1996). Among silicates, phyllosilicate weathering has a particularly strong influence on geochemical cycles due to their abundance, large specific surface area, and high ion-exchange capacity (Sposito, 1984; Davis and Kent, 1990; Drever, 1997; Bowser and Jones, 2002). Among phyllosilicates, biotite is the key source of primary (K) and secondary (Fe, Mg, Al) nutrients in soils, and is estimated to make up ~7% of the exposed crustal surface (Nesbitt and Young, 1984). Indeed, during the past few decades many field and laboratory studies have shown that the biosphere is crucial in controlling mineral weathering and therefore influencing geochemical processes (Beerling and Berner, 2005; Taylor et al., 2009).

A number of experimental studies have quantified the abiotic dissolution of biotite have revealed that, at a given pH, the reported rates vary up to 1.5 orders of magnitude (Acker and Bricker, 1992; Turpault and Trotignon, 1994; Kalinowski and Schweda, 1996; Malmström et al., 1996; Malmström and Banwart, 1997; He et al., 2005). These variations can be due to a number of possible reasons; (a) differences in bulk chemical composition of the biotite, (b) differences in grain size and geometry of particles dissolved, (c) different experimental approaches and durations used for determining

dissolution kinetics, and (d) variations in chemical compositions and concentrations of the reacting fluids (Oelkers et al., 2001; Brantley, 2003; Köhler et al., 2005; Zhang and Lüttge, 2009; Arvidson and Lüttge, 2010; Rimstidt, 2014; Fischer et al., 2014).

Biotite is a subgroup of the mica group which forms a solid solution series with iron and magnesium end members annite ($K\,Fe_3\,AlSi_3O_{10}\,(OH)_2$) and phlogopite ($K\,Mg_3\,AlSi_3O_{10}\,(OH)_2$). The variable concentrations of Fe and Mg in natural biotite samples, in conjunction with the substitution of a wide variety of other elements in the octahedral and tetrahedral silicate sheets, leads to differences in element release rates when normalised to the biotite formula. To test the effect of mineral composition on dissolution rates, we present data from the dissolution of two distinct biotite samples.

Existing biotite dissolution kinetic studies have employed a variety of experimental approaches. These include (a) open-system experiments performed in fluidized-bed reactors and flow-through columns (Acker and Bricker, 1992), dialysis-cell reactors (Kalinowski and Schweda, 1996), thin-film flow-through reactors (Malmström et al, 1996; Malmström and Banwart, 1997), and continuous-flow reactors (Hodson, 2006; Voinot et al, 2013), and (b) closed-system experiments where biotite was reacted in batch mode with a variety of solutions (Turpault and Trotignon, 1994; Balland et al., 2010). It is important to note that all open-system experiments were performed for days to months, allowing the determination of steady-state far from equilibrium dissolution rates. However, significant changes in both surface area and bulk mineral composition can occur during such open-system experiments, requiring the careful consideration of surface area normalisation (Brantley, 2003; Hodson, 2006). Often, rate data from open-system experiments are normalised to an initial surface area and initial mineral composition, and changes in either of these parameters in not considered. Conversely, closed-system experiments are usually performed over shorter timescales (hours to days) and allow the characterisation of the initial stages of dissolution. However, rates

determined from these short closed-system experiments can be significantly affected by the changing fluid composition, and rates can be obscured by secondary phase precipitation (Oelkers et al., 2001; Brantley, 2003). Currently, there are no experimental studies that compare directly open- and closed-system biotite dissolution rates; therefore we have addressed this by performing both mixed–flow (open-system) and batch (closed-system) experiments with the same biotite, at equivalent conditions.

Moreover, biotite is highly anisotropic, in terms of surface reactivity, with edge (*h k* 0) surfaces between 30 to 300 times more reactive than basal (0 0 1) surfaces (Turpault and Trontignon, 1994; Hodson, 2006). This implies that the grain shape and size will play a crucial role in measuring and interpreting dissolution rate data. Surprisingly however, the majority of published biotite dissolution rates are normalised to the total surface area, and the effect of geometric anisotropy on reactivity have not been addressed experimentally. Therefore, in this study, we have performed experiments with three different biotite size fractions, each with different geometric (edge to basal surface) ratios to better understand the control of grain size and geometry on biotite dissolution kinetics.

Finally, most past studies only focussed on the abiotic biotite dissolution However, in natural settings, biotite is a prime source of nutrients (K in particular) and thus biotic processes may play an important role in element release. Several recent studies have demonstrated that microorganisms influence phyllosilicate weathering through a combination of physical and chemical alteration, or 'bio-fracking' (Balogh-Brunstad et al., 2008; Hopf et al., 2009; Bonneville et al., 2009; Balland et al., 2010; Bonneville et al., 2011; Saccone et al., 2012; Gazzè et al., 2012; Gazzè et al., 2013). One bio-mediated mechanism is changing the chemical composition of the local environment, i.e. localised acidification (Balogh-Brunstad et al., 2008; Bonneville et al., 2011) Such acidification is the result of microbial/fungal respiration and the release of organic ligands in the near

environments of living microorganisms (Bonneville et al., 2011; Gazzè et al., 2013). With this in mind, several studies quantified the effect of organic ligands (low molecular weight organic acids and siderophores) on biotite dissolution (e.g. Drever and Stillings, 1997; Balland et al, 2010; Voinot et al., 2013). A catalysing effect of organic ligands on mineral weathering (i.e. a doubling of dissolution rate) has been reported in the presence of high concentrations of organic ligands (i.e., $>10^{-3}$ M, Golubev et al., 2006; Balland et al., 2010). However, the effect of organic ligands on mineral dissolution at the low concentration levels typically found in soils (10^{-5} to 10^{-6} M, Jones, 1998; Ullman and Welch, 2002), and known to be secreted by microorganisms ($< 10^{-3}$ M, Adeyemi and Gadd, 2005) is unclear, and for complex multi-oxide silicates, such as biotite, only a few data sets testing the effects of organic ligands on dissolution exist (Balland et al., 2010; Voinot et al., 2013). To test the effect organic ligands on biotite dissolution, we have reacted biotite with three organic ligands (citric acid, oxalic acid, and the siderophore desferrioxamine B, DFOB) and assessed their influence on element release and biotite dissolution rates. By doing this we are better able to link biotic and abiotic dissolution data to natural soil forming processes, where microbial/fungal exudates contribute significantly to mineral dissolution.

5. 2. MATERIALS AND METHODS

5. 2. 1. Mineral samples

The chemical composition of the Grasåsen and Moen biotite samples used in this study were previously described (Moen – Bonneville et al., 2009; Grasåsen – Bray et al., 2014) and the stoichiometric formula of each is given in Table 5.1. Each sample was crushed separately using a jaw crusher, pestle and mortar, ball mill, and agate disk mill, removing inclusions throughout. The crushed biotite samples were subsequently sieved to obtain the 75–150 μm (Moen), and 25-53, 53-180, and 180-500 μm (Grasåsen) size

Table 5.1

Chemical composition of the biotite samples (oxide wt. %) derived by EMPA.

	Moen [a]	Grasåsen [b]
SiO_2	35.12	37.52
TiO_2	3.32	3.24
Al_2O_3	16.23	14.75
Cr_2O_3	0.03	0.01
FeO	24.73	17.39
MnO	0.83	0.06
MgO	6.57	12.76
CaO	0.02	0.002
Na_2O	0.12	0.08
K_2O	9.23	9.48
H_2O	3.32	3.97
F	1.04	-
Cl	0.11	-
Σ	100.68	99.27

[a] Bonneville et al., 2009. Moen, Norway.

$(K_{0.918}Na_{0.018})(Mg_{0.763}Mn_{0.055}Fe^{(II)}_{1.612}Cr^{(II)}_{0.002})(Al_{1.491}Ti^{(IV)}_{0.195}Si^{(IV)}_{2.737})(OH)_2(O)_{10}F_{0.257}Cl_{0.015}$.

[b] Bray et al., 2014. Grasåsen, Norway.

$(K_{0.913}Na_{0.011}Ca_{0.0002})(Mg_{1.436}Mn_{0.004}Fe^{(II)}_{1.098}Cr^{(II)}_{0.0004})(Al_{1.312}Ti^{(IV)}_{0.184}Si^{(IV)}_{2.832})(OH)_2(O)_{10}$.

fractions. Each size fraction was then washed ultrasonically 10 times in 18.2 MΩ water, separated by gravitational settling, and dried at 40 °C for 48 hours.

Post washing, each size fraction was imaged using a field emission gun scanning electron microscope (FEG-SEM, FEI Quanta 650 equipped with an Oxford X-Max silicon drift detector, SDD, operated at 20 kV) on a stage set at a 45° angle to determine grain geometries, from which the geometric specific surface area (SSA_{geo}, m^{-2} g^{-1}), and the average edge (SA_{edge}, %) and basal plane (SA_{basal}, %) proportions of each size fraction were determined. The specific surface area (SSA_{BET}, m^{-2} g^{-1}) of each size fraction was measured via a 9 point N_2 adsorption isotherm between 0.05 and 0.25 p/p_o (equilibrium pressure/saturation pressure) at 77 K using a Micromeritics Gemini V analyser. Samples were degassed with N_2 for 20 hours before analysis and the surface area was calculated

using the BET method (Brunauer et al., 1938) based on an assumed cross section of adsorbed N_2 of 0.162 nm^2. Replicate measurements of 76 sub-samples of the 53–180 µm size fraction yielded a relative standard deviation (RSD) of 4.6%. The SSA_{BET}, SSA_{geo}, SA_{edge}, and SE_{basal} of each size fraction are given in Table 5.2. Images of the post washing, pre reaction biotite grains are shown in figure B–1 in Appendix B.

5. 2. 2. Dissolution experiments

5. 2. 2. 1. Closed-system experiments

In total, 91 closed-system experiments were conducted on the prepared biotite fractions in high density polyethylene bottles (HDPE, Nalgene) at 25 ± 1 °C for up to 12 hours. The bottles were constantly shaken in an incubator at 140 rpm. In addition, each bottle was shaken manually a minimum once every hour for the duration of the 12 hour experiments. For each experiment, 1–2 g of biotite was added to 1 L of reactive fluid. Two types of reactive fluid were prepared: (i) one set of experiments (Moen biotite) was performed in aqueous 0.01M $CaCl_2$ (AnalaR NORMAPUR, VWR) with the pH adjusted to between 2 and 6 using HCl/NaOH (Aristar/AnalaR NORMAPUR, VWR). A second larger

Table 5.2

Surface area parameters for the four biotite powder size fractions.

	Grasåsen biotite 25-53 µm	Grasåsen biotite 53-180 µm	Grasåsen biotite 180-500 µm	Moen biotite 75-150 µm
SSA_{BET} (m^2 g^{-1})	3.25 [a] ± 0.05	0.92 [b] ± 0.09	0.64 [c] ± 0.07	2.63 [d] ± 0.08
SSA_{geo} (m^2 g^{-1})	0.40	0.19	0.18	0.24
SA_{edge}	11.6 % [e] ± 12.4 %	7.0 % [f] ± 10.6 %	2.2 % [g] ± 2.3 %	4.1 % [h] ± 5.9 %
SA_{basal}	88.4 % [e] ± 12.4 %	93.0 % [f] ± 10.6 %	97.8 % [g] ± 2.3 %	95.9 % [h] ± 5.9 %
Roughness factor (SSA_{BET}/SSA_{geo})	8.12	4.86	3.53	11.16

[a] n = 3, [b] n = 76, [c] n = 3, [d] n = 1, [e] n = 50, [f] n = 50, [g] n = 25, [h] n = 18.

set of experiments was performed with fluids that were buffered at each pH (also 2–6) with potassium hydrogen phthalate (KHP, $C_8H_5KO_4$, CertiFied AR, Fisher). KHP was used as a background electrolyte to fix the ionic strength and to buffer the pH because initial experiments with $CaCl_2$ showed a strong pH buffering ability of the Grasåsen biotite. Experiments were also conducted using both types of reactive fluids to which 500 µmoles L^{-1} of either citric acid ($C_6H_8O_7$), DFOB ($C_{25}H_{48}N_6O_8$), or oxalic acid ($C_2H_2O_4$) were added. Details for all experimental conditions are given in Table 5.3. The maximum pH variance in each experiment was ± 0.08 pH units (based on average of 2σ of pH for each experiment, 95% confidence).

Table 5.3

Details of the closed-system experiments, element release fitting parameters and analytical release rates

			Size fraction		Surface Area	Fitting parameters								Biotite dissolution rate							
						Al		Fe		Mg		Si		$\log R_{Al}$	$\log R_{Fe}$	$\log R_{Mg}$	$\log R_{Si}$	$\log R_{Al}$	$\log R_{Fe}$	$\log R_{Mg}$	$\log R_{Si}$
	Exp.	matrix	µm	pH	$m^2 L^{-1}$	$k' 10^{-7}$	q	$k' 10^{-7}$	q	$k' 10^{-7}$	q	$k' 10^{-7}$	q	t = 1 s	t = 1 s	t = 1 s	t = 1 s	t = 12 h	t = 12 h	t = 12 h	t = 12 h
Grasåsen	18-20	KHP	53-180	2.56	1.95	7.19	0.25	6.25	0.28	6.56	0.26	3.08	0.25	-6.74	-6.76	-6.77	-7.12	-10.21	-10.11	-11.62	-10.61
	21-23			3.21	2.00	7.51	0.20	5.93	0.24	7.05	0.22	3.22	0.20	-6.81	-6.84	-6.81	-7.19	-10.50	-10.35	-11.92	-10.89
	24-26			4.16	1.98	2.91	0.25	1.41	0.33	2.25	0.30	2.60	0.19	-7.13	-7.33	-7.17	-7.30	-10.60	-10.44	-11.27	-11.03
	33-35		25-53	4.47	6.73	11.00	0.15	9.72	0.13	12.94	0.16	4.67	0.17	-6.78	-6.88	-6.68	-7.11	-10.73	-10.90	-12.48	-10.98
	36-38		180-500	4.10	1.32	1.70	0.30	0.29	0.48	3.35	0.25	1.24	0.23	-7.29	-7.86	-7.08	-7.55	-10.54	-10.28	-11.71	-11.13
	27-29		53-180	5.18	2.02	0.80	0.33	0.30	0.41	1.15	0.34	1.43	0.22	-7.58	-7.91	-7.40	-7.51	-10.66	-10.66	-10.97	-11.15
	30-32			5.95	1.89	1.81	0.11	0.17	0.28	2.02	0.23	1.61	0.12	-7.69	-8.31	-7.34	-7.71	-11.81	-11.66	-11.86	-11.78
	39-41			2.60	1.97	7.02	0.25	8.23	0.25	5.53	0.27	3.93	0.21	-6.75	-6.68	-6.83	-7.07	-10.22	-10.14	-11.52	-10.71
	42-44	KHP + Citric acid	53-180	3.07	1.85	4.96	0.26	3.26	0.31	3.85	0.29	3.27	0.22	-6.88	-6.99	-6.95	-7.15	-10.30	-10.17	-11.37	-10.79
												1.38	0.24				-7.48				-11.01
	45-47			3.95	1.96	6.26	0.21	4.36	0.26	4.89	0.24	3.24	0.21	-6.89	-6.94	-6.93	-7.17	-10.57	-10.36	-11.75	-10.85
	48-50			4.96	1.85	1.93	0.29	0.89	0.39	1.87	0.32	1.16	0.27	-7.25	-7.46	-7.22	-7.50	-10.55	-10.29	-11.15	-10.88
	51-53			5.70	1.87	0.54	0.38	0.14	0.53	0.79	0.38	0.11	0.47	-7.69	-8.12	-7.53	-8.30	-10.58	-10.31	-10.74	-10.76
	54-56	KHP + DFOB	53-180	2.52	1.73	8.34	0.26	10.79	0.24	7.66	0.25	4.26	0.21	-6.67	-6.58	-6.72	-7.05	-10.12	-10.10	-11.71	-10.73
	72-74			3.16	1.79	1.65	0.38	1.68	0.40	1.65	0.38	0.70	0.35	-7.21	-7.17	-7.21	-7.61	-10.09	-9.95	-10.74	-10.65
	75-76			4.18	1.81	1.58	0.32	1.57	0.35	1.45	0.33	0.59	0.29	-7.30	-7.26	-7.32	-7.76	-10.46	-10.27	-11.04	-11.04
	78-80			5.21	1.85	0.54	0.41	0.47	0.46	1.02	0.36	0.08	0.48	-7.66	-7.67	-7.43	-8.42	-10.41	-10.20	-10.83	-10.82
	81-83			5.98	1.85	0.30	0.43	0.18	0.52	0.81	0.36	0.16	0.40	-7.89	-8.04	-7.53	-8.19	-10.54	-10.26	-10.85	-10.97
	57-59	KHP + Oxalic acid	53-180	2.50	1.90	11.08	0.23	12.07	0.23	7.89	0.24	3.14	0.24	-6.59	-6.56	-6.71	-7.13	-10.16	-10.12	-11.72	-10.66
	60-62			3.06	1.80	10.19	0.22	10.74	0.23	7.49	0.23	4.13	0.19	-6.65	-6.61	-6.75	-7.10	-10.27	-10.18	-11.80	-10.86
	63-65			3.94	1.88	10.71	0.17	7.07	0.23	5.94	0.22	1.11	0.25	-6.73	-6.79	-6.88	-7.55	-10.57	-10.36	-11.92	-11.01
	66-68			4.99	1.80	2.97	0.25	1.42	0.34	1.83	0.31	0.87	0.28	-7.13	-7.32	-7.24	-7.62	-10.61	-10.39	-11.20	-10.97
	69-71			5.74	1.87	0.26	0.43	0.51	0.37	0.21	0.48	0.51	0.27	-7.95	-7.72	-8.00	-7.87	-10.59	-10.65	-10.02	-11.27

Table 5.3 continued.

			Size fraction		Surface Area	Fitting parameters								Biotite dissolution rate							
						Al		Fe		Mg		Si		log R_{Al}	log R_{Fe}	log R_{Mg}	log R_{Si}	log R_{Al}	log R_{Fe}	log R_{Mg}	log R_{Si}
	Exp.	matrix	µm	pH	$m^2 L^{-1}$	$k' 10^{-7}$	q	$k' 10^{-7}$	q	$k' 10^{-7}$	q	$k' 10^{-7}$	q	t = 1 s	t = 1 s	t = 1 s	t = 1 s	t = 12 h	t = 12 h	t = 12 h	t = 12 h
Grasåsen	84	KHP + [Si]	53-180	4.27	1.90	2.49	0.26	1.91	0.29	2.28	0.30	0.76	0.28	-7.18	-7.26	-7.17	-7.67	-10.59	-10.57	-11.31	-11.00
	85			4.27	1.74	3.25	0.24	2.23	0.28	3.72	0.25	0.92	0.27	-7.11	-7.21	-7.03	-7.61	-10.62	-10.56	-11.68	-11.02
	87			4.14	1.79	4.10	0.25	2.79	0.30	3.40	0.28	5.30	0.16	-6.98	-7.08	-7.03	-7.08	-10.45	-10.32	-11.47	-10.99
	89			4.12	1.78	5.68	0.23	4.60	0.27	3.89	0.27	1.78	0.25	-6.88	-6.91	-6.98	-7.35	-10.44	-10.31	-11.50	-10.81
	90			4.16	1.66	1.70	0.26	1.06	0.34	1.64	0.29	1.27	0.20	-7.35	-7.44	-7.32	-7.58	-10.76	-10.50	-11.35	-11.27
	92			4.22	1.84	0.40	0.33	0.09	0.46	0.52	0.37	0.27	0.28	-7.88	-8.38	-7.72	-8.11	-11.00	-10.88	-10.80	-11.44
	94			3.99	1.92	0.76	0.35	0.21	0.48	0.94	0.33	0.16	0.41	-7.57	-7.99	-7.50	-8.18	-10.58	-10.38	-11.03	-10.92
	96			3.97	1.79	0.49	0.41	0.47	0.40	0.55	0.39	0.02	0.58	-7.70	-7.72	-7.67	-8.86	-10.45	-10.50	-10.63	-10.81
	98			4.24	1.80	0.17	0.53	0.09	0.62	0.25	0.50	0.07	0.43	-8.05	-8.26	-7.91	-8.53	-10.25	-10.03	-9.93	-11.17
	86	KHP + [Al]	53-180	4.04	1.75	4.73	0.25	2.69	0.32	3.66	0.28	1.53	0.25	-6.92	-7.07	-6.99	-7.41	-10.40	-10.24	-11.45	-10.87
	88			4.01	1.77	9.20	0.19	6.42	0.24	5.66	0.24	3.15	0.19	-6.75	-6.82	-6.87	-7.22	-10.49	-10.37	-11.76	-10.98
	91			4.06	1.91	4.52	0.18	0.55	0.40	0.93	0.34	0.52	0.28	-7.09	-7.66	-7.50	-7.84	-10.88	-10.46	-10.98	-11.18
	93			4.00	1.82	0.11	0.49	0.16	0.43	0.47	0.38	0.05	0.46	-8.27	-8.16	-7.74	-8.61	-10.62	-10.80	-10.68	-11.10
	95			3.83	1.72	1.03	0.35	0.42	0.44	1.48	0.32	0.84	0.20	-7.45	-7.74	-7.33	-7.77	-10.48	-10.32	-11.17	-11.48
	97			3.81	1.76	2.38	0.30	2.45	0.31	1.73	0.33	5.91	0.0021	-7.14	-7.12	-7.24	-8.90	-10.38	-10.34	-11.08	-13.53
	99			4.02	1.89	0.61	0.39	0.26	0.51	0.34	0.46	1.29	0.0042	-7.62	-7.88	-7.80	-9.27	-10.46	-10.16	-10.15	-13.88
Moen	1	$CaCl_2$	75-150	2.00	2.47	10.74	0.23	19.75	0.16	25.62	0.22	-	-	-6.60	-6.50	-6.25	-	-10.16	-10.40	-9.86	-
	2			4.00	2.44	6.63	0.1301	11.82	0.093	17.64	0.1183	-	-	-7.06	-6.96	-6.68	-	-11.10	-11.16	-10.77	-
	3			6.00	2.42	-	-	-	-	17.09	0.0698	-	-	-	-	-6.92	-	-	-	-11.24	-
	4	$CaCl_2$ + Citric acid	75-150	2.00	2.44	26.02	0.11	6.69	0.23	14.96	0.22	-	-	-6.55	-6.81	-6.48	-	-10.68	-10.38	-10.08	-
	5			4.00	2.45	5.76	0.1745	9.59	0.157	17.00	0.1455	-	-	-7.00	-6.82	-6.61	-	-10.82	-10.73	-10.57	-
	6			6.00	2.44	2.51	0.1581	13.56	0.0622	12.29	0.1221	-	-	-7.40	-7.07	-6.82	-	-11.30	-11.42	-10.89	-
	7	$CaCl_2$ + DFOB	75-150	2.00	2.48	2.19	0.38	4.32	0.3091	8.51	0.31	-	-	-7.08	-6.87	-6.58	-	-9.95	-10.08	-9.77	-
	8			4.00	2.42	6.95	0.1961	10.86	0.1722	52.78	0.1094	-	-	-6.87	-6.73	-6.24	-	-10.59	-10.57	-10.37	-
	9			6.00	2.25	0.21	0.3817	9.28	0.1183	4.28	0.2076	-	-	-8.10	-6.96	-7.05	-	-10.97	-11.05	-10.72	-

Over the course of each 12 hour closed-system experiment, up to 20 samples containing 5 mL of a mixture of reactive fluid and biotite particles were removed with a 5 mL syringe with decreasing frequency as each experiment progressed. Removed samples were immediately filtered through 0.2 μm polyethersulfone filters (Sartorius) and quenched in 3% HNO_3 (Aristar, VWR), HCl (Aristar, VWR) or NaOH (AnalaR NORMAPUR, VWR) depending on analysis. Experiments were halted after 12 hours and the remaining reactive fluid was separated from the reacted biotite by centrifugation. All fluids were analysed as described below, and the reacted biotite powder was recovered for subsequent imaging and analysis. Fluid samples were analysed for Al, Fe, Mg, and Si by inductively coupled plasma mass spectrometry (ICP-MS, Agilent 7500ce with integrated auto-sampler, analytical error 6.3%), and to cross check, Mg was also analysed by atomic absorption spectroscopy (AAS, Analytik Jena Contraa 700, maximum analytical uncertainty of 2.8%). A double beam spectrophotometer (Uvikon XL) was used to analyse aqueous silica (molybdate blue method at 815 nm; Coradin et al., 2004; Eaton et al., 2005, analytical uncertainty 3.5%) and iron (ferrozine method at 562 nm; Viollier *et al.*, 2000, analytical uncertainty 4.4%). The limit of quantification for Al, Fe, Mg, and Si, determined from calibration curves, was 0.8, 0.6, 5.3, and 4.7 μg kg^{-1} respectively. The average analytical uncertainty, measured against two certified reference materials for Al, Fe and Mg (SLRS-5 CRM, National Research Council Canada; NWTM-27.3, LGC Standards), and an in-house standard for Si, was determined to be 5.7, 6.7, 1.1, and 7.9% respectively. The limit of quantification for Mg by AAS was 2.6 μg kg^{-1} with a maximum analytical uncertainty of 7.8%. The limit of quatification for Fe and Si by spectrophotometry was 2.6 and 12.1 μmoles kg^{-1} respectively.The maximum analytical uncertainty for analyses, determined by inhouse standards was 4.4% and 3.5 % for Fe and Si respectively.

5. 2. 2. 2. Open-system experiments

Both the Moen and Grasåsen biotite samples were reacted with fluids of pH 2 to 4 at constant ionic strengths. These open-system experiments were performed in two distinct mixed-flow reactors, the experimental details are outlined in Table 5.4:

The Moen biotite was reacted with an aqueous $CaCl_2$ solution of 0.01 M ionic strength at pH 3.3 in a 300 mL titanium Parr™ mixed-flow reactor with continuous pH monitoring and controlled temperature, pressure, and stirring, as described by Wolff-Boenisch et al. (2004). Briefly, 3 to 6 g of the 75-150 µm biotite size fraction and 300 ml of the reactive fluid was added to the reactor, stirred at 400 rpm. The biotite was allowed to react for up to 260 hours with the reactive fluid continuously pumped through the reactor with a high pressure liquid chromatography pump (HPLC) at flow rates from 1.2 to 2.2 g/min. At the system outlet, the fluid passed through a 2 µm titanium filter and was further filtered using 0.2 µm polyvinylidene fluoride (PDVF) Whatman™ filters before being collected in acid washed HDPE sample bottles. Fluid samples were acidified with HNO_3 (Aristar, VWR); solid samples were recovered after the experiments by centrifugation and were subsequently dried.

Table 5.4

Details of the open-system experiments and calculated dissolution rates.

Exp.		Matrix	additive		pH	*m*	Flow	[Al]	[Fe]	[Mg]	[Si]	log R_{Al}	log R_{Fe}	log R_{Mg}	log R_{Si}
				mol L^{-1}		g	mL min^{-1}	mol L^{-1} 10^{-5}				mol m^{-2} s^{-1}			
1		HCl	-	-	1.99	1.03	0.18	13.03	10.96	13.31	17.81	-9.50	-9.49	-9.53	-9.69
2		HCl	Oxalic acid	0.0005	2.01	1.08	0.21	14.37	11.77	15.12	20.52	-9.41	-9.42	-9.45	-9.62
3		HCl	Citric acid	0.0005	1.97	1.01	0.21	9.56	7.08	8.85	12.49	-9.60	-9.65	-9.67	-9.83
7		NaCl	Oxalic acid	0.0005	3.33	1.05	0.21	1.03	1.79	2.04	3.26	-10.55	-10.24	-10.30	-10.39
10		NaCl	-	-	3.09	1.04	0.17	1.46	2.33	2.44	2.84	-10.48	-10.20	-10.30	-10.53
13		NaCl	-	-	4.39	1.07	0.17	-	-	-	0.53	-	-	-	-11.28
14		NaCl	Citric acid	0.0005	3.13	1.03	0.18	9.28	5.73	7.30	8.12	-9.64	-9.78	-9.79	-10.04
15		NaCl	-	-	3.11	1.11	0.19	2.48	3.09	3.64	5.03	-10.22	-10.05	-10.10	-10.25
16		NaCl	-	-	3.09	1.11	0.21	1.67	2.97	3.40	4.59	-10.38	-10.06	-10.11	-10.28
17A		KHP	-	-	4.14	1.49	0.12	0.30	0.55	0.47	0.48	-11.50	-11.15	-11.34	-11.62
17B		KHP	Citric acid	0.0005	3.93	1.49	0.12	0.53	0.73	0.71	0.74	-11.26	-11.04	-11.17	-11.45
18A		KHP	-	-	4.14	1.54	0.11	0.35	0.60	0.53	0.59	-11.48	-11.17	-11.34	-11.59
18B		KHP	Oxalic acid	0.0005	3.90	1.54	0.10	1.06	1.07	1.17	1.12	-11.01	-10.93	-11.01	-11.32
B2		$CaCl_2$	-	-	3.35	6.04	1.16	1.12	0.15	1.08	2.30	-11.04	-11.95	-10.77	-11.00
BC1		$CaCl_2$	Citric acid	0.0005	3.29	6.04	1.89	3.37	0.44	3.10	3.61	-10.59	-11.27	-10.10	-10.35
BCD1		$CaCl_2$	Citric Acid DFOB	0.0005 0.00028	3.00	6.04	1.87	5.08	0.19	5.49	4.15	-10.53	-11.64	-9.85	-10.18

The Grasåsen biotite was reacted in fluids of pH 2 to 4 at an ionic strength of 0.01 M, fixed using either NaCl or KHP. Experiments were conducted in 35 mL Teflon mixed flow reactors and were continuously stirred with floating Teflon magnetic stirring bars. The reactors consisted of identical base and head compartments holding the reactor chamber together by threaded connection (Köhler et al, 2005; Chaïrat et al., 2007; Flaathen et al., 2010; Declerq et al., 2013). Material was kept in the reactor chamber by placing 0.45 µm GN-6 Metricel MCE membrane filters at the connection of the reactor chamber with the base and head compartments. The reactors were submersed in a water bath at a constant temperature of 25 ± 1 °C and fluids were added to the reactors by peristaltic pump at rates from 0.1 to 0.6 g/min. The pH of the inlet and outlet fluids was measured using a Metrohm 713 pH Meter, calibrated with certified reference buffer solutions of pH 4.005, 6.866, and 9.183 (CertiPUR, Merck) at 25 °C. pH measurement precision was 0.02 pH units. Dissolved silica concentrations in these open system experiments were determined using the colorimetric molybdate blue method (Bran & Luebbe AutoAnalyzer 3, maximum analytical uncertainty ± 3.5%). Concentrations of Fe, Mg, and Al were determined by atomic absorption spectrophotometry using a Perkin Elmer 5100 PC spectrometer with maximum analytical uncertainty of 2.8%. The details of the open-system experiments are listed in Table 5.4.

5. 3. RESULTS

5. 3. 1. Closed-system experiments

To assess the stoichiometry of element release during the experiments, the number of moles of each element, $\boldsymbol{i}$, in the fluid phase at time t ($\boldsymbol{m}_{i,t}$) normalized to the mineral surface area present in the reactor, and the stoichiometry of the dissolving biotite ($\boldsymbol{m}'_{i,t}$) were calculated with

$$\boldsymbol{m'_{i,t}} = \frac{\boldsymbol{m_{i,t}}}{\boldsymbol{s} \cdot M \cdot \boldsymbol{n_i}} = \frac{\boldsymbol{c_{i,t}} \cdot \boldsymbol{V_t}}{\boldsymbol{s} \cdot M \cdot \boldsymbol{n_i}}$$

Eq. 5.1

where $\boldsymbol{c}_{i,t}$ (moles kg^{-1})is the measured fluid concentration of $\boldsymbol{i}$ at time t, V_t refers to the mass (kg) of reactive fluid in the reactor at time t, the symbol $\boldsymbol{s}$ represents the specific surface area of biotite powder (m^2 g^{-1}, either SSA_{BET} or SSA_{geo}), M the mass of biotite powder (g), and n_i the stoichiometry of the *ith* element in the biotite formula. Resulting values of $\boldsymbol{m'_{i,t}}$ are shown in Figures 5.1-5.3. The release of elements from biotite during the closed-system dissolution experiments is highly pH dependent and, in part, non-stoichiometric. In ligand free experiments at pH 2.5, the release of Mg, Fe, and Al is

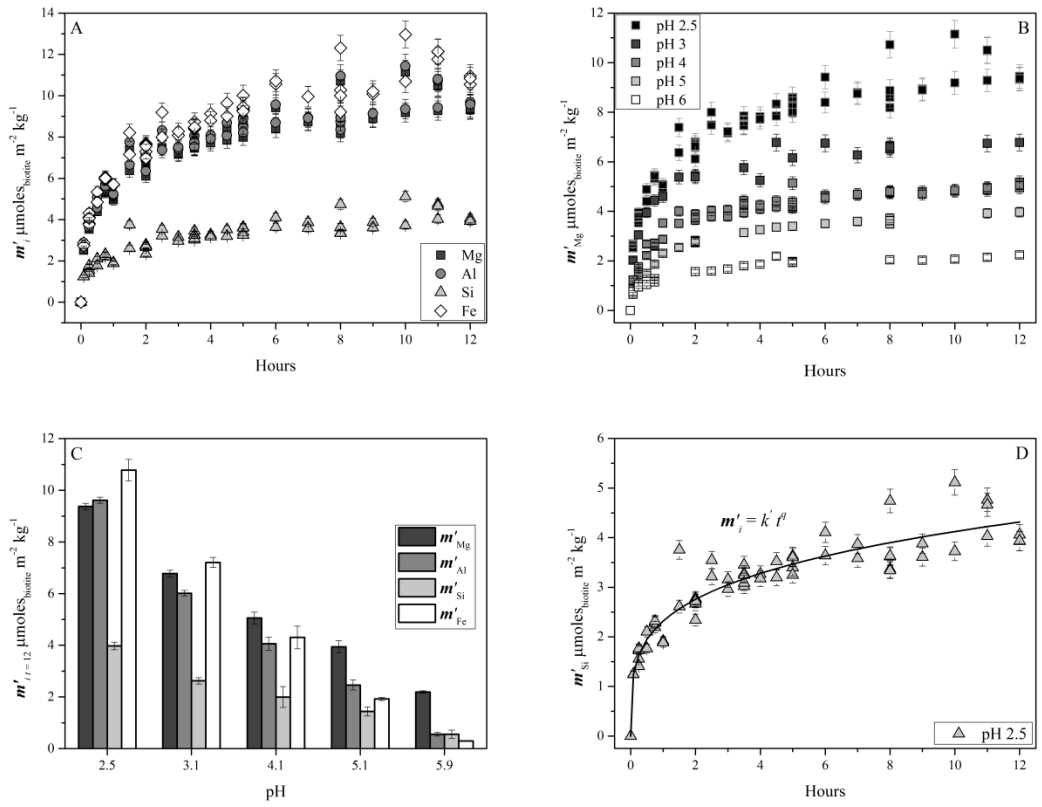

Figure 5.1

Element release data from the closed system abiotic dissolution reactions. (A) shows the release of elements at pH 2.5, (B) shows the release of Mg at each pH, (C) shows the concentration of each element after 12 hours, and (D) demonstrates the fit of element release data using Eq.5.1 on Si release data at pH 2.5.

largely stoichiometric with respect to one another, while Si release is 2.5-3 times lower when normalized to the dissolving biotite stoichiometry than that of these metals (Fig. 5.1A). With increasing pH the release of all elements decreases (Fig. 5.1B) with the final concentrations (after 12 hours) at pH 6 being ~1 order of magnitude lower than those at pH 2.5 (Fig. 5.1C). Increased pH also results in further non-stoichiometric release with a preferential Mg release over other elements at pH > 4 (Fig. 5.1C). Figure 5.1D shows the release of Si into the fluid at pH 2.5 and the general equation describing element release (Eq. 5.2), which is discussed further below.

At the same pH, surface area normalised element release increases with decreasing particle size fraction (Fig. 5.2). After 12 hours, the smallest biotite size fraction (25–

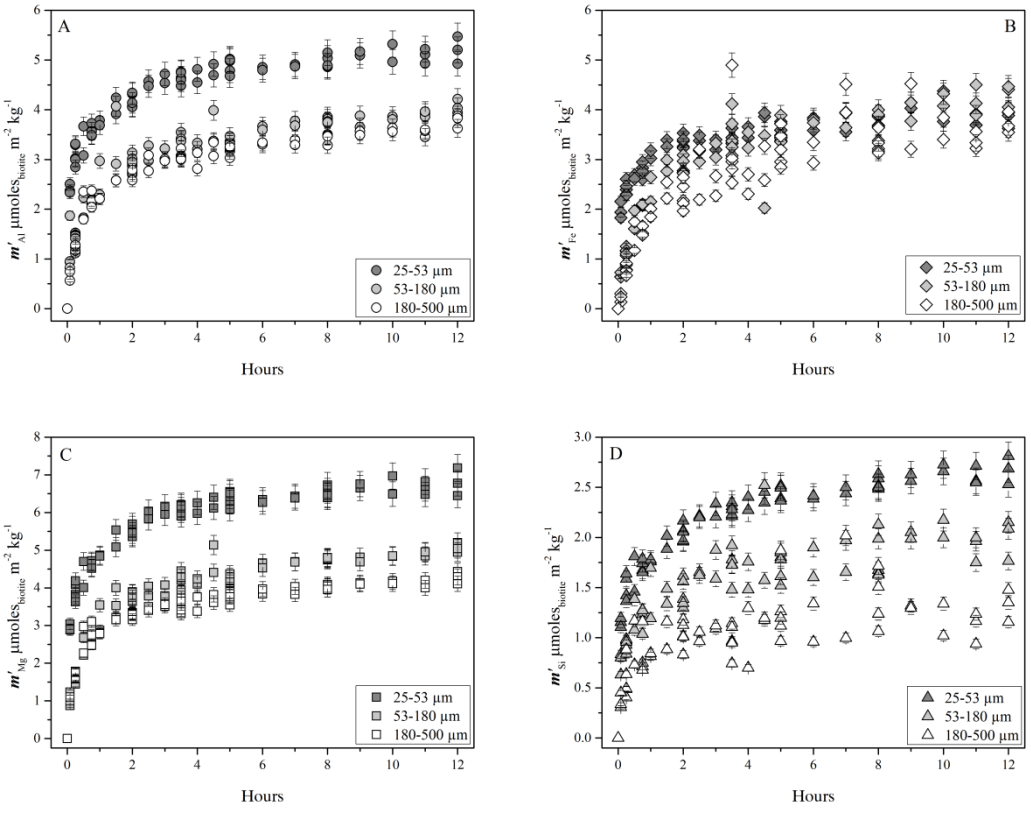

Figure 5.2

Surface area and stoichiometry normalised released moles (m'_i) as a function of time at pH 4 from the 25–53, 53–180, and 180–500 µm biotite size fractions. (A) aluminium, (B) iron, (C) magnesium, and (D) silicon.

53µm) released up to 1.3 and 2 times more Si than the 53–180 and 180–500 µm size fractions respectively. Fe release appears to be independent of particle size fraction, however this likely stems from secondary mineral precipitation as the fluid is supersaturated with respect to ferrihydrite after 12 hours for each size fraction (Table B–1), as calculated using the minteq.v4 database in PHREEQC3 (Parkhurst and Appelo, 2013).

In experiments with organic ligands present, there was no appreciable effect on Si release at pH 2.5 (Fig. 5.3A). At pH 3 and above, the presence of organic ligands increases element release relative to ligand free experiments with increasing pH. This is most evident for Fe and Al (Fig. 5.3B and 5.3C), and can also be seen for Mg in figure 5.3D.

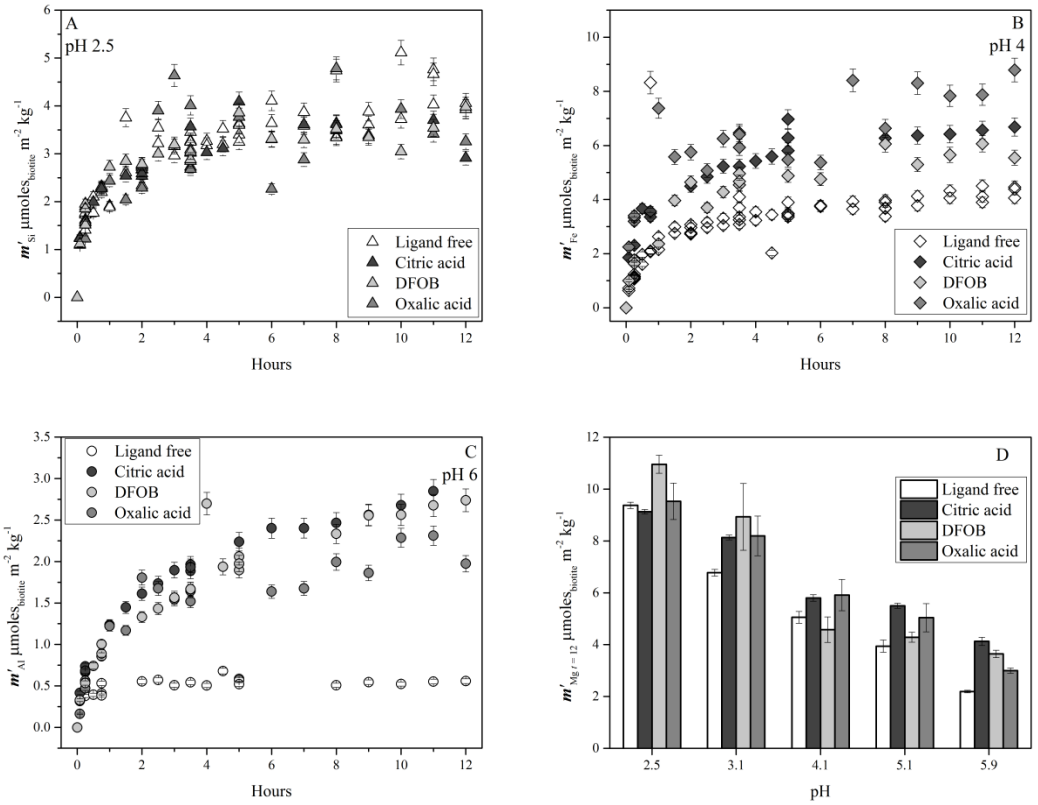

Figure 5.3

Element release in closed system experiments in the presence of organic acids. (A) Si release at pH 2.5, (B) Fe release at pH 4, (C) Al release at pH 6, and (D) Concentration of Mg after 12 hours.

These figures are representative of the overall trend of the effect of ligand presence observed for Al, Fe, Mg, and Si from pH 2.5 to 6 as presented in figure B–2. A comparison of the concentration of released Mg after 12 hours from ligand free and ligand bearing experiments is presented in Fig. 5.3D, illustrating the effect of organic ligands on Mg release. Above pH 4 the presence of ligands results in up to double the release of Si compared to the non organic-ligand bearing experiments (Fig. B–2).

The release of elements into the fluid over the course of 12 hour closed-system experiments follows a trend typical for most far from equilibrium closed-system dissolution studies (Oelkers et al., 2001) and can be modelled (Eq. 5.2, Fig. 5.1D) according to:

$$\boldsymbol{m'_{i,t}} = k' t^q$$

Eq. 5.2

where $\boldsymbol{m'_{i,t}}$ refers to the surface area and stoichiometry normalised number of moles of the *ith* element in the fluid phase at time t (Eq. 5.1), k' designates a rate constant (moles m^{-2} s^{-q}), t refers to time in seconds, and q stands for the exponential decay of the release rate (dimensionless). In Eq. 5.2, the values of k' and q can be derived through a linear regression of the logarithm of $\boldsymbol{m'_{i,t}}$ and t, where q corresponds to the slope of the regression and $\log k'$, its intercept ($\log t = 0$, $t = 1$ second). The values of k' and q for each experimental condition are listed in Table 5.3, along with the coefficients of determination.

Evaluating dissolution rates from closed-system experiments is challenging because kinetic calculations must consider the constantly changing fluid composition and the effect of possible saturation controlled back reactions (Oelkers et al., 2001; Brantley, 2003). Far from equilibrium closed-system dissolution experiments commonly follow the trend described by Eq. 5.2, where rapid release of elements occurs in the first stage of the reaction followed by a slower, decreasing release with time. This observation has been interpreted to stem from 1) the initial rapid release of elements from fine

particles or highly reactive sites, and 2) the slowing of rates due to an approach to equilibrium, or 3) a slowing of rates due to the increase of one or more aqueous species that inhibits dissolution (Oelkers and Schott, 2001; Saldi et al., 2007; Gautelier et al., 2007; Oelkers et al., 2008; Saldi et al., 2010). As such, we have determined rates directly from the derivative of the element release at a given point in the experiment. The analytical dissolution rate can be calculated from the derivative of Eq. 5.2:

$$r_{i,t} = \frac{\partial m'_i}{\partial t} = q k' t^{(q-1)}$$

Eq. 5.3

where $r_{i,t}$ represents the dissolution rate ($moles_{biotite}$ m^{-2} s^{-1}) with respect to the *ith* element at time *t*. The calculated biotite dissolution rates for each closed-system experiment at t = 1 second and t = 12 hours are shown in Table 5.3. These dissolution rates decrease with time for all elements, with the rate at 12 hours approximately 4 orders of magnitude slower than the initial dissolution rate (t = 1 second). The causes of the differences in these rates will be discussed below.

5. 3. 2. Open-system experiments

During the open-system experiments, which lasted up to 800 hours, the element release rates approached a near steady-state after approximately 100 hours (Fig. 5.4). Steady state was defined by the outlet fluids maintaining a constant concentration of Al, Fe, Mg, and Si, within 5% (analytical and experimental uncertainty) for a minimum of 3 residence times (reactor volume/flow rate). In the case of the Grasåsen biotite at pH 2, steady state occurred from 125 hours onwards. The average concentrations of elements released after 125 hours (Table 5.4) were used to calculate 'steady state' biotite dissolution rates according to:

$$r_i = \frac{\mathrm{f} \cdot \boldsymbol{c}_i}{\boldsymbol{s} \cdot M \cdot n_i}$$

Eq. 5.4

where r_i denotes the steady state dissolution rate ($mol_{biotite}$ m^{-2} s^{-1}), f symbolizes the fluid flow rate (kg s^{-1}), $\boldsymbol{c}_i$ signifies the aqueous concentration of the *ith* element in the outlet fluid (mol kg^{-1}), $\boldsymbol{s}$ stands for the initial specific surface area (m^2 g^{-1}, SSA_{BET} or SSA_{geo}) of the mineral powder of mass M (g), and n_i the stoichiometric coefficient of the *ith* element in the biotite formula (Table 5.1). The calculated biotite dissolution rates for each open-system experiment are listed in Table 5.4. Dissolution is not stoichiometric and decreased by ~1.5 orders of magnitude from pH 2 to 4 in the ligand-free experiments.

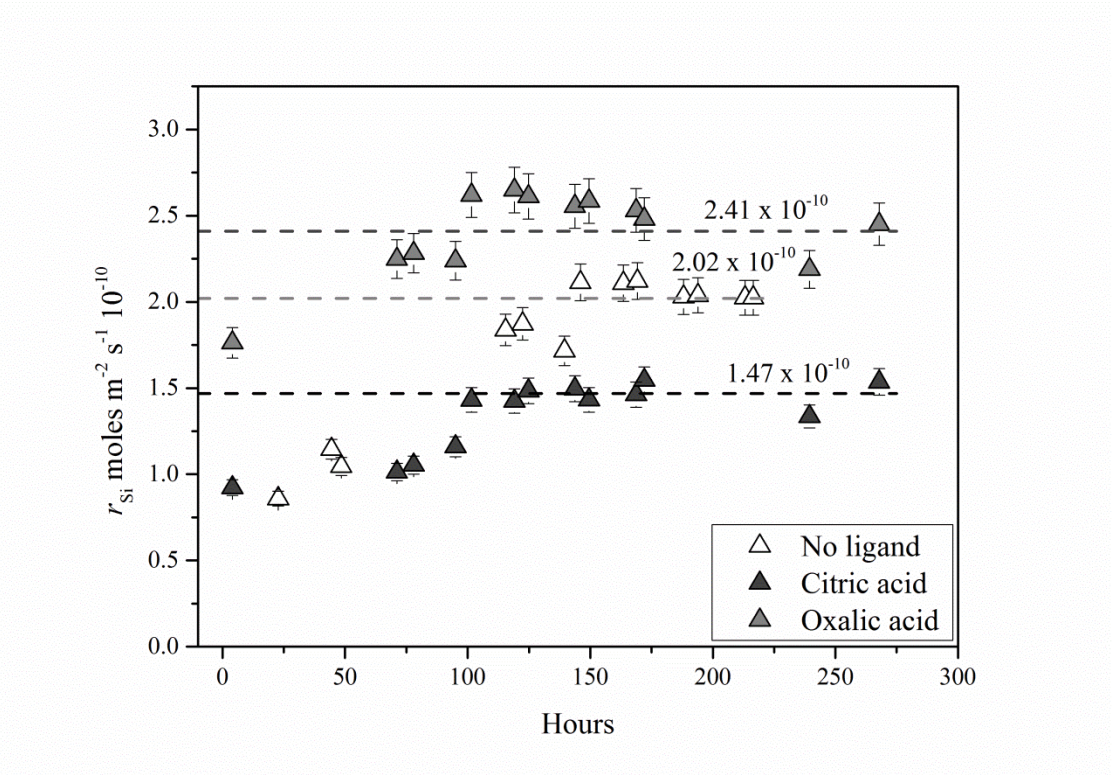

Figure 5.4

Biotite dissolution rates based on Si release from open system experiments. The dashed lines represent calculated steady state dissolution rates.

5. 4. DISCUSSION

5. 4. 1. pH dependent element release and dissolution

Consistent with the general trend of multi-oxide silicates (Oelkers and Schott, 2001; Golubev and Pokrovsky, 2006; Schott et al., 2012; Rimstidt et al., 2014; Stockmann et al., 2013), the Grasåsen and Moen biotite dissolution rates decrease with increasing pH from pH 2 to 6. The calculated open and closed-system ligand-free dissolution rates are plotted as a function of pH in Fig. 5.5A, along with biotite dissolution rates from the literature. The shaded area in Fig. 5.5A is used in Fig. 5.5B-D to highlight the range of kinetic data presented in the literature as a function of pH (Acker and Bricker, 1992;

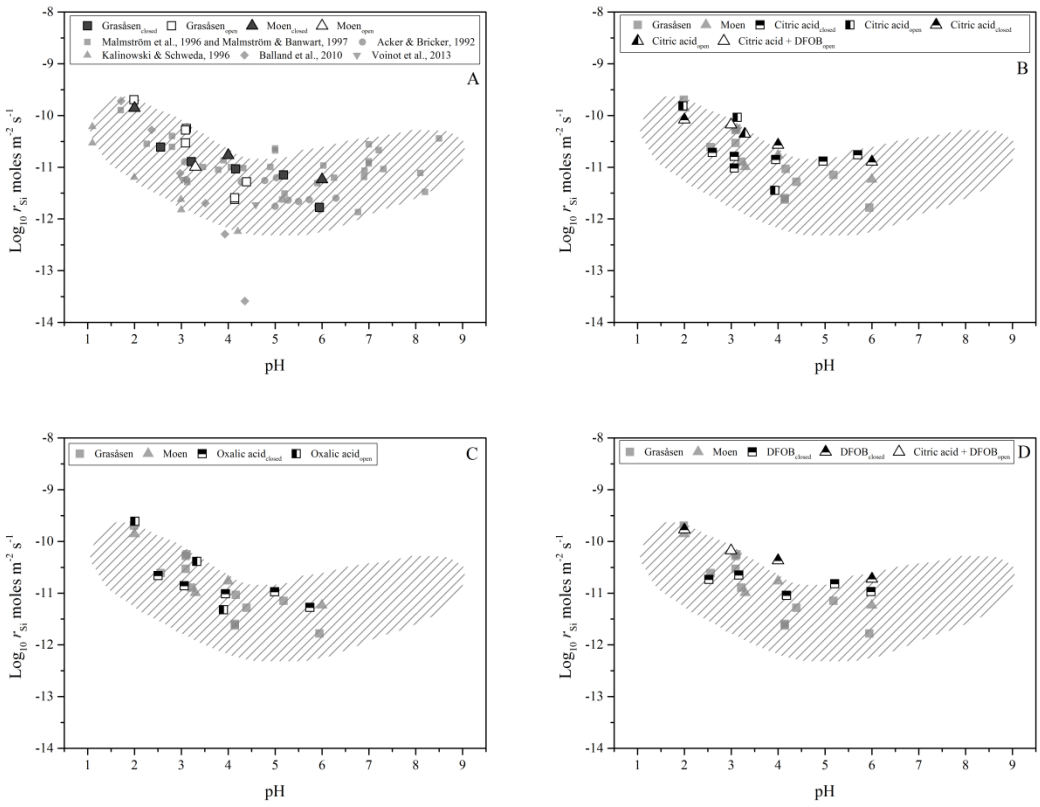

Figure 5.5

Biotite dissolution rate data from closed- and open-system experiments of Moen and Grasåsen biotite with literature data, plotted against pH. The shaded area guides the eye to the spread literature data. (A) ligand-free, (B) citric acid, (C) oxalic acid, and (D) DFOB. In figures B, C, and D, the light grey symbols represent the ligand-free Grasåsen and Moen open- and closed-system experimental data.

Kalinowski and Schweda, 1996; Malmström et al., 1996; Malmström and Banwart, 1997; Balland et al., 2010; Voinot et al., 2013). The closed-system rates plotted are those calculated at for t = 12 hours, as these are most consistent with open-system and literature data. It is worth noting that, at any given pH, biotite dissolution rates from the literature can range over 1.5 orders of magnitude.

This range of reported rates can be attributed to a number of differences. Firstly, differences in the bulk chemical composition of each biotite sample may result in a range of dissolution rates. The kinetic data from the literature presented in Fig. 5.5A span biotite samples from 3 locations: Bancroft, Ontario, Canada (Acker and Bricker, 1992; Voinot et al., 2013); Moen, Norway (Kalinowski and Schweda, 1996; Malmström et al., 1996; Malmström and Banwart, 1997); and Raze, Limousin, France (Balland et al., 2010). However, in the case of the biotite from Bancroft, Ontario, the reported Mg and Fe present in each sample vary, e.g. Acker and Bricker (1992) report moles of Mg and total Fe in one mole of biotite as 1.59 and 1.12 respectively, while in the biotite used by Voinot et al. (2013) Mg and Fe in the formula are 2.06 and 0.73 moles respectively. Secondly, the anisotropic nature of biotite surfaces has previously been described (Turpault and Trotignon, 1994; Hodson, 2006), differences in the grain size, surface area and geometry of reacting biotite grains may influence the reported dissolution rates. Thirdly, as highlighted above, the different experimental approaches, and experiment durations could also influence dissolution kinetics. Kohler et al. (2005) reported decreasing illite dissolution rates with time during flow-through experiments, and attributed these observations to the changes in clay morphology and a decrease in the number of reactive edge sites. The duration of flow-through biotite dissolution experiments in the literature, presented in Fig. 5.5A, ranges from approximately 300 (Acker and Bricker, 1992) to 3000 hours (Kalinowski and Schweda, 1996). Finally, variations in the chemical composition of the reactive fluids can influence dissolution rates, particularly in closed-

Table 5.5

Apparent rate constants k_H (10^{-9} moles m^{-2} s^{-1}), and reaction order x, with respect to hydrogen ion activity from the Moen and Grasåsen element release data.

		Grasåsen				Moen		
		Al	Fe	Mg	Si	Al	Fe	Mg
k_H 10^{-9} $moles_{biotite}$ m^{-2} s^{-1}		1.25	1.83	3.06	0.83	0.58	0.21	0.29
SE limits	max	3.40	3.96	8.14	1.95	1.84	16.86	1.02
	min	0.46	0.84	1.15	0.35	0.19	0.003	0.08
x		0.48	0.47	0.58	0.48	0.49	0.48	0.31
SE		0.11	0.09	0.11	0.10	0.15	0.59	0.13

system experiments where fluids may become supersaturated with respect to secondary phases.

In the case of the Grasåsen and Moen biotite, the dissolution rates determined in this study can be described as a function of pH using an empirical rate law for acid promoted dissolution (e.g. Lasaga, 1998)

$$r_i = k_{H,i} a_{H^+}^{x_i} \qquad \text{Eq. 5.5}$$

where r_i again refers to the dissolution rate of biotite based on the *ith* element, $k_{H,i}$, corresponds to a rate constant, and x refers to a reaction order with respect to proton activity.

Using Eq. 5.5, the rate constants and reaction orders derived from the ligand free experiments for both the Grasåsen and Moen biotite samples were determined by linear-least-square regression of log r_i against pH (Table 5.5; Fig. 5.5A) Results are comparable with the rate equations previously reported for biotite (Acker and Bricker, 1992; Kalinowski and Schweda, 1996, Malmström et al., 1996; Malmström and Banwart, 1997; Balland et al., 2010).

The data derived from the biotite dissolution experiments performed in the presence of citric acid, oxalic acid, and DFOB (Fig. 5B-D) generally lie within the shaded region of the ligand-free biotite dissolution rates shown in Fig. 5.5A. At pH 2 to 4, the

biotite dissolution rates in the presence of citric acid, oxalic acid, and DFOB were within the range of the ligand free data from this study, and the literature. Above pH 4 a slight enhancement in dissolution rate can be seen in the presence of citric acid, oxalic acid, and DFOB when compared to the data from this study, however, these rates are within the range of biotite dissolution rates reported previously (Fig. 5.5B-D). In comparison, Balland et al. (2010) reported an enhanced ligand promoted release rate of Fe, which was up to 2 orders of magnitude faster than in a corresponding ligand-free experiment. Balland et al. (2010) conducted biotite dissolution experiments in the presence of citric acid and gluconic acid at ligand concentrations between 10^{-3} and 10^{-2} M. Similarly, Voinot et al. (2013) reported an order of magnitude enhancement of biotite dissolution rates in the presence of citric acid, but saw no enhancement in the presence of a siderophore. In the current study, the apparent lack of enhancement or inhibition of element release from biotite in the presence of organic ligands may be explained by two reasons: (1) the relatively low concentration of organic ligand used in the reactive fluids, and (2) that biotite dissolution rates have been computed from Si release rather than the release of other aqueous metals, see discussion below. With respect to organic ligand concentrations, in the current study, concentrations of citric and oxalic acid were 500 μM each, and DFOB was 500 μM and 145 μM in the closed- and open-system experiments respectively, consistent with the range of organic ligand production by mycorrhizal soil microorganisms in the literature (Lapeyrie et al., 1987; Lapeyrie 1988; Adeyemi and Gadd, 2005). The concentration of citric acid used in this study was 2 to 20 times lower than the concentration used by Balland et al. (2010), the concentration of siderophore used by Voinot et al. (2013) is in range of DFOB used in this study, although the citric acid concentration used by Voinot et al., 2013 is not available. It has been shown previously that, in at least some cases, a system requires a minimum concentration of

organic ligands before an appreciable effect (i.e. a doubling of dissolution rate) is seen (> 10^{-3} M, Golubev et al., 2006).

The biotite dissolution rates presented in Fig. 5.5 were calculated based on the temporal evolution of reactive fluid Si concentrations. One of the reasons for the reported effect of citric acid on biotite dissolution rates in the study of Balland et al. (2010) is because the authors used dissolved Fe concentrations, a metal to which citrate has a strong affinity, to calculate their rates. Note that Fe has low solubility at slightly acidic pH in the absence of organic ligands, an increase in fluid citric acid concentration increases Fe solubility leading to the appearance of faster rates in this previous study. This conclusion is emphasized in Fig. 5.6, which shows the speciation and metal complexation of (A) phthalate buffer, (B) citric acid, (C) oxalic acid and (D) DFOB as a function of pH, calculated from the acid dissociation and stability constants of each ligand (Table B–1) and the concentrations of Al, Fe and Mg after 12 hours at pH 2.5, using the PHREEQC 3 computer code (Parkhurst and Appelo, 2013). In the presence of citric acid (Fig. 5.6B) the majority of Fe and Al in aqueous solution forms citrate complexes above pH 2 and 3 respectively, however Mg–citrate complexes do not become dominant until above pH 6. This poor affinity for the formation of Mg-organic ligand complexes is also reflected in the oxalic acid and DFOB speciation. At pH 1, Fe–oxalate and Fe–DFOB complexes are the dominant form of dissolved Fe, and Al-oxalate, Al-DFOB complexes dominate above pH 2.5 and 2 respectively (Fig 5.6C and 5.6D). The poor affinity of citrate, oxalate and DFOB species for Mg is not due to exhaustion of the ligands in solution, metal-ligand complexes represent a maximum of 2% of total ligand concentration. The saturation state of the reactive fluids with respect to potential secondary phases in all experiments is shown in Table B–2. Compared to a fluid calculated using NaCl as a background electrolyte, the presence of phthalate has little effect of Al and Fe secondary phase saturation. This is due to the poor affinity of

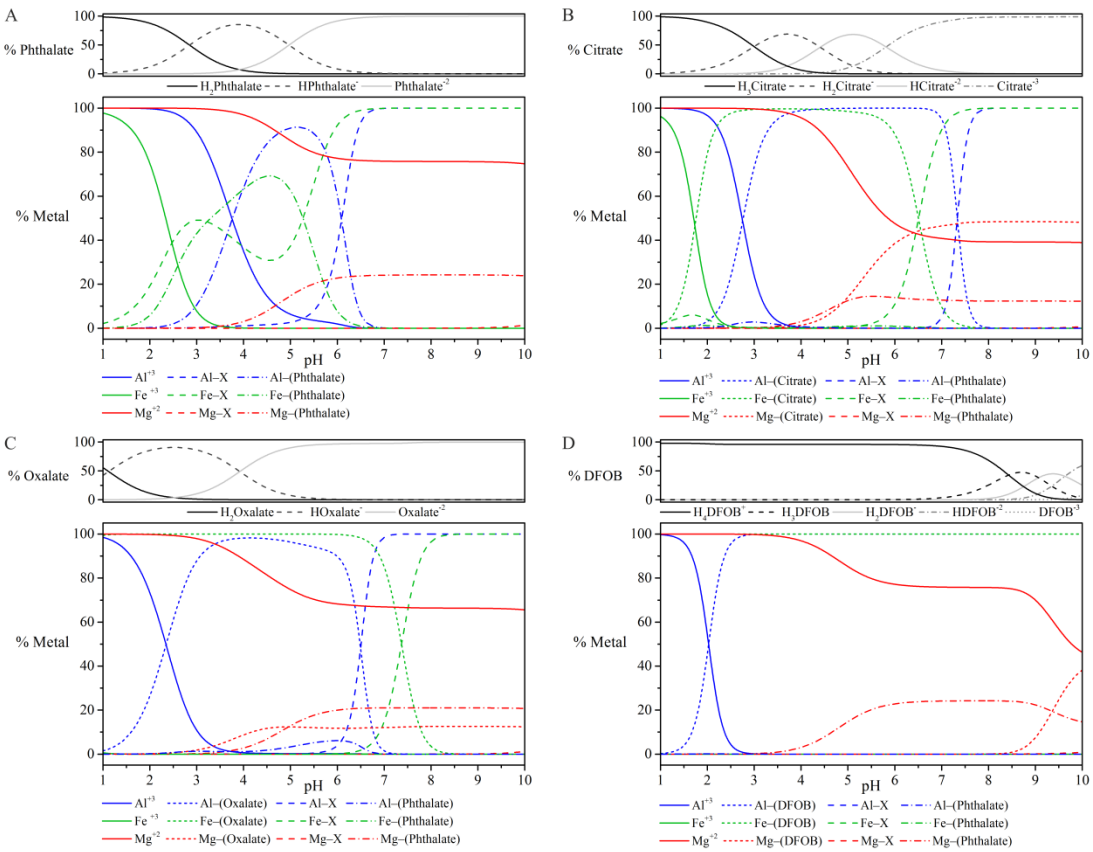

Figure 5.6

Metal speciation as a function of pH from the closed-system experiments in the presence of (A) the phthalate buffer, (B) citric acid, (C) oxalic acid, and (D) DFOB. Calculated using PHREEQC 3 (Parkhurst and Appelo, 2013), experimentally determined metal concentrations, and equilibrium constants from the literature (Table B–2).

phthalate for metals. In the ligand-free experiment, reactive fluids at pH ≥ 3 are supersaturated with respect to ferrihydrite, and supersaturated with respect to gibbsite at pH > 5. However, the calculated saturation indices for ferrihydrite and gibbsite in experimental fluids are all below zero in the presence of citric acid, oxalic acid and DFOB at pH 2.5 to 4, with ferrihydrite is supersaturated in the presence of citric acid at pH >4, and both ferrihydrite and gibbsite are supersaturated in the presence of oxalic acid at pH > 5. The presence of organic ligands therefore decreases secondary phase saturation, allowing the further release of Al and Fe into the reactive fluid.

The mechanism by which an organic ligand influences mineral dissolution has been described as complexation, either direct (surface complexation) or indirect

(solution based chelation, c.f. Drever and Stillings, 1997). In the case of biotite, it is likely that metal-ligand complexation occurs mainly in the fluid phase. In our previous study on the Grasåsen biotite (Bray et al., 2014) we demonstrated that the isoelectric point of biotite is at pH 3. Below this pH, the biotite surface has a net positive charge, above this pH, a net negative charge. Above pH 3 the dominant species of citric and oxalic acid are negatively charged such that interaction with the negatively charged biotite surface is likely limited. However, the dominant DFOB species in the range of pH of this study (2 – 6) is the positively charged H_4DFOB^+ species. It has been demonstrated previously that DFOB adsorption to mineral surfaces promotes Al and Fe release to solution (Hersman et al., 1995; Holmén and Casey, 1996; Kraemer et al., 1999; Cocozza et al., 2002; Cheah et al., 2003; Rosenberg and Maurice, 2003; Kraemer, 2004; Wolff-Boenisch et al., 2006; Buss et al., 2007; Reichard et al., 2007).

5. 4. 2. Surface area and dissolution

The surface area normalised dissolution rates of the three Grasåsen size fractions do not appear to depend on total mineral surface area present (SA_{BET} m^2, Fig. 5.7). This observation may stem from the anisotropic nature of biotite surface reactivity, which has been previously described in detail (e.g. Turpault and Trotignon, 1994; Hodson, 2006). However, the logarithm of the dissolution rates apparently exhibit a linear correlation with the fraction of geometric specific surface attributed to the biotite edges (*h k* 0, SA_{edge} %, Fig 5.7), demonstrating the importance of grain geometry on the overall dissolution rate. Biotite, like other sheet silicates has been shown to primarily dissolve parallel to the basal surface, i.e. at the (*h k* 0) surfaces (Kaviratna and Pinnavaia, 1994; Turpault and Trotignon, 1994; Bosbach et al., 2000; Bickmore et al., 2001, 2003; Hodson, 2006; Aldushin et al., 2006; Saldi et al., 2007; Cappelli et al., 2013).

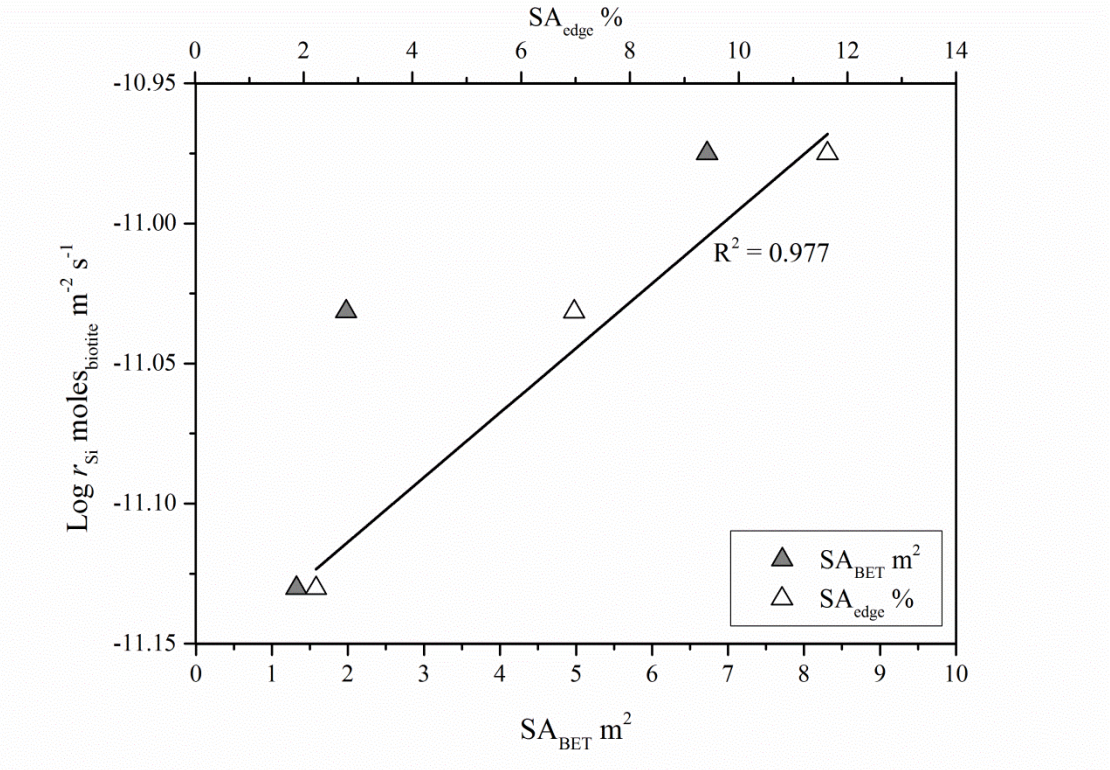

Figure 5.7

Biotite dissolution for each size fraction plotted against SSA_{BET} (grey squares), and $\%SA_{edge}$ (open squares).the line is the regression of the $\%SA_{edge}$ plot. Note the dual *x*-axis.

From the grain geometry measurements made using FEG-SEM (see 5.2.1), the overall biotite dissolution rate constant at a single pH (k'_{Si}, Eq. 5.2) can be considered to be the sum of two contributions in accord with (e.g. Hodson, 2006)

$$k'_{Si} = k'_{Si,edge} \cdot SA_{edge} + k'_{Si,basal} \cdot SA_{basal}$$

Eq. 5.6

where $k'_{Si,edge}$ and $k'_{Si,basal}$ (moles m^{-2} s^{-q}) correspond to the rate constants of the edge and basal surfaces respectively, and SA_{edge} and SA_{basal} designate the fraction of edge and basal surfaces of the total geometric surface area (Table 5.2). The values of $k'_{Si,edge}$ and $k'_{Si,basal}$ are obtained from extrapolating the linear regression of k'_{Si} with $\%SA_{edge}$ and $\%SA_{basal}$ to 0% SA_{basal} and SA_{edge} respectively. At pH ~4 the value of $k'_{Si,edge}$ is 36.7 × 10^{-7} (moles m^{-2} s^{-q}), approximately 120 times greater than $k'_{Si,basal}$, 0.31 × 10^{-7} (moles m^{-2} s^{-q}). The relative reactivities of the edge and basal surfaces based on the other elements

differ, using the same method; the values of $k'_{\mathrm{Al,edge}}$ and $k'_{\mathrm{Mg,edge}}$ are 102 and 45 times greater than $k'_{\mathrm{Al,basal}}$ and $k'_{\mathrm{Mg,basal}}$, respectively. The relative reactivity of the edge and basal surfaces could not be calculated for Fe, as iron release was independent of grain geometry (see 5.3.1). These calculations, although limited by the extrapolation of experimental data, suggest that the relative reactivities are element specific. The calculated relative reactivity ratios of (h k 0) : (0 0 1) for each element (excluding Fe) fall within the range given by Turpault and Trotignon (1994) of 30 to 300, and Hodson (2006) of 71 to 132. However, the range presented in this study is pH specific and may change with pH due to corresponding biotite surface compositional changes (Bray et al., 2014).

An example of the relative contribution of basal versus edge dissolution is presented in Fig 5.8A-C. The relative rates in this figure were calculated from the sum of two distinct contributions in accord with

$$\boldsymbol{m}_{Si} = \left(k'_{\mathrm{edge}} \cdot t^{q} \cdot \mathrm{SA}_{\mathrm{edge}}\right) + \left(k'_{\mathrm{basal}} \cdot t^{q} \cdot \mathrm{SA}_{\mathrm{basal}}\right)$$

Eq. 5.7

The model describes well the corresponding data, as seen in Fig. 5.8D. It is worth noting that the values of k'_{edge} and k'_{basal} were calculated using a fixed average value of q (see Eq. 5.1) as this parameter varies by 0.06 as a function of grain size (Table 5.3). However, the modelled concentrations (Eq. 5.7, Fig. 5.8) were calculated using the values for q provided in Table 5.3 (see experiments 24–26 and 33–38).

It is also worth noting that $\mathrm{SSA_{geo}}$ for each of the size fractions is significantly less than the corresponding $\mathrm{SSA_{BET}}$. The ratio of $\mathrm{SSA_{BET}/SSA_{geo}}$, or roughness factor (Wolff-Boenisch et al., 2004), for the Grasåsen biotite ranges between ~8 for the 25-53 μm size fraction and ~3 for the 180-500 μm) size fraction. The biotite surface consists of relatively smooth basal surfaces and rough edges (see Fig. B–1), so when the grains are predominantly free of smaller particles adhered to surfaces it follows that the roughness

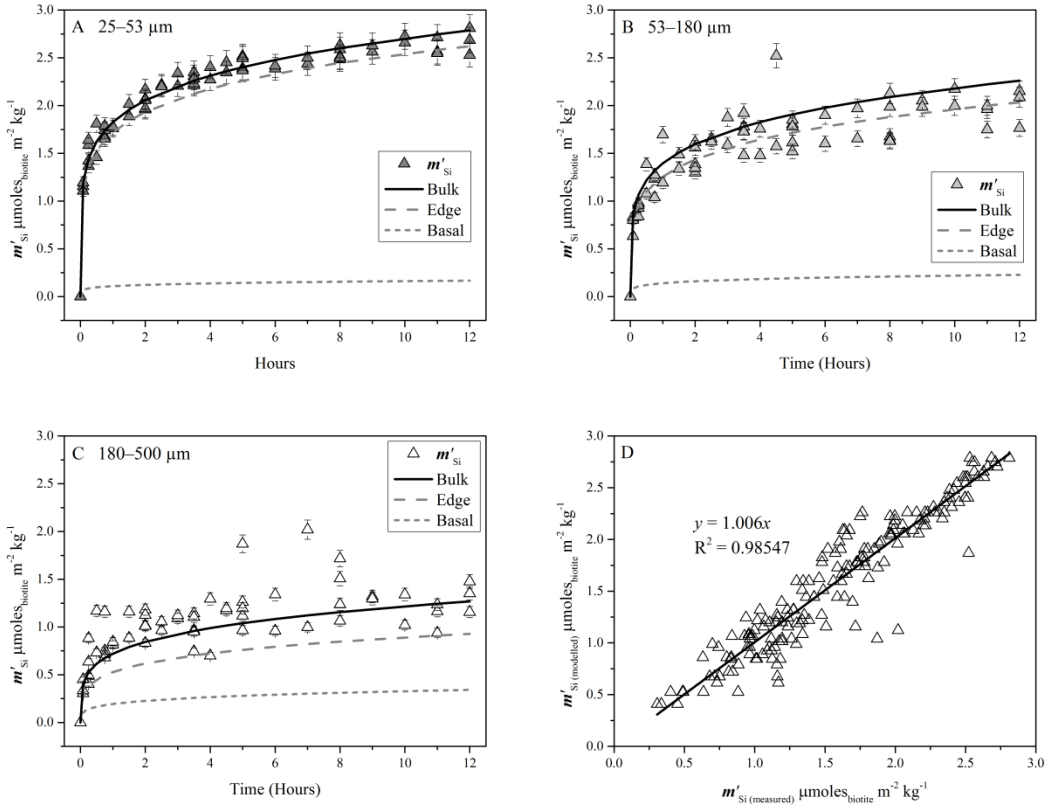

Figure 5.8

Modelled element release from the edge and basal surfaces plotted with experimental data for the three size fractions at pH 4 (A) 25–53, (B) 53–180, and (C) 180–500. The suitability of the model to represent experimental data can be assessed with (D), a plot of modelled against experimentally determined surface area and stoichiometry normalised moles released ($\boldsymbol{m'_i}$).

factor is directly linked to SA_{edge}. This also suggests that the values of SA_{edge} may underestimate the actual surface area present on the edge surfaces of biotite grains. If the SA_{edge} values were larger, then the calculated edge reactivity would be significantly lower.

Table 5.6

Average element release ratios from the Grasåsen biotite with 2 S.D. given in parentheses.

	Ligand free		Citric acid		DFOB		Oxalic acid	
	closed	open	closed	open	closed	open	closed	open
[Mg]/[Si]	2.70 (0.55)	1.79 (0.35)	3.06 (1.07)	1.85 (0.44)	3.33 (0.96)	-	2.85 (1.09)	1.54 (0.32)
[Al]/[Si]	2.15 (0.54)	1.48 (0.56)	2.87 (1.17)	1.87 (0.46)	3.02 (1.10)	-	3.01 (0.83)	1.61 (0.65)
[Fe]/[Si]	2.02 (0.82)	2.22 (0.73)	3.09 (1.16)	1.97 (0.64)	3.85 (1.37)	-	3.37 (1.06)	1.77 (0.52)

5. 4. 3. Stoichiometry of dissolution

The stoichiometry of element release from the biotite structure during the first 12 hours of reaction in closed-system experiments can be assessed by plotting the stoichiometry and surface area normalised moles of each metal released from biotite ($\boldsymbol{m'_i}$) against the corresponding moles of Si (Fig 5.9), and calculating the $\boldsymbol{m'_i/m'_{Si}}$ ratios (Table 5.6). In the ligand-free closed-system dissolution experiments the ratio of $\boldsymbol{m'_{Mg}/m'_{Si}}$ (Fig. 5.9A) is pH independent and is far from stoichiometric revealing an average ratio of 2.7 (S.D. 0.6). This non-stoichiometric release also represents the $\boldsymbol{m'_{Al}/m'_{Si}}$ (Fig. 5.9B) and $\boldsymbol{m'_{Fe}/m'_{Si}}$ (Fig. 5.9C) ratios which have averages of 2.2 and 2.2 respectively (S.D. 0.5 and 0.8). In the open-system experiments, the ratio of $\boldsymbol{m'_i/m'_{Si}}$, at all pH values decreases during each experiment but in general remains greater than 1 after 300 hours of reaction. In one experiment at pH 3 $\boldsymbol{m'_{Al}/m'_{Si}}$ ratio reached 0.7 after ~250 hours. Non-stoichiometric release of structural metals has previously been described for biotite (Acker & Bricker, 1992; Kalinowski & Schweda, 1994; Turpault and Trotignon, 1994; Malmstrom and Banwart 1997). It is worth noting that towards neutral pH the ratios of $\boldsymbol{m'_{Al}/m'_{Si}}$ and $\boldsymbol{m'_{Fe}/m'_{Si}}$ decrease (see insets of Fig. 5.9B and 5.9C). At pH 6 the ratios for these elements are 1.04 and 0.48 respectively (S.D. 0.16 and 0.17), indicating near-stoichiometric release of Al and retention of Fe in the solid phase. This approach to stoichiometric Al release and Fe retention in the solid phase at pH 6 is likely

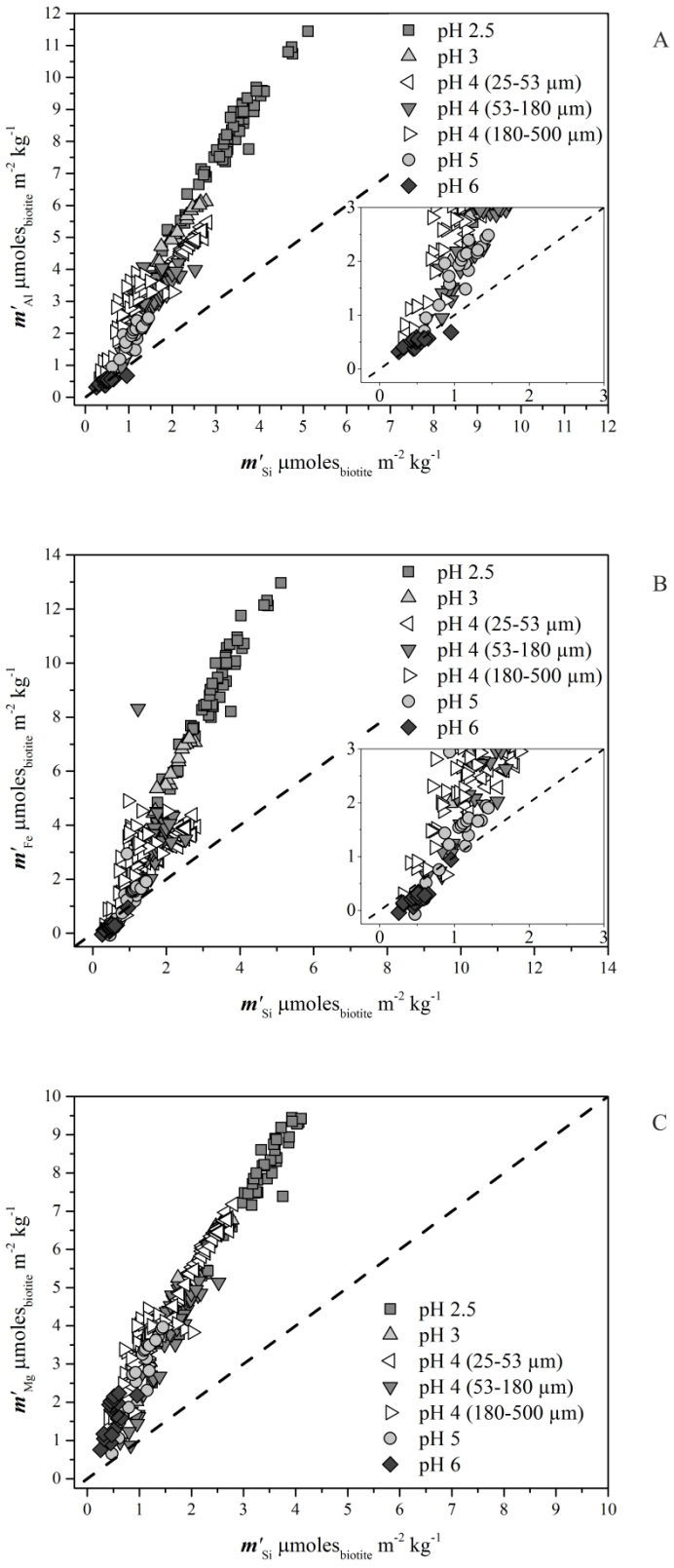

Figure 5.9

Plots of released (A) Mg, (B) Al, and (C) Fe against released Si in closed system experiments, the dashed line represents stoichiometric release and the insets highlight the lower regions of the plots.

due to the precipitation of secondary Al and Fe oxy-hydroxide phases. Indeed in the ligand-free closed-system experiments at pH 6 fluids are calculated to be supersaturated with respect to boehmite, gibbsite, and ferrihydrite. In fact ferrihydrite is supersaturated at pH 3 and above.

The $\boldsymbol{m'}_i/\boldsymbol{m'}_{Si}$ ratios in the presence of organic ligands are presented in figure 5.10. In general, the $\boldsymbol{m'}_i/\boldsymbol{m'}_{Si}$ ratios increase in the presence of organic ligands with respect to the ligand-free experiments (Table 5.6). With citric (Fig. 5.10A and B) and oxalic acid or

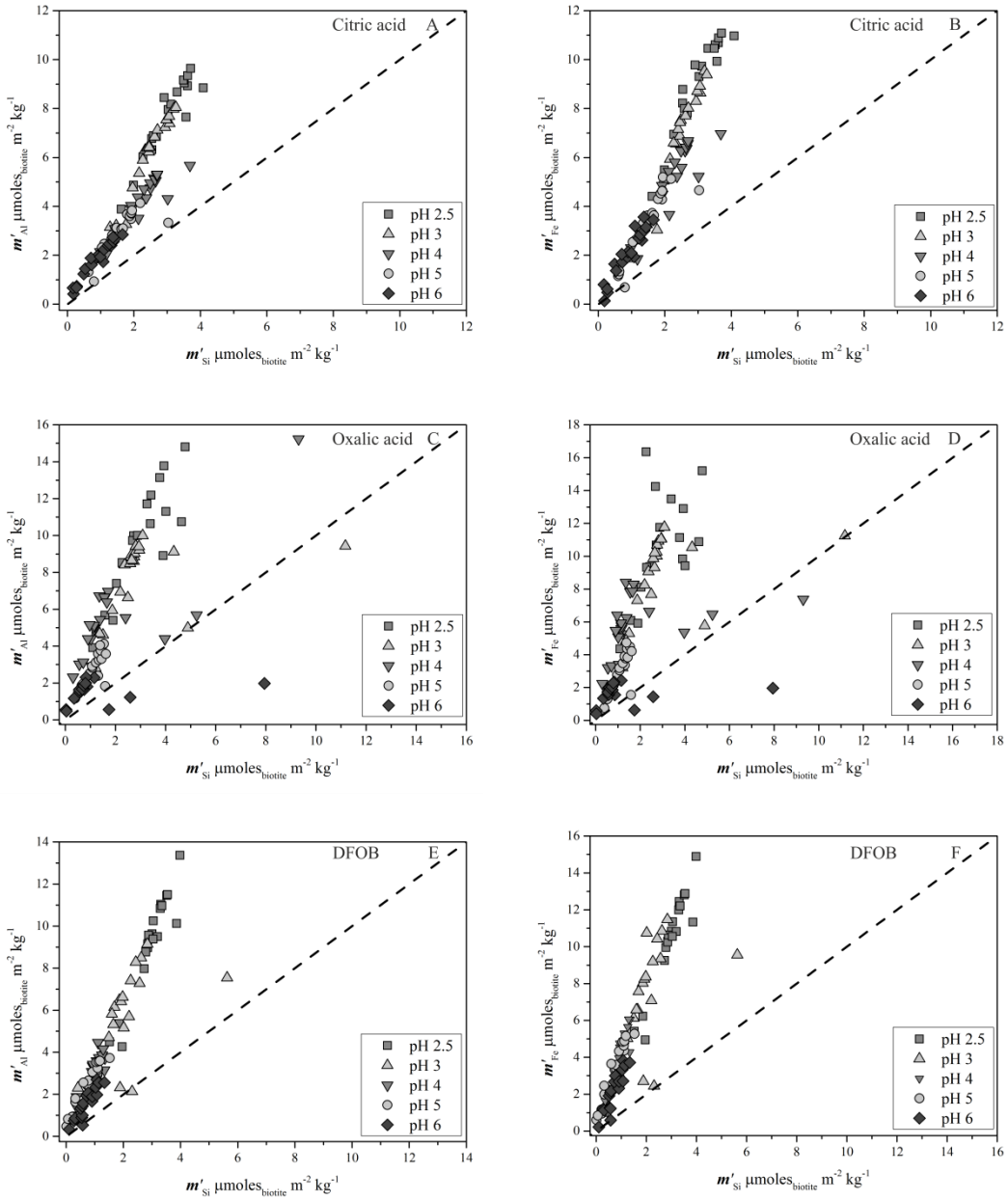

Figure 5.10

Plots of release Al and Fe against Si in closed-system experiments in (A, B) citric acid, (C, D) oxalic acid, and (E, F) DFOB.

DFOB (Fig. 5.10C-F) present in the experimental fluid the ratios for $\boldsymbol{m'}_{Al}/\boldsymbol{m'}_{Si}$ and $\boldsymbol{m'}_{Fe}/\boldsymbol{m'}_{Si}$ at pH 5 and 6 are more consistent with the respective ratios at lower pH. This enhanced release of metals in the presence of organic ligands likely stems from the increased solubility of Fe and Al (Fig. 5.6).

5. 4. 4. Dissolution mechanism

Bray et al., (2014) demonstrated the formation of Mg and Fe depleted tetrahedral and Al depleted octahedral layers at the biotite surface at low pH. The average depth of this depleted layer was calculated from (Bray et al., 2014).

$$\mathrm{Dep}_i = \frac{\boldsymbol{m}_i}{n_i \left(\frac{\rho_{\mathrm{biotite}}}{\mathbf{m}_{\mathrm{biotite}}} \cdot \frac{N}{10^{21}} \right)}$$

Eq. 5.8

The average depth of removal of the *ith* element (Dep_i) is calculated by dividing the moles of the *ith* element removed from the biotite during dissolution experiment ($\boldsymbol{m}_i$) by the average density of atoms in the biotite structure (atoms nm^{-3}), where n_i is the stoichiometric coefficient of the *ith* element in the bulk biotite, ρ_{biotite} (g cm^{-3}) represents the biotite density (3.09, average from webmineral.com) and $\mathbf{m}_{\mathrm{biotite}}$ refers to the molecular mass of biotite (450.15g mol^{-1} for the Grasåsen biotite). Bray et al. (2014) calculated depletion depths based on the total released moles of elements, ignoring the relative reactivities of the basal (0 0 1) and edge (*h k* 0) surfaces. Here we can calculate the depth of element removal from biotite from both the basal (0 0 1) and edge (*h k* 0) planes by replacing $\boldsymbol{m}_i$ in Eq. 5.8 with released moles from the basal and edge surfaces. As we cannot attribute Fe release to the basal and edge surfaces we will use the Si derived relative surface reactivities calculated above. This calculation aids the visualisation of the biotite surface during its dissolution, both in the presence and absence of organic ligands (Fig. 5.11). As the edge surfaces are 120 times more reactive than the basal surfaces the majority of dissolution occurs perpendicular to the (0 0 1)

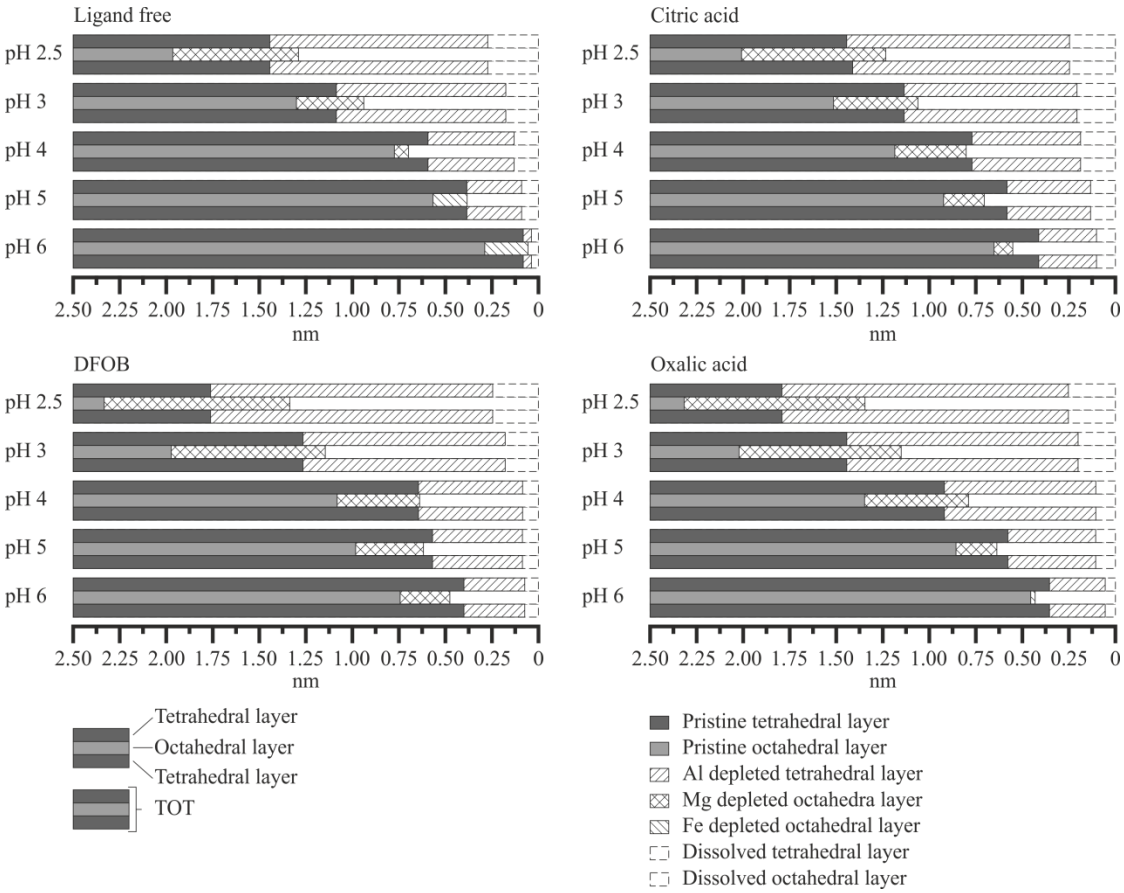

Figure 5.11

Calculated depths of dissolution fronts in the tetrahedral and octahedral layers as a function of pH and organic ligand. Calculations based on the reactivity of (*h k 0*) and released concentrations after 12 hours.

plane. Figure 5.11 depicts the extent of element removal from biotite after 12 hours as a function of pH and presence of organic ligands. Released elements are attributed to either tetrahedral or octahedral sites depending on the biotite structure. At all pH in both organic ligand bearing and ligand free experiments, octahedral metal (Fe, Mg) release is greater than tetrahedral element (Al and Si) release. In the organic ligand free experiments, Fe is preferentially released over Mg from the octahedral layer at pH 2.5 to 4, whereas at pH 5 and 6, Fe is preferentially retained over Mg. This change in element release is likely due to the control of secondary phase equilibria on Fe release above pH 5, where Fe-oxyhydroxide solubility is lowest. It is unclear from these experiments if Fe retention is within the biotite structure or as a secondary mineral precipitate, in figure

5.11 it is represented as remaining in the biotite structure. The preferential retention of Fe in the solid phase at near neutral conditions is not seen in the presence of citric acid or DFOB, due their effect on increasing Fe solubility. In the presence of oxalic acid, preferential Fe release occurs at pH 5 but not pH 6. It is also likely that $Fe^{(II)}$ oxidation may be occurring within the biotite structure, forming $Fe^{(III)}$ subdomains, however the quantification of Fe oxidation is beyond the scope of this study. Similarly, the release of Al from tetrahedral sites in the presence of organic ligands is greatly increased compared to the ligand-free experiments above pH 3. The depth of Al removal at pH 6 in the presence of organic ligands is approximately 2.5 times greater than in the ligand free experiments. Biotite dissolution is known to proceed non-stoichiometrically (Kalinowski and Schweda, 1996; Malmström et al., 1996; Malmström and Banwart, 1997; Voinot et al., 2013; Bray et al., 2014), however Acker and Bricker (1992) suggested that dissolution of octahedral and tetrahedral layers was internally stoichiometric, i.e., Fe and Mg release from the octahedral layer was stoichiometric but non stoichiometric compared to the bulk chemistry. Figure 5.11 demonstrates that for Grasåsen biotite, this is not the case. Indeed, Mg and Fe release from the octahedral layer is not stoichiometric; similarly Al and Si release from the tetrahedral layer is also non stoichiometric.

5. CONCLUSION

The results summarized above illustrate the complex, but systematic dissolution behaviour of biotite, a common sheet silicate mineral. Dissolution is dominated at the biotite edges. Dissolution at these edges at acidic conditions occurs from the independent removal of the cations at distinct rates, where Mg and Fe are in general released faster than Al, which itself is released faster than Si. As a result, with time the biotite edges change composition and structure, the outermost edge consisting of an Al depleted tetrahedral framework adjacent to a Mg, Fe depleted octahedral layer. As one

continues deeper into the biotite increasing Al, Mg, and Fe are present until a stoichiometric biotite is found deep with the mineral grains. As rates are dominated by removal of material from edge surfaces, which constitute only a small fraction of the total biotite surface area, the degree to which total surface area normalized rates can represent natural processes is questionable. The biotite dissolution behaviour presented in this study highlights the need of soil dwelling micro-organisms to expose highly reactive (*h k* 0) surfaces through the chemical and physical forcing involved in bio-fracking to extract nutrients (Bonneville et al., 2009; Bonneville et al., 2011; Gazzè et al., 2012; Gazzè et al., 2013).

Chapter 6. Fungal growth and biochemical functionality

Chapter 6 addresses the third research objective outlined in the introduction, to determine the growth kinetics and surface coverage of a mycorrhizal fungus on a mineral surface, and determine the spatial biochemistry of a fungal hypha to assess what controls hypha functionality. In this chapter we highlight the suitability of optical microscopy to image fungal hyphae *in situ*, and the usefulness of μ-FTIR for observing spatial variations in fungal biochemistry. We provide an average growth rate of 10 m d^{-1} for fungi in symbiosis with a tree growing in 1500 ppm CO_2.

Abstract

Mycorrhizal fungi are key players in the mobilisation, acquisition and supply of nutrients from minerals to plants. Recent advances in understanding of the mechanism and kinetics of fungal mineral weathering have demonstrated the need for a more quantitate assessment of fungal growth rates and of their biochemical functionality while growing over a nutrient source. Here, I present the first *in situ* measurements of growth rates of the fungus *Paxillus involutus* growing over a biotite flake surface, while living in symbiosis with its tree partner *Pinus* sylvestris. The growth of individual hyphae over the mineral surface was tracked in plant-fungal-biotite continuum microcosms at two different CO_2 levels to mimic current ambient (350 ppm) and past or predicted future high CO_2 (1500 ppm) levels. Measurements of fungal advance were acquired through sequential images collected over 5 to 10 days using an optical microscope. Initial estimates of the fungal growth rates at 1500 ppm CO_2 are approximately 10 μm d^{-1}. Furthermore, to assess changes in biochemical make up of fungal hyphae during growth over a biotite surface the spatial variation of biochemical functional groups of individual hypha were measured using synchrotron based Fourier transform infrared microspectroscopy (μ-FTIR). A combination of point measurements along hyphal strands

as well as focal planar array (FPA) mapping has highlighted clear differences in functional group make up of the tip and of the more mature areas of individual hyphae. The quantification of the fungal growth kinetics and the biochemical consequences of hyphal growth over the biotite surface presented in this study aids in the refinement of our understanding of plant-driven fungal mineral weathering. The observed biochemical variations along a hypha seem to suggest that different parts of fungal hyphae have specific functionalities involved in mineral weathering.

6. 1. INTRODUCTION

It is widely accepted that life plays an important role in mineral weathering and the formation of soils. Recent studies have highlighted the importance of plant-fungi symbiotes in extracting nutrient elements from minerals in exchange for a significant portion of a plant's net photosynthate (Ek, 1997; Read et al., 2004; Hobbie and Wallander, 2006; Leake et al., 2008; Smits et al., 2008; Bonneville et al., 2009; Bonneville et al., 2011). The co-evolution of large vascular plants and mycorrhizal fungi resulted in a clear CO_2 drawdown from the atmosphere during the Phanerozoic (Beerling and Berner, 2005) and this link has continued to control atmospheric CO_2 regulation since (Taylor et al., 2009; Quirk et al., 2012; Quirk et al., 2014).

Such mycorrhizal influences although they affect global scale processes, actually occur at the micro to nano scale, and specifically at the interface between life (fungi) and rocks (mineral substrate surfaces). All fungi, but ectomycorrhizal fungal hyphae in particular, are excellent at extracting nutrients from minerals by 'bio-fracking'; distorting the crystal structure, creating new surfaces, exuding extracellular polymeric substances (EPS) around growing hyphae, and thus acidifying the local environment (Bonneville et al, 2009; Saccone et al., 2012; Gazzè et al., 2012; Smits et al 2012; Gazzè et al., 2013). Studying element release in long term hyphal-biotite interaction experiments, Bonneville

et al. (2009) suggested that the biotite lattice distortion observed beneath growing hyphae was a result of fungal attachment to, and growth over, the mineral surface. Fungi are able to bind strongly onto mineral surfaces via class I hydrophobins, which are present in *Paxillus involutus* and all other basidiomycete fungi. (Wosten et al., 1993). Hyphal tips are likely to be able to exert relatively large forces externally due to their internal pressure, which ranges between 0.4 to 1 MPa and, in specific fungal structures by up to 8 MPa (Harold, 2002; Bechinger et al., 1999). Being able to exert such pressures has led to the suggestion that this ability may, in part, drive fungal growth. Furthermore, in some cases, such pressures may allow certain strains of fungi to even penetrate (bore) into solid material, such as plant tissue and mineral surfaces. In the case of mineral substrates this may lead to major changes in the crystal structure of the substrates (Jongmans et al., 1997; Money, 1999; Bastmeyer et al., 2002; Bonneville et al., 2009). However, most of these processes are not well understood because fungal growth processes are poorly understood. Recently, Gazzè et al. (2012) also suggested that, combined with the physical forces, increased organic ligand exudation at the tip of a growing hyphae could induce the formation of channels on a phyllosilicate basal (0 0 1) surface. While growing, the cell wall close to the tip of a hypha becomes more permeable, allowing for tip expansion (Gooday, 1996; Sun et al., 1996; Bartnicki-Garcia et al., 2000). This permeability also allows for the increased secretion of organic ligands, possibly enhancing weathering and channel formation (Saconne et al., 2012; Gazzè et al., 2012). Although long term exposure experiments (over months) have shown that contact between hyphae and mineral substrates indeed lead to an increased element release via the basal surface (Bonneville et al 2009, 2011), it also became clear that the most active section of a hypha for mineral alteration is near the tip.. Thus, it is important to understand what controls hypha growth at the tip and in the mature parts of hyphae both from a biochemical but also a growth rate perspective. It is clear that the

functionality of an ectomycorrhizal fungal hypha changes with length but it is not clear if and how these changes in functionality are reflected in the biochemical composition of the hypha. To investigate these changes I have analysed live fungal hyphae to quantify relative abundances of biochemical functional groups using synchrotron based micro Fourier Transform Infrared spectroscopy (μ-FTIR).

Secondly, to refine our quantitative assessment of fungal-mineral weathering a thorough assessment of fungal growth rates are needed. This is primarily because, surprisingly, fungal growth rates are poorly known and this leads to evaluations of the rate of plant-driven fungal biotite weathering to be usually calculated based on an assumed average continuous growth rate. For example, in the fungal-biotite study of Bonneville et al (2011) a fungal growth rate of 10.2 μm d^{-1} was assumed. This value was a best estimate that was based on calculations of the time of initial colonisation and the total average hyphal length after 73 days. This rate of 10.2μm d^{-1} was at the time the first reported estimation of hyphal growth rate over any mineral surface. Fungal growth rates have been measured on few other substrates and in a few other configurations, For example, hyphal growth rates between 0 and 600 μm d^{-1} have been reported based on hyphae turnover rates in soils that range between 7 to 145 days (Staddon et al., 2003; Treseder et al., 2010). Such values render it difficult to corroborate or validate an ectomycorrhizal fungal growth rate over biotite of 10.2 μm d^{-1}. This value has to be adequately measured in time series experiments and this was one aim of this study.

In addition, through Earth history, atmospheric CO_2 has varied significantly (Berner, 2006). At a mesocosm scale, results of *Pinus sylvestris* grown in ambient (400 ppm) and elevated (1500 ppm) atmospheric CO_2 concentrations showed an enhancement of plant grown and nutrient demand at higher CO_2 (Andrews et al., 2010). If photosynthate export from plants to symbiotic fungal partners is independent of pCO_2 then it can be expected that fungal growth rates should be increased in elevated

atmospheric CO_2 concentrations. To evaluate the effect of ambient and high CO_2 on fungal growth over the same substrate was the second aim of this study.

Importantly, although rates of fungal weathering can be calculated at the scale of a single hypha (Bonneville et al., 2011), weathering occurs or is initiated primarily near the tip of a hypha. However, to translate any such derived rates to tree, field, catchment, biome, and global scales, it is important to better constrain the extent of the hypha-mineral contact surface area, and the contact area surface at the hyphal tips. This leads to the need to quantify the frequency of hyphal branching as hyphae grow across a mineral surface. In this chapter, I have used optical microscopy to monitor the growth of *Paxillus involutus,* in symbiosis with *Pinus sylvestris,* across biotite surfaces. Tree-fungi-mineral continuum microcosm system growth was observed for 5 to 10 days at 350 and 1500 ppm pCO_2, with the frequency of hyphal branching and the number of hyphal tips quantified and from these measurements fungal growth rates were derived.

Together with the biochemical measurements of fungal functional group distributions, these measurements provide further insight into the mechanisms and significance of fungal weathering at different scales and in different atmospheric conditions.

6. 2. EXPERIMENTAL METHODS

6. 2. 1. Plant-fungi axenic microcosm

The experimental approaches used below utilise the *Pinus sylvestris-Paxillus involutus* continuum microcosm setup. Surfaces of *P. sylvestris* seeds were sterilised and subsequently aseptically incubated on agar plates (for chemical composition see chapter 3, section 3.1.5) at (day) 15 °C and 60% humidity, and (night) 10 °C and 75% humidity, with an 18 hour photo period (550 μmol m^{-2} s^{1} irradiance), and at either 350 or 1500 ppm CO_2. These conditions were used for growth through the course of the microcosm

setup and experiments. At the same time *P. involutus* was grown in sterile square Petri dishes on a sheet of cellophane covering a modified Melin-Norkans agar medium (see chapter 3, section 3.1.5). After approximately 1 month, *P. sylvestris* seedlings were transferred to a Petri dish containing the *P. involutus* to form the symbiotic relationship. Tree roots were planted in contact with the growth front of the fungus, with the shoot of the tree seedling remaining outside the Petri dish through a hole sealed with lanolin.

After 8 to 10 weeks, or when evidence of mycorrhizal synthesis had occurred, seedlings with mycorrhizal roots were transferred to the experimental microcosm which consisted of 80 mL of plant agar, in a sterile square petri dish with an additional 20 mL of agar separated from the lower layer by a sterile cellophane sheet. Before the top layer of agar had solidified, 6 empty plastic wells were added at even spacing and 50 g of acid washed. Rinsed and autoclaved perlite, of 2.0 to 2.4 mm in diameter, was scattered over the agar in a single layer. The roots of the seedlings were arranged so that they did not lie over the empty plastic wells and the shoots were kept outside the sterile petri dish, through a hole sealed with lanolin. After the plants had settled in the microcosms, usually 2 weeks, the 6 empty plastic wells were replaced with wells containing single 1 cm^2 freshly cleaved biotite flakes. Experiments were run for up to 6 months, during which time the biotite flakes were colonized only by the mycorrhizal fungus. This colonisation was monitored using optical microscopy, and the biochemical composition of the hyphae analysed by μ-FTIR.

6. 2. 2. Hyphal growth observations

Images of fungal colonisation were acquired using a Nikon Eclipse ME600 microscope fitted with a Nikon CF Plan 20x extra-long working distance (ELWD) objective, a Newport motion controlled stage, and a BestScope BUC2-500C down eye-piece camera. The 20x objective yielded images with a field of view of 500 x 500 μm and

areas of the biotite surface were covered by moving the Newport motion controlled stage a known distance. The Newport motion controlled stage consisted of a Newport Universal Motion Controller ESP300 and two UTM50CC motors, facilitating movement in the *x* and *y* dimensions. This setup allowed μm precision movement of the stage, giving the ability to move know distances and return to previously visited coordinate locations. Once the fungi reached the edge of the biotite flakes composite image maps were collected at time steps ranging from 1 to 7 days for both pCO_2 systems.

Individual images from each time step were collated and stitched together manually using a standard graphics programme. Initially, images were positioned based on the recorded coordinates at the time of acquisition. Images were subsequently shifted slightly to align surface features with neighbouring images, creating a consistent image of large areas of the biotite flake surface. Fungi were located and traced using vectors which were subsequently exported to ImageJ (Rasband, 1997; Abramoff et al., 2004). Hyphal length (l) was determined using the 'measure' command, and the number of nodes (junction of branches) and tips were counted for each time step. Composites from multiple time steps were used to calculate individual and average growth rates (R) by normalising to the length of time between each composite image (t) (Eq. 6.1).

$$R = \frac{\mathrm{d}l}{\mathrm{d}t} = \frac{l_a - l_b}{t}$$

Eq. 6.1

6. 2. 3. Synchrotron based μ-FTIR

Fourier transform infrared (FTIR) spectroscopy is a technique used to determine chemical bonds in a substance and therefore give information on the chemical characteristics. Infrared light is absorbed when the vibrational motion (bending, rotation, and stretching) of a species (cation-anion pair, functional group, or molecule) causes a change in its dipole moment. The frequency and strength of infrared absorption

is determined primarily by bond type, mass of atoms, and bond symmetry (McMillan and Hofmeister; 1988; Diem, 1993; Stuart and Ando, 1997). Most organic molecules show characteristic spectral features in the mid-infrared region (700-4000cm^{-1}, Diem, 1993; Naumann et al., 1996). Table 6.1 holds information on the spectral features of organic bonds, and the compounds they correspond to typical for bacterial strands and silica substrates (Benning et al., 2004).

To perform the μ-FTIR measurements, fungal strands were initially tested on the biotite substrate (Fig 6.1). However, as fungal hyphae are very thin (<10-15 μm) the biotite silicate substrate dominated the spectral signature. Therefore we used a different

Table 6.1

Frequencies and band assignments for FTIR spectra derived from the *Calothrix* sp. Whole-cells, purified sheath spectra (adapted from Benning et al 2004).

Wavenumbers (cm^{-1})	Assignments[a]	Main group	Comment
~3300–3400	v O–H and v N–H	Water	Water/amide A
~2960	v_{as} CH_3	Lipids	Methyl groups
~2930	v_{as} CH_2	Lipids	Methylene groups
~2875	v_s >CH_2/–CH_3	Lipids	Methyl and methylene groups in fatty acids
~1740	v >C=O of esters	Membrane lipids	Fatty acids
~1710	v >C=O of esters	Carboxylic group	Esters
~1650	v C=O	Amide I	Protein (mostly *ß*-helical structure; the seconday structure of the protein can affect the position 1695–1637 cm^{-1})
~1540	δ N–H and v C–N	Amide II	Protein
~1450	δ_{as} CH_2 / δ_{as} CH_3	Lipid/amide III	Broad methylene peaks with positions varying in the literatur: amide III protein
~1392	v_s C–O	Carboxylic acids	Stretching of carboxylates: can interfere with the methyl δ_s CH_2 / δ_s CH_3 pf the proteins and with the methyl benind, δ_s $N(CH_3)_3$ of the lipids
~1240	v_{as} P=O	Nucleic acid/ phosphyoryl group	Stretching of the phosphodiester backbon of the nucleic acids (DNA and RNA); general phosphoryl groups
~1200–950	v C–O/v_{as} P=O ~1080 cm-1 for P=0 ~1165, 1110, 1050 and 1030 for C–O	Polysaccharides /nucleic acid	Dominated by the ring vibrations in polysaccharides; overlaps with stretching phophodiester backbone of the nucleic acids (DNA and RNA)
~1150–100	v C–O	Polysaccharides	Main region for carbohydrate peaks

[a] v = stretching; δ = bending; as = asymmetric, s = symmetric

approach. Immediately before measurement, live fungal hyphae were harvested from colonised biotite flakes using a pair of forceps. The removed section of mycelial network was suspended in 0.1 mL of 18 MΩ water and deposited onto a low-emissivity infrared reflectance slide (Kevley Technologies, USA), slides which show 100% reflectance across the mid-IR. μ-FTIR measurements were conducted on the MIRIAM B22 beamline at Diamond Light Source, UK, using a Bruker Vertex 80 V Fourier Transform IR Interferometer, fitted with a Hyperion 3000 microscope, using an external synchrotron source. Spectra were collected in reflectance mode with a liquid N_2 cooled mercury-cadmium-telluride (MCT) broadband detector at a resolution of 4 cm^{-1} by collating 256 or 512 scans per point through a 10 x 10 μm aperture. Point scans were collected along the length of individual hyphae with apparent tips, and nodes specifically targeted by aligning the computer controlled *x*- *y*- stage. Blank point scans of the Kevley slide were also obtained to record the background signal. Spectra from point measurements were processed using OPUS 6.5 (Bruker) to correct for background signal. Intensities of different functional groups were calculated by integrating the spectra in the region of specific peaks.

In addition to the point measurements, areas of hyphae were measured using a Focal Planar Array (FPA) mode but using a conventional globar source. A FPA is a collection of light sensitive pixels arranged into a rectangle at the focal plane of a lens. This allows the capturing of spectroscopic information over an area in a short period of time, as opposed to a composite of individual point scans from the standard setup. FPA maps scanned areas of the sample with a resolution of 1.03 μm^2/pixel with an approximate 2 fold oversampling. FPA maps were processed using the CytoSpec software to filter the spectral map for specific wavelengths.

Figure 6.1

Plant-fungi microcosm underneath the μ-FTIR objective at the MIRIAM beam line, Diamond Light Source

6. 3. RESULTS & DISCUSSION

6. 3. 1. Hyphal growth

Images of the biotite flake as a function of time show growth of hyphae (Fig. 6.2) The initial estimate of growth rate from these observations at a concentration of 1500ppm CO_2 is approximately 10 μm d^{-1}, a value comparable with that to the assumed growth rate from Bonneville et al. (2011). However, the growth rate reported by Bonneville et al. (2011) is from a plant-fungi system growing at 350 ppm atmospheric CO_2 concentration. Note the condensation of solution on the biotite surface in Fig. 6.2. It

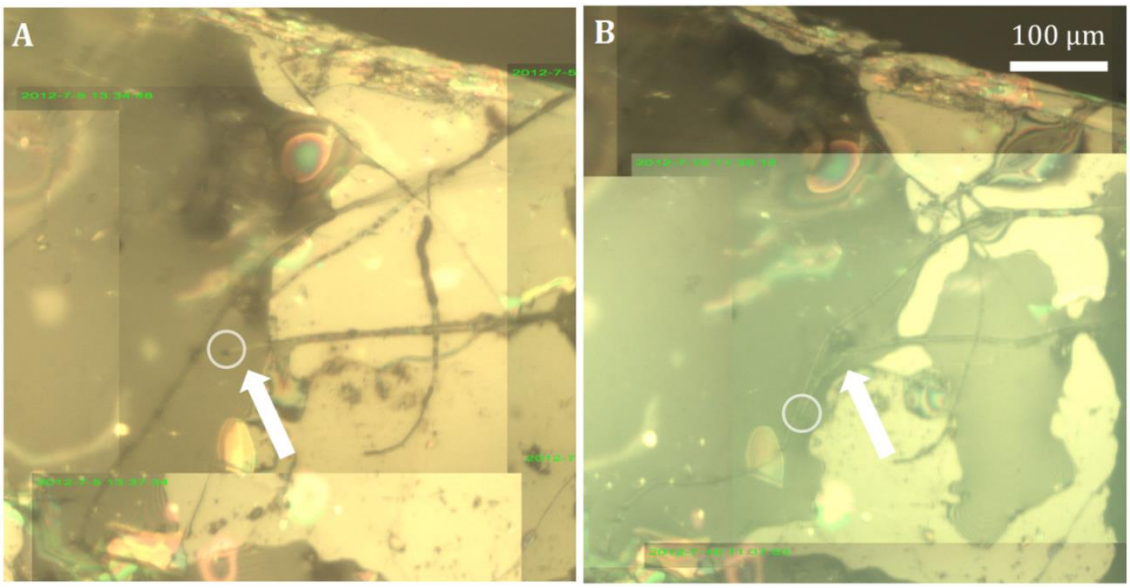

Figure 6.2

Optical microscope image of hyphae growing on a biotite surface (bright colour) at (A) time = 0, and (B) time = 5 days. The white circles are to guide the eye to the position of the hyphal tip of the highlighted hyphae. The calculated growth distance is 52 µm. The dark areas in the images are droplets of condensation forming on the biotite surface.

appears that the presence of this solution prevents the hyphae from always staying in contact with the mineral surface and in some cases the hyphae appear to 'float' on the surface of the solution droplets. It is possible that his may have a detrimental impact on hyphal growth rates and regimes.

6. 3. 2. µ-FTIR spectra and biochemical functional groups.

Point measurements along individual hyphae yield visually different spectra (Fig. 6.3). Three functional groups are clearly identified by peak assignment; lipids (blue, 2800-3050 cm^{-1}), amides (red, 1480-1700 cm^{-1}), and carbohydrates (brown, 950-1180 cm^{-1}). This initial evaluation clearly demonstrates that synchrotron based µ-FTIR is an excellent tool to assess changes in biochemical make up of growing fungal hyphae. There are clear changes in the ratios of these functional groups along the hyphae, however, further work is needed to link these changes to changes in hyphal functionality.

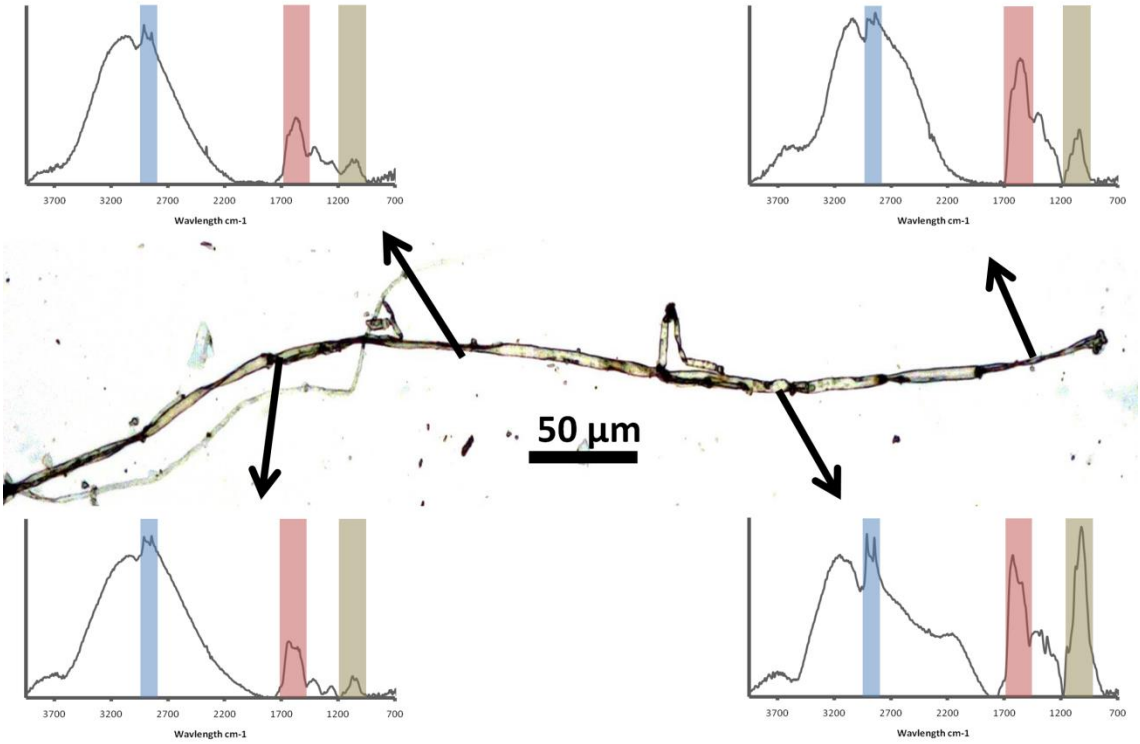

Figure 6.3

Point µ-FTIR measurements along a fungal hypha. Graphs show intensity vs wavelength (cm^{-1}) with lipids (blue, 2800-3050 cm^{-1}), amides (red, 1480-1700 cm^{-1}), and carbohydrates (brown, 950-1180 cm^{-1}) highlighted.

FPA mapping allowed the filtering of specific wavelengths across the surface map, highlighting areas of different functional groups (Fig. 6.4). These clear spatial distributions could be useful for interpreting localised functionality, for example around a growing tip.

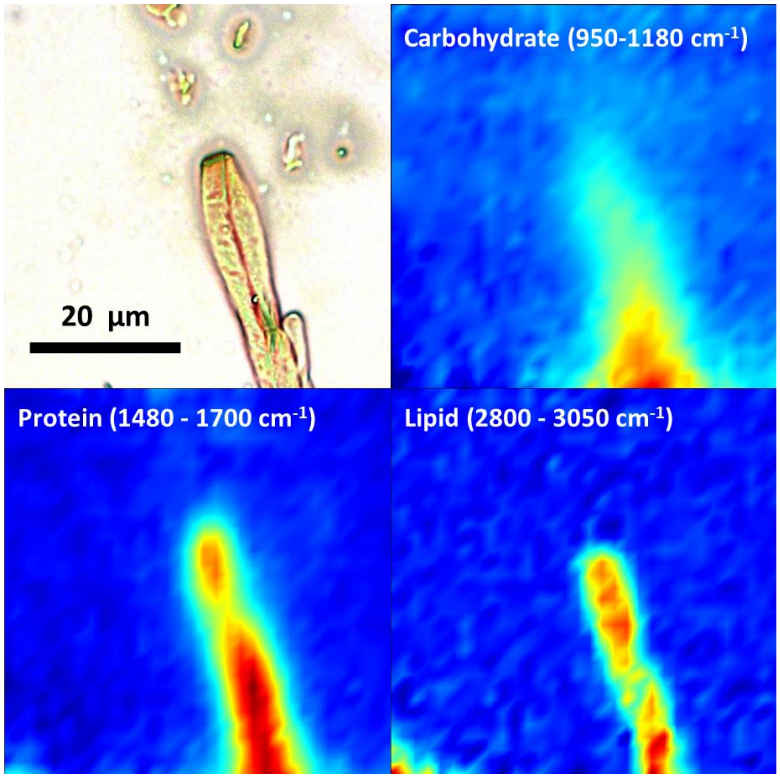

Figure 6.4

FPA maps of an area of hyphae filtered for carbohydrate, protein and lipid wavelengths.

6. 4. CONCLUSION

For the translation of lab based mycorrhizal biotite weathering rates determined at the micron scale to larger scales requires a robust understanding of the parameters controlling the weathering rate. In this case, those parameters are the growth rate and mechanism of fungal hyphae and the importance of hypha-mineral contact surface area. In this study I have shown that optical microscopy can be used to monitor fungal growth over several time steps. Initial results estimate fungal growth rates of 10 μm $^{d-1}$ in a 1500 ppm CO_2 atmosphere.

Previous studies have suggested that different areas of a fungal hypha have different functions during the fungal weathering process. In this study we hypothesise that these changes in functionality are reflected in changes in proportions of biochemical functional groups in a hypha. Initial results in this study highlight our ability identify biochemical functional groups using synchrotron based μ-FTIR and FPA mapping. However, further work is needed to marry observed changes in biochemistry to hypha functionality.

Chapter 7. Conclusions

The overarching aim of this thesis was to investigate the processes involved in fungal bio-weathering through: (i) gaining a greater understanding of mineral-fluid interface, particularly the control of fluid on the chemistry of biotite; (ii) quantifying the element release rates from biotite as a function of fluid composition; and (iii) the observation of the biochemistry and growth regime of a symbiotic fungus growing over a mineral substrate.

Minerals weather in the natural environment through both biological and abiotic processes, however the mechanisms by which a complex multi-oxide silicate, such as biotite, breaks down is poorly understood. Previous studies on a variety of biotite samples of with varying compositions have produced dissolution rates ranging over 1.5 orders of magnitude at a given pH. Both stoichiometric and non-stoichiometric biotite dissolution has been described at similar pH conditions. To understand fungal driven biotite weathering processes, there first needed to be a robust understanding the processes occurring at the biotite surface-fluid interface.

This led to the study presented in chapter 4, investigating the surface chemistry of biotite. The short time scale experiments yielded results describing an incredibly reactive mineral with a highly pH dependent and chemically variable surface composition. The results of this study gave indications of the formation of a, diffusion and surface reaction controlled dissolution front when biotite is submersed in a fluid for short periods of time.

To understand the significance of the initial dissolution processes observed in chapter 4, and to investigate the causes of the large variations in reported dissolution rates, two biotite samples, of different compositions were dissolved in acidic solutions using a combined approach of open- and closed-system experiments (Chapter 5). The effect of grain size and grain geometry was also tested to assess the importance of the different biotite surfaces (edge and basal) on bulk dissolution rate. Furthermore, as there is little data on the effect of organic ligands, at concentrations known to be secreted by microorganisms, on biotite dissolution mechanisms or rates, citric acid, oxalic acid and

DFOB were reacted with biotite. Studying the effect of organic ligands provides a link to processes which may be occurring on the mineral surface, at the interface between the fungi and the mineral.

These results provided a clearer picture of biotite dissolution mechanisms abiotically, and in the presence of organic exudates, helping our interpretation of the role of organic exudates in fungal mineral weathering.

A key aspect that current fungal mineral weathering rates lack is a quantitative understanding of how mycorrhizal hyphae grow across a mineral surface, both in terms of rate and extent. To address this I conducted some time resolved growth observations (chapter 6) to calculate the rate of growth of fungal hyphae as a function of atmospheric CO_2 concentration. As CO_2 levels have varied through geological time, this approach provides us with an estimation on how mycorrhizal may have grown millions of years ago. The quantification of growth rate, and fungi-mineral contact area is also key to calculating mineral weathering precisely. The data provided in chapter 6 aids our understanding of the importance of fungal weathering for nutrient fluxes in the environment.

It has been suggested that different areas of hyphae have different physical and chemical functions for growth and mineral weathering. The second aspect of chapter 6 was the characterisation of fungal biochemistry along the length of hyphae using synchrotron based μ-FTIR. Initial results confirmed that this μ-FTIR was a useful tool for characterising changes in biochemistry at a high resolution (5-10 μm).

The combination of these studies has led to a greater understanding of mineral weathering and the role mycorrhizal fungi play in nutrient release at a variety of scales.

7. 1. OUTLOOK

There is a clear need to investigate soil processes at a variety of scales using a multidisciplinary approach. Recent publications by teams of researchers (Brantley et al., 2011; Bridge and Banwart, 2012) have highlighted areas in which critical zone and soil science research needs to address.

For mycorrhizal mineral weathering, the work presented in this thesis, looks only at the effect of one fungus (*Paxillus involutus*) and one plan host (*Pinus sylvestris*) on one mineral, however there are a multitude mycorrhizal partnerships in the natural environment and areas of different lithology that they grow on. There is scope to understand these processes on other minerals using different species.

One of the many counter arguments to the importance of mycorrhizal fungi in mineral weathering is that they inhabit a relatively shallow area of soil. The next step in the investigation could be how communities of bacteria and fungi interact in soils to promote nutrient cycling and maintain soil health.

Chapter 8. References

Abramoff M. D., Magalhaes P. J., Ram S. J. (2004) Image Processing with ImageJ. *Biophotonicas International* **11**, 36-42.

Acker J. G. and Bricker O. P. (1992) The influence of pH on biotite dissolution and alteration kinetics at low temperature. *Geochim. Cosmochim. Acta* **56**, 3073-3092.

Adeyemi A. O. and Gadd G. M. (2005) Fungal degradation of calcium-, lead- and silicon-bearing minerals. *BioMetals* **18**, 269-281.

Akter M. and Akagi T. (2005) Effect of Fine Root Contact on Plant-Induced Weathering of Basalt. *Soil Sci. Plant Nutr.* **51**, 861-871.

Aldushin K., Jordan G., Schmahl W. W. (2006) Basal plane reactivity of phyllosilicates studied in situ by hydrothermal atomic force microscopy (HAFM). *Geochim. Cosmochim. Acta* **70** 4380-4391.

Alonso, U. (2003). Influencia de los coloides en el transporte de contaminantes en la interfaz campo cerano/campo lejano de un almacenamiento de residuos radioactivos de alta actividad. Ph.D. Thesis, Universidad Complutense de Madrid, Spain (in Spanish).

Alonso U., Missana T., Patelli A., Ceccato D., Albarran N., García-Gutiérrez M., Lopez-Torrubia T., Rigato V. (2009) Quantification of Au nanoparticles retention on a heterogeneous rock surface. *Colloid. Surface. A* **347**, 230-238.

Amrhein C. and Suarez D. L. (1988) The use of a surface complexation model to describe the kinetics of ligand-promoted dissolution of anorthite. *Geochim. Cosmochim. Acta* **52**, 2785-2793.

Amtmann A., and Rubio F. (2012) Potassium in Plants. In: eLS. John Wiley & Sons, Chichester.

Andrews M. Y., Palmer B. G., Leake J. R., Banwart S. A., Beerling D. J. (2010) Mesocosm-scale experimental quantification of plant root-fungal associations of Carbon fluxes and mineral weathering. *Geochim. Cosmochim. Acta* **74,** A24.

Arthur M. A. and Fahey T. J. (1993) Controls on Soil Solution Chemistry in a Subalpine Forest in North-Central Colorado. *Soil Sci. Soc. Am. J.* **57**, 1122-1130.

Arvieu J.-C., Leprince F., Plassard C. (2003) Release of oxalate and protons by ectomycorrhizal fungi in response to P-deficiency and calcium carbonate in nutrient solution. *Ann. For. Sci.* **60**, 815-821.

Balland C., Poszwa A., Leyval C. and Mustin C. (2010) Dissolution rates of phyllosilicates as a function of bacterial metabolic diversity. *Geochim. Cosmochim. Acta* **74**, 5478-5493.

Balogh-Brunstad Z., Keller C. K., Gill R. A. (2008a) The effect of bacteria and fungi on chemical weathering and chemical denudation fluxes in pine growth experiments. *Biogeochemistry* **88**, 153-167.

Balogh-Brunstad Z., Keller C. K., Dickinson J. T., Stevens F., Li C. Y., Bormann B. T. (2008b) Biotite weathering and nutrient uptake by ectomycorrhizal fungus, *Sillus tomentosus*, in liquid-culture experiments.

Banwart S. A. (2011) Save our soils. *Nature* **474**, 151-152.

Barman A. K., Varadachari C., Ghosh K. (1992) Weathering of solicate minerals by organic acids I. Nature of cation solubilisation. *Geoderma* **53**, 45-63.

Bartnicki-Garcia S., Bracker C. E., Gierz G., Lopez-Franco R., Lu H. S. (2000) Mapping the growth of fungal hyphaeL Orthogonal cell wall expansion during tip growth and the role of turgor. *Biophys. J.* **79**, 2382-2390.

Bastmeyer M., Deising H. B., Bechinger C. (2002) Force exertion in fungal infection. *Annu. Rev. Biophys. Biom.* **31**, 321–341

Bechinger C., Giebel K.-F., Schnell,M., Leiderer P., Deising H. B., Bastmeyer M. (1999) Optical measurements of invasive forces exerted by appressoria of a plant pathogenic fungus: *Science* **285**, 1896–1899.

Beerling D. J. and Berner R. A. (Feedbacks and the coevolution of plants and atmospheric CO_2. *PNAS* **102**, 1302-1305.

Benning L. G., Phoenix V. R., Yee N., Tobin M. J. (2004) Molecular characterization of cyanobacterial silicification using cynchrotron infrared micro-spectroscopy. *Geochim. Cosmochim. Acta* **68** 729–741.

Bergeron R. J. and McManis J. S. (1991) Synthesis of catecholamide and hydroxamate siderophores. In *CRC Handbook of microbial iron chelates* (ed. Winkelmann, G.), CRC Press, Florida,

Berner E. K., Berner R. A., Moulton K. L. (2003) Plants and Mineral Weathering: Present and Past. 169-188. In *Surface and Ground Water, Weathering, and Soils* (ed. J. I. Dever) Vol. 5 *Treatise on Geochemistry* (eds. H. D. Holland and K. K. Turekian), Elsevier-Pergamon, Oxford.

Berner R. A. (2006) GEOCARBSULF: A combined model for Phanerozoic atmospheric O2 and CO2. *Geochim. Cosmochim. Acta* **70**, 5653-5664.

Bickmore B. R., Bosbach D., Hochella M. F., Charlet L., Rufe E. (2001) In situ atomic force microscopy study of hectorite and nontronite dissolution: Implications for phyllosilicate edge surface structures and dissolution mechanisms. *Am. Miner.* **86**, 411-423.

Bickmore B. R., Rosso K. M., Nagy K. L., Cygan R. T., Tadanier C. J. (2003) *Ab initio* determination of edge surface structures for dioctahedral 2:1 phyllosilicates: implications for acid-base reactivity. *Clay Clay Miner.* **51**, 359-371.

Blum A. and Lasaga A. C. (1991) The role of surface speciation in the dissolution of albite. *Geochim. Cosmochim. Acta* **55**, 2193-2201.

Bonneville S., Smits M. M., Brown A., Harrington J., Leake J.R., Brydson R. and Benning L. G. (2009) Plant-driven fungal weathering: early stages of mineral alteration at the nanometer scale. *Geology* **37**, 615-618.

Bonneville S., Morgan D. J., Schmalenberger A., Bray A., Brown A., Banwart S. A. and Benning L. G. (2011) Tree-mycorrhiza symbiosis accelerate mineral weathering: Evidences from nanometer-scale elemental fluxes at the hypha-mineral interface. *Geochim. Cosmochim. Acta* **75**, 6988-7005.

Borgias B., Hugi A. D., Raymond K. N. (1989) Isomerization and Solution Structures of Desferrioxamine B Complexes of Al^{3+} and Ga^{3+}. *Inorg. Chem.* **28**, 3538-3545.

Bormann B. T., Wang D., Bormann F. H., Benoit G., April R., Snyder M. C. (1998) Rapid, plant-induced weathering in an aggrading experimental ecosystem. *Biogeochemistry* **43**, 129-155.

Bosbach D., Charlet L., Bickmore B., Hochella M. F. Jr. (2000) The dissolution of hectorite: In-situ, real-time observations using atomic force microscopy. Am. Min. **85**, 1209-1216.

Bowser C. J., and Jones B. F. (2002) Mineralogic controls on the composition of natural waters dominated by silicate hydrolysis. *Am. J. Sci.* **302**, 582-662.

Brady P. V. and Walther J. V. (1990) Kinetics of quartz dissolution at low temperatures. *Chem. Geol.* **82**, 253-264.

Brandt F., Bosbach D., Krawczyk-Bärsch E., Arnold T. and Bernhard G. (2003) Chlorite dissolution in the acid pH-range: A combined microscopic and macroscopic approach. *Geochim. Cosmochim. Acta* **67**, 1451–1461.

Brantley S. L., Liermann L., Bau M., Wu S. (2001) Uptake of Trace Metals and Rare Earth Elemnts from Hornblende by a Soil Bacterium. *Geomicrobiol. J.* **18**, 37-61.

Brantley S. L. (2003) Reaction Kinetics of Primary Rock-forming Minerals under Ambient Conditions, pp. 73-118. In *Surface and Ground Water, Weathering, and Soils* (ed. J. I. Dever) Vol. 5 *Treatise on Geochemistry* (eds. H. D. Holland and K. K. Turekian), Elsevier-Pergamon, Oxford.

Brantley S. L., Megonigal J. P., Scatena F. N., Balogh-Brunstad Z., Barnes R. T., Bruns M. A., Van Cappellen P., Dontsova K., Hartnett H. E., Hartshorn A. S., Heimsath A., Herndon E., Jin L., Keller C. K., Leake J. R., McDowell W. H., Meinzer F. C., Mozdzer T. J., Petsch S., Pett-Ridge J., Pregitzer K. S., Raymond P. A., Riebe C. S., Shumaker K., Sutton-Grier A., Walter R. and Yoo K. (2011) Twelve testable hypotheses on the geobiology of weathering. *Geobiology* **9**, 140–165.

Bray A. W., Benning L. G., Bonneville S., Oelkers E. H. (2014) Biotite surface chemistry as a function of aqueous fluid composition. *Geochim. Cosmochim. Acta* **128**, 58-70.

Bridge J. and Banwart S. A. (2012) Securing soils for sustainable agriculture. *Royal Society of Chemistry*. Available from: http://www.rsc.org/images/081203%20oscar%20web_tcm18-222767.pdf

Brigatti F. M., Frigieri P., Ghezzo C. and Poppi L. (2000) Crystal chemistry of Al-rich biotites coexisting with muscovites in peraluminous granites. *Am. Mineral.* **85**, 436-448.

Brown, G. E., and Calas, G. (2012) Mineral-aqueous solution interfaces and their impact on the environment. *Geochem. Perspectives,* **1,** 483-742.

Brunauer S., Emmett P, H., Teller E. (1938) Adsorption of Gases in Multimolecular Layers. *J. Am. Chem. Soc.* **60**, 309-319.

Bundeleva I. A., Shiokova L. S., Bénézeth P., Pokrovsky O. S., Kompantseva E. I., Balor S. (2011) Zeta potential of anoxygenic phototrophic bacteria and Ca adsorption at the cell surface: Possible implications for cell protection from $CaCO_3$ precipitation in alkaline solutions. *J. Colloid. Interf. Sci.* **360,** 100-109.

Buss H. L., Lüttge A., Brantley S. L. (2007) Etch pit formation on iron silicate surfaces during siderophore-promoted dissolution. *Chem. Geol.* **240**, 326-342.

Cama J. and Ganor J. (2006) The effects of organic acids on the dissolution of silicate minerals: A case study of oxalate catalysis of kaolinite dissolution. *Geochim. Cosmochim. Acta* **70**, 2191-2209.

Cappelli C., Van Driessche A. E. S., Cama J., Huertas F. J. (2013) In Situ Observation of Biotite Dissolution at pH 1 Using Advanced Optical Microscopy. *Cryst. Growth Des.* **13**, 2880-2886.

Carroll S. A and Knauss K. G. (2005) Dependence of labradorite dissolution kinetics on $CO_{2(aq)}$ and $Al_{(aq)}$ and temperature. *Chem. Geol.* **217**, 213-225.

Cases J. (1967) Les phenomenes physicochimiques a l'interface application au procede de la flottation. PhD thesis, Faculte des Sciences de L'Universite de Nancy.

Chaïrat C., Oelkers, E. H., Schott J., Lartigue J.-E. (2007) Fluorapatite surface composition in aqueous solution deduced from potentiometric, electrokinetic, and solubility measurements, and spectroscopic observations. *Geochim. Cosmochim. Acta* **71**, 5888-5900.

Cheah S.-F., Kraemer S. M., Cervini-Silva J., Sposito G. (2003) *Chem. Geol.* **198**, 63-75.

Cocozza C., Tsao C. C. G., Cheah S.-F., Kraemer S. M., Raymond K. N., Miano T. M., Sposito G. (2002) Temperature dependence of goethite dissolution promoted by trihydroxamate siderophores. *Geochim. Cosmochim. Acta* **66**, 431-438.

Coradin T., Eglin D., Livage J. (2004) The silicomolybdic acid spectrophotometric method and its application to silicate/biopolymer interaction studies. *Spectroscopy* **18,** 567-576.

Cornejo-Garrido H., Fernández-Lomelín P., Guzmán J., Cervini-Silva J. (2008) Dissolution of arsenopyrite (FeAsS) and galena (PbS) in the presence of desferrioxamine-B at pH 5. *Geochim. Cosmochim. Acta* **72**, 2754-2766.

Davies C. W. (1962) Ion Association. Butterworths, London. 37–53.

Davis J. A. and Kent D. B. (1990) Surface complexation modelling in aqueous geochemistry. *Rev. Min*. **23**, 117–260.

Declerq J., Bosc O., Oelkers E. H., (2013) Do organic ligands affect forsterite dissolution rates? *Appl. Geochem.* **39**, 69-77.

Deer W. A., Howie R. A., Zussman J. (1966) An Introduction to the Rock Forming Minerals. 193-216. Longman Group Limited, Essex, United Kingdom.

Devidal J.-L., Schott J. and Dandurand J.-L. (1997) An experimental study of kaolinite dissolution and precipitation kinetics as a function of chemical affinity and solution composition at 150 ^{o}C, 40 bars, and pH 2, 6.8 and 7.8. *Geochim. Cosmochim. Acta* **61**, 5165-5186.

Diem M. (1993) Introduction to Modern Vibrational Spectrscopy. Wiley Interscience, New York.

Drever J. I. (1994) The effect of land plants on weathering rates of silicate minerals. *Geochim. Cosmochim. Acta* **58**, 2325–2332.

Drever J. I. (1997) The Geochemistry of Natural Waters, 3rd ed. Prentice-Hall, New Jersey, 436.

Drever J. I. and Stillings L. L. (1997) The role of organic acids in mineral weathering. *Colloid. Surface.* **120**, 167-181.

Drever J. I. and Zobrist J. (1992) Chemical weathering of solicate rocks as a function of elevation in the southern Swiss Alps. *Geochim. Cosmochim. Acta* **56**, 3209-3216.

Eaton A., Clesceri L., Greenber A., Franson M. (2005) Standard methods for the examination of water and wastewater. **4** 164-171. American Public Health Association, Washington, DC.

Ek H., (1997) The influence of nitrogen fertilization on the carbon economy of *Paxillus involutus* in ectomycorrhizal association with *Betula pendula*. *New Phytol*. **135**, 133–142.

Filby A., Plaschke M., Geckeis H., Fanghänel Th. (2008) Interaction of latex colloids with mineral surfaces and Grimsel granodiorite. *J. Contam. Hyrdol.* **102**, 273-284.

Föllmi K. B., Arn K., Hosein R., Adatte T., Steinmann P. (2009) Biogeochemical weathering in sedimentary chronosequences of the Rhône and Oberaar Glaciers (Swiss Alps): Rates and mechanisms of biotite weathering. *Geoderma* **151**, 270-281.

Furrer G. and Stumm W. (1986) The coordination chemistry of weathering: dissolution kinetics of Al_2O_3 and BeO. *Geochim. Cosmochim. Acta* **50**, 1847-1860.

Gadd G. M. (2007) Geomycology: biogeochemical transformations of rocks, minerals, metals and radionuclides by fungi, bioweathering and bioremediation. *Mycol. Res.* **111**, 3-49.

Gautier J.-M., Oelkers E. H. and Schott J. (1994) Experimental study of K-feldspar dissolution rates as a function of chemical affinity at 150 °C and pH 9. *Geochim. Cosmochim. Acta* **58**, 4549-4560.

Gazzè S. A., Saccone L., Ragnarsdottir K. V., Smits M. M., Duran A. L., Leake J. R., Banwart S. A., McMaster T. J. (2012) Nanoscale channels on ectomycorrhizal-colonized chlorite: Evidence for plant-driven fungal dissolution. *J. Geophys. Res*. **117**, G00N09.

Gazzè S. A., Saccone L., Smits M. M., Duran A. L., Leake J. R., Banwart S. A., Ragnasdóttir K. V., McMaster T. J. (2013) Nanoscale Observations of Extracellular Polymeric Substances Deposition on Phyllosilicates by an Ectomycorrhizal Fungus, *Geomicrobiol. J.* **30**, 721-730.

Gazzè S. A., Stack A. G., Ragnasdóttir K. V., McMaster T. J. (2014) Chlorite topography and dissolution of the interlayer studied with atomic force microscopy. *Am. Min.* **99**, 128-138.

Gislason S. R. and Oelkers E. H. (2003) The mechanism, rates and consequences of basaltic glass dissolution: II. An experimental study of the dissolution rates of basaltic glass as a function of pH at temperatures from 6 ˚C to 150 ˚C. *Geochim. Cosmochim. Acta* **67**, 3817-3832.

Golubev S. V., Bauer A., Pokrovsky O. S. (2006a) Effect of pH and organic ligands on the kinetics of smectite dissolution at 25ºC. *Geochim. Cosmochim. Acta* **70**, 4436-4451.

Golubev S. V., and Pokrovksy O. S. (2006b) Experimental study of the effect of organic ligands on diopside dissolution kinetics. *Chem. Geol.* **235**, 377-389.

Gooday G. W. (1996) Cell walls. In *The Growing Fungus* (ed. Gow N. A. R. and Gadd G. M.) Chapman and Hall, London.

Grąz M. and Wilkołazka A. J. (2009) *Abortiporus biennis* tolerance to insoluble metal oxides: oxalate secretion, oxalate oxidase activity, and mycelial morphology. *BioMetals* **22**, 401-410.

Harold F.M. (2002) Force and compliance: Rethinking morphogenesis in walled cells: *Fungal Genetics and Biology* **37**, 271–282

Harouiya N. and Oelkers E. H. (2004) An experimental study of the effect of aqueous fluoride on quartz and alkali-feldspar dissolution rates. *Chem. Geol.* **205**, 155-167.

Haward S. J., Smits M. M., Ragnasdóttir K. V., Leake J. R., Banwart S. A., McMaster T. J. (2011) In situ atomic force microscopy measurements of biotite basal plane reactivity in the presence of oxalic acid. *Geochim. Cosmochim. Acta* **75**, 6870-6881.

He Y. T., Bigham J. M., Traina S. J. (2005) Biotite dissolution and Cr(VI) reduction at elevated pH and ionic strength. *Geochim. Cosmochim. Acta* **69**, 3791-3800.

Hersman L., Lloyd T., Sposito G. (1995) Siderophore-promoted dissolution of hematite. *Geochim. Cosmochim. Acta* **59**, 3327-3330.

Hobbie E. A. and Wallander H. (2006) Integrating ectomycorrhizal fungi into quantitative frameworks of forest carbon and nitrogen cycling. In *Fungi in Biogeochemical Cycles* (ed. G. M. Gadd). Cambridge University Press, Cambridge, 98–128.

Hodson M. E. (2006) Does reactive surface area depend on grain size? Results from pH 3, 25 °C far-from-equilibrium flow-through experiments on anorthite and biotite. *Geochim. Cosmochim. Acta* **70**, 1655-1667.

Högberg M. N. and Högberg P. (2002) Extramatrical ectomycorrhizal mycelium contributes one-third of microbial biomass and produces, together with associated roots, half the dissolved organic carbon in a forest soil. *New. Phytol.* **154**, 791-795.

Holmén B. A. and Casey W. H., (1996) Hydroxamate ligands, surface chemistry, and the mechanism of ligand-promoted dissolution of goethite [α-FeOOH(s)]. *Geochim. Cosmochim. Acta* **60**, 4403-4416.

Hopf J., Langenhorst F., Pollok K., Merten D., Kothe E. (2009) Influence of microorganisms on biotite dissolution: An experimental approach. *Chem. Erde-Geochem.* **69**, 45-56.

Huang W. H. and Kiang W. C. (1972) Laboratory dissolution of plagioclase feldspars in water and organic acids at room temperature. *Am. Min.* **57**, 1849-1859.

Hunter R. J. (1989) Foundation of Colloid Science. **Vol. 1**, Clarendon Press, Oxford.

IUPAC (2006) Compendium of Chemical Terminology, the Gold Book. <http://goldbook.iupac.org/>

James R. O. and Healy T. W. (1972) Adsorption of hydrolysable metal-ions at oxide water interface. 1. Co(II) adsorption on SiO_2 and TiO_2 as model systems. *J. coll. Inter Sci.* **40**, 42-52.

Jara A. A., Golberg S. and Mora M. L. (2005) Studies on the surface charge of amorphous aluminosilicates using surface complexation models. *J. Colloid Interf. Sci.* **292**, 160-170

Jenny H. (1941) Factors of Soil Formation. *McGraw-Hill Book Company*, New York.

Jones D. L. (1998) Organic acids in the rhizosphere – a critical review. *Plant and Soil* **205**, 25-44.

Jongmans A. G., van Breemen N., Lundstrom U., van Hees P. A. W., Finlay R. D., Srinivasan M., Unestam T., Giesler R., Melkerud P. A. and Olsson M. (1997) Rock-eating fungi. *Nature* **389**, 682–683.

Kalinowski B. E. and Schweda P. (1996) Kinetics of muscovite, phlogopite and biotite dissolution and alteration at pH 1-4, room temperature. *Geochim. Cosmochim. Acta* **60**, 367-385.

Kalinowski B. E., Lierman L. J., Brantley S. L., Barnes A., Pantano C. G. (2000) X-ray photoelectron evidence for bacteria-enhanced dissolution of hornblende. *Geochim. Cosmochim. Acta* **64**, 1331-1343.

Kaviratna H., Pinnavaia T. J. (1994) Acid hydrolysis of octahedral Mg^{2+} sites in 2:1 layered silicates: an assessment of edge attack and gallery access mechanisms. *Clay Clay Miner.* **42**, 717-723.

Kiczka M., Wiederhold J. G., Frommer J., Kraemer S. M., Bourdon B., Kretzschmar R. (2010) Iron isotope fractionation during proton- and ligand-promoted dissolution of primary phyllosilicates. *Geochim. Cosmochim. Acta* **74**, 3112-3128.

Koele N., Turpault M.-P., Hildebrand E. E., Uroz S., Frey-Klett P. (2009) Interactions between mycorrhizal fungi and mycorrhizosphere bacteria during mineral weathering: Budget analysis and bacterial quantification. *Soil Biol. Biochem.* **41**, 1935-1942.

Köhler S. J., Bosbach D., Oelkers E. H. (2005) Do clay mineral dissolution rates reach steady state? *Geochim. Cosmochim. Acta* **69**, 1997-2006.

Kosmulski M. (2009) Compilation of PZC and IEP of sparingly soluble metal oxides and hydroxides from literature. *Advances in Colloid and Interface Science* **152**, 14-25.

Kraemer S. M., Cheah S.-F., Zapf R., Xu J., Raymond K. N., Sposito G. (1999) Effect of hydroxamate siderophores on Fe release and Pb(II) adsorption by goethite. *Geochim. Cosmochim. Acta* **63**, 3003-3008.

Kraemer S. M. (2004) Iron oxide dissolution and solubility in the presence of siderophores. *Aquat. Sci.* **66**, 3-18.

Kubicki J. D., Blake G. A., Apitz S. E. (1997) Molecular orbital calculations for modelling acetate-aluminosilicate adsorption and dissolution reactions. *Geochim. Cosmochim. Acta* **61**, 1031-1046.

Landeweert R., Hoffland E., Finlay R. D., Kuyper T. W., van Breemen N. (2001) Linking plants to rocks: ectomycorrhizal fungi mobilize nutrients from minerals. *TRENDS Ecol. Evol.* **16**, 248–254.

Lapeyrie F., Chilvers G. A., Bhem C. A. (1986) Oxalic acid synthesis by the mycorrhizal fungus *Paxillus involutus* (Batsch. ex Fr.) Fr. *New Phytol.* **106**, 139-146.

Lasaga A. C. (1998) Kinetic Theory in the Earth Sciences. *Princeton University Press*, NJ.

Lasaga A. C., Soler J. M., Ganor J., Burch T. E., Nagy K. L. (1994) Chemical weathering rate laws and global geochemical cycles. *Geochem. Cosmochem. Acta* **58**, 2362-2386.

Leake J. R., Duran A. L., Hardy K. E., Johnson I., Beerling D. J., Banwart S. A., Smits M. M. (2008) Biological weathering in soil: the role of symbiotic root-associated fungi biosensing minerals and directing photosynthate-energy into grain-scale mineral weathering. *Min. Mag.* **72**, 85-89.

Leyval C. and Berthelin J. (1991) Weathering of a Mica by Roots and Rhizospheric Microorganisms of Pine. *Soil Sci. Soc. Am. J.* **55**, 1009-1016.

Lian B., Chen Y., Zhu L. and Yang R. (2008) Effect of Microbial Weathering on Carbonate Rocks. *Earth Sci. Front.* **15**, 90-99.

Lin F. -C. and Clemency C. V. (1981a) Dissolution kinetics of phlogopite. I. Closed system. *Clays Clay Minerals* **29**, 101-106.

Lin F. -C. and Clemency C. V. (1981b) The kinetics of dissolution of muscovites at 25˚C and 1 atm CO_2 partial pressure. *Geochim. Cosmochim. Acta* **45**, 571-576.

Loring J. S., Simanova A. A., Persson P. (2008) Highly Mobile Iron Pool from a Dissolution-Readsorption Process. *Langmuir* **24**, 7054-7057.

Malmström M., Banwart S., Lewenhagen J., Duro L. and Bruno J. (1996) The dissolution of biotite and chlorite at 25˚C in the near-neutral pH region. *J. Cont. Hydrol.* **21**, 201-213.

Malmström M. and Banwart S. (1997) Biotite dissolution at 25˚C: The pH dependence of dissolution rate and stoichiometry. *Geochim. Cosmochim. Acta* **61**, 2779-2799.

Martell A. E. and Smith R. M. (1977) Critical Stability Constants: Volume 3 Other Organic Ligands. Springer, New York.

Martell A. E., Smith R. M., Motekaitis R. J. (2004) NIST critically selected stability constants, stability constants, standard reference database 46, Version 8.0.

McMaster T. J., Smits M. M., Haward S. J., Leake J. R., Banwart S., Ragnarsdóttir K. V. (2008) High-resolution imaging of biotite dissolution and measurement of activation energy. *Min. Mag.* **72**, 115-120.

McMaster T. J. (2012) Atomic Force Microscopy of the fungi-mineral interface applications in mineral dissolution, weathering and biogeochemistry. *Curr. Opin. Biotech.* **23**, 562-569.

McMillan P. F. and Hofmeister A. M. (1988) Infrared and Raman spectroscopy. *In Rev. Mineral.* **18,** 99–160.

Momma K. and Izumi F. (2011) VESTA 3 for three-dimensional visualization of crystal, volumetric and morphology data. *J. Appl. Crystallogr.* **44**, 1272-1276.

Money P.N. (1999) Fungus punches its way in. *Science* **201**, 332–333.

Morel F. M .M., and Hering J. G. (1993) *Principles and Applications of Aquatic Chemistry.* Wiley, New York.

Moulton K. L. and Berner R. A. (1998) Quantification of the effect of plants on weathering: Studies in Iceland. *Geology* **26**, 895-898.

Murakami T., Utsunomiya S., Yokoyama T., Kasama T. (2003) Biotite dissolution processes and mechanisms in the laboratory and in nature: Early stage weathering environment and vermiculitization. *Am. Min.* **88**, 377-386.

Murakami T., Ito J.-I., Utsunomiya S., Kasama T., Kozai N., Ohnuki T. (2004) Anoxic dissolution processes of biotite: implications for Fe behaviour during Archean weathering. *Earth Planet Sc. Lett.* **224**, 117-129.

Murphy S. F., Brantley S. L., Blum A. E., White A. F., Dong H. (1998) Chemical weathering in a tropical watershed, Luquillo Mountains, Puerto Rico: II. Rate and mechanism of biotite weathering. *Geochim. Cosmochim. Acta* **62**, 227-243.

Nagy K. L. (1995) Dissolution and precipitation kinetics of sheet silicates. *Rev. Mineral.* **31**, 173-233.

Naumann D., Schultz C., and Helm D. (1996) What can infrared spectroscopy tell us about the structure and composition of intact bacterial cells? In *Infrared Spectroscopy of Biomolecules* (eds. H. H. Mantsch and D. Chapman), pp. 279–310. Wiley-Liss, New York.

Neaman A., Chorover J., Brantley S. L. (2006) Effects of organic ligands on granite dissolution in batch experiments at pH 6. *Am. J. Sci.* **306**, 451-473.

Nesbitt H. W. and Young G. M. (1984) Prediction of some weathering trends of plutonic and volcanic rocks based on thermodynamic and kinetic considerations. *Geochim. Cosmochim. Acta* **48**, 1523-1534.

Oelkers E. H., Schott J. and Devidal J.-L. (1994) The effect of aluminium, pH, and chemical affinity on the rates of aluminosilicate dissolution reactions. *Geochim. Cosmochim. Acta* **58**, 661-669.

Oelkers E. H., (1996) Summary and review of the physical and chemical properties of rocks and fluids. *Rev. Min.* **34**, 131-191.

Oelkers E. H. and Schott J. (2001) An experimental study of enstatite dissolution rates as a function of pH, temperature, and aqueous Mg and Si concentration, and the mechanism of pyroxene/pyroxenoid dissolution. *Geochim. Cosmochim. Acta* **65**, 1219-1231.

Oelkers E. H., Schott J., Devidal, J.-L. (2001) On the interpretation of closed system mineral dissolution experiments: Comment on "Mechanism of keolinit dissolution at room temperature and pressure Part II: Kinetic study" by Huertas et al. (1999). *Geochim. Cosmochim. Acta* **65**, 4429-4432.

Oelkers E. H., Golubev S. V., Chaïrat C., Pokrovsky O. S., Schott J. (2009) The surface chemistry of multi-oxide silicates. *Geochim. Cosmochim. Acta* **73**, 4617-4634.

Parkhurst D. L., and Appelo C. A. J., (2013) PHREEQC version 3 – A computer program for speciation, batch-reaction, one-dimensional transport, and inverse geochemical calculations. Available from: <http://wwwbrr.cr.usgs.gov/projects/GWC_coupled/phreeqc/>.

Parks G. A. (1965) Isoelectric points of solid oxides and aqueous hydroxo complex systems. *Chem. Revs.* **65**, 177-244.

Parks G. A. (1967) Aqurous surface chemistry of oxides and complex oxide minerals. In Equilibrium Concepts in Natural Water Systems (ed. W. Stumm). *Am. Chem. Soc. Adv. Chem.* **67**, 121-160.

Parks G. A. (1990) Surface Energy and Adsorption at Mineral /Water Interfaces: An Introduction. *Rev. Min*. **23**, 133-175.

Pimentel D., Harvey C., Resosudarmo P., Sinclair K., Kurz D., McNair M., Crist S., Shpritz L., Fitton L., Saffouri R., Blair R. (1995) Environmental and Economic Costs of Soil Erosion and Conservation Benefits. *Science* **267**, 1117-1123.

Planquette H., Fones G. R., Statham P. J., Morris P. J. (2009) Origin of iron and aluminium in large particles (> 53 μm) in the Crozet region, Southern Ocean. *Marine Chemistry* **115**, 31-42.

Pokrovski G. S. and Schott J. (1998) Experimental study of the complexation of silicon and germanium with aqueous organic species: Implications for germanium and silicon transport and Ge/Si ratio in natural waters. *Geochm. Cosmochim. Acta* **62**, 3413-3428.

Pokrovsky O. S., Schott J. and Thomas F. (1999) Dolomite surface speciation and reactivity in aquatic systems. *Geochim. Cosmochim, Acta* **63**, 3133-3143.

Pokrovsky O. S. and Schott J. (2000) Forsterite surface composition in aqueous solutions: a combined potentiometric, electrokinetic, and speciation approach. *Geochim. Cosmochim Acta* **64**, 3299-3312.

Pokrovsky O. S. and Schott J. (2004) Experimental study of brucite dissolution and precipitation in aqueous solution: surface speciation and chemical affinity control. *Geochim. Cosmochim. Acta* **68**, 31-45.

Pokrovsky O. S., Shirokova L. S., Bénézeth P., Schott J. (2009) Effect of organic ligands and heterotrophic bacteria on wollastonite dissolution kinetics. *Am. J. Sci.* **309**, 731-772.

Quirk J., Beerling D. J., Banwart S. A., Kakonyi G., Romero-Gonzalez M. E., Leake J. R. (2012) Evolution of trees and mycorrhizal fungi intensifies silicate mineral weathering. *Biology Letters* **8**, 1006-1011.

Quirk J., Leake J. R., Banwart S. A., Taylor L. L., Beerling D. J. (2014) Weathering by tree-root-associating fungi diminishes under simulated Cenozoic atmospheric CO_2 decline. *Biogeosciences* **11**, 321-331.

Ramos M. E., Cappelli C., Rozalén M., Fiore S., Huertas F. J., Effect of lactate, glycine, and citrate on the kinetics of montmorillonite dissolution. *Am. Min.* **96**, 768-780.

Rasband W. S., (1997) ImageJ, U. S. National Institutes of Health, Bethesda Maryland, USA. Available from: http://imagej.nih.gov/ij/.

Rath R. K. and Subramanian S. (1997) Studies on adsorption of guar gum onto biotite mica. *Miner. Eng.* **10**, 1405-1420.

Read D. J., Leake J. R., Perez-Moreno J. (2004) Mycorrhizal fungi as drivers of ecosystem processes in heathland and boreal forest biomes. *Can. J. Bot.* **82**, 1243-1263.

Reichard P. U., Kretzschmar R., Kraemer S. M. (2007) Dissolution mechanisms of goethite in the presence of siderophores and organic acids. *Geochim. Cosmochim. Acta* **71**, 5635-5650.

Read D. J., Leake J. R., Perez-Moreno J. (2004) Mycorrhizal fungi as drivers of ecosystem processes in heathland and boreal forest biomes. *Can. J. Bot.* **82**, 1243-1263.

Renshaw J. C., Robinson G. D., Trinci A. P. J., Wiebe M. G., Livens F. R., Collison D., Taylor R. J. (2002) Fungal siderophores: structures, functions and applications. *Mycol. Res.* **106**, 1123-1142.

Rimstidt J. D. (2014) Geochemical Rate Models. *Cambridge University Press*. Cambridge, UK.

Rosenberg D. R. and Maurice P. A. (2003) Siderophore adsorption to and dissolution of kaolinite at pH 3 to 7 and 22 °C. *Geochim. Cosmochim. Acta.* **67**, 223-229.

Rufe E. and Hochella Jr. M. F. (1999) Quantitative Assessment of Reactive Surface Area of Phlogopite During Acid Dissolution. *Science* **285**, 874–876.

Rutherford G. K. and Bray C. (1979) Extent and Distribution of Soil Heavy Metal Contamination near a Nickel Smelter at Coniston, Ontario. *J. Environ. Qual.* **8**, 219-222.

Saccone L., Gazzè S. A., Duran A. L., Leake J. R., Banwart S. A., Ragnarsdóttir K. V., Smits M. M., McMaster T. J. (2012) High resolution characterization of ectomycorrhizal fungal-mineral interactions in axenic microcosm experiments. *Biogeochemistry* **111**, 411-425.

Saha R., Saha N., Donofrio R. S., Bestervelt L. L. (2012) Microbial siderophores: a mini review. *J. Basic Microb.* **53**, 303-317

Saldi G. D., Köhler S. J., Marty N., Oelkers E. H. (2007) Dissolution rates of talc as a function of solution composition, pH and temperature. *Geochim. Cosmochim. Acta* **71**, 3446-3457.

Schnoor J. L. (1990) Kinetics of chemical weathering: a comparison of laboraty and field weathering rates. In *Aquatic Chemical Kinetics* (ed. W. Stumm). Wiley, New York.

Schott J., Pokrovsky O. S., Spalla O., Devreux F., Gloter A., Mielczarski J. A. (2012) Formation, growth and transformation of leached layers during silicate minerals dissolution: The example of wollastonite. *Geochim. Cosmochim. Acta* **98**, 259-281.

Simanova A. A., Persson P., Loring J. S. (2010) Evidence for ligand hydrolysis and Fe(III) reduction in the dissolution of goethite by desferriozamine-B. *Geochim. Cosmochim. Acta* **74**, 6706-6720.

Smits M. M., Bonneville S., Haward S., Leake J. R. (2008) Ectomycorrhizal weathering, a matter of scale? Min. Mag. 72, 131-134.

Smits M. M., Bonneville S., Benning L. G., Banwart S. A. and Leake J. R. (2012) Plant-driven weathering of apatite – the role of an ectomycorrhizal fungus. *Geobiology* **10**, 445-456.

Song W., Ogawa N., Oguchi C. T., Hatta T., Matsukara Y. (2007) Effect of Bacillus subtilis on granite weathering: A laboratory experiment. Catena 70, 275-281.

Sposito G. (1984) The surface chemistry of soils. Oxford University Press, New York, 234p

Sposito G. (1998) On Points of Zero Charge. *Environ. Sci. Technol.* **32**, 2815-2819.

Sposito G. (2004) The Surface Chemistry of Natural Particles. Oxford University Press, New York, 242 p.

Staddon P. L., Bronk Ramsey C., Ostle N., Ineson P. and Fitter A. H. (2003) Rapid turnover of hyphae of mycorrhizal fungi determined by AMS microanalysis of ^{14}C. *Science* **300**, 1138–1140.

Stockmann G. J., Wolff-Boenisch D., Gislason S. R., Oelkers E. H. (2013) Do carbonate precipitates affect dissolution kinetics?: 2: Diopside. *Chem. Geol.* **337-338**, 56-66.

Stuart B. and Ando D. J. (1997) Biological Applications of Infrared Spectroscopy. John Wiley, Chichester, UK.

Sugimori H., Yokoyama T., Murakami T. (2009) Kinetics of biotite dissolution and Fe behaviour under low O_2 conditions and their implications for Precambrian weathering. *Geochim. Cosmochim. Acta* **73**, 3767-3781.

Sun Y. P., Unestam T., Lucas S. D., Johanson K. J., Kenne L., Finlay R. (1999) Exudation-reabsorption in a mycorrhizal fungus, the dynamic interface for interaction with soil and soil microorganisms. *Mycorrhiza* **9**, 137-144.

Sverjensky D. A. (1994) Zero-point-of-charge prediction from crystal chemistry and solvation theory. *Geochim. Cosmochim. Acta* **58**, 3123-3129.

Sverjensky D. A. (2004) Prediction of surface charge on oxides in salt solutions: Revisions for 1:1 (M^+L^-) electrolytes. *Geochim. Cosmochim. Acta* **69**, 225-257.

Swoboda-Colberg N. G., Drever J. I. (1993) Mineral dissolution rates in plot-scale field and laboratory experiments. *Chem. Geol.* **105**, 51-69.

Taylor A. S., Blum J. D., Lasaga A. C., MacInnis I. N. (2000) Kinetics of dissolution and Sr release during biotite and phlogopite weathering. *Geochem. Cosmochem. Acta* **64**, 1191-1208.

Taylor L. L., Leake J. R., Quirk J., Hardy K., Banwart S. A., Beerling D. J. (2009) Biological weathering and the long-term carbon cycle: integrating mycorrhizal evolution and function into the current paradigm. *Geobiology* **7**, 171-191.

Taylor L., Banwart S., Leake J., Beerling D. J. (2011) Modelling the evolutionary rise of ectomycorrhizal on sub-surface weathering environments and the geochemical carbon cycle. *Am. J. Sci.* **311**, 369–403.

Taylor L. L., Banwart S. A., Valdes P. J., Leake J. R., Beerling D. J. (2012) Evaluating the effets of terrestrial ecosystems, climate and carbon dioxide on weathering over geological time: a global-scale process-based approach. *Philos. T. Roy. Soc. B* **367**, 565-582.

Tréguer, P. and P. Le Corre (1975). Manuel d'analyse des sels nutrifs dans l'eau de mer: utilisation de l'Autoanalyzer II Technicon R. Université de Bretagne Occidentale, Bretagne, France.

Treseder K. K., Schimel J. P., Garcia M. O. and Whiteside M. D. (2010) Slow turnover and production of fungal hyphae during a Californian dry season. *Soil Biol. Biochem*. **42**, 1657–1660.

Turpault M. P. and Trotignon L. (1994) The dissolution of biotite single crystals in dilute HNO_3 at 24°C; Evidence of an anisotropic corrosion process of micas in acidic solution. *Geochim. Cosmochim. Acta* **58**, 2761-2775.

Ullman W. J. and Welch S. A. (2002) Organic ligands and feldspar dissolution. In *Water-Rock Interactions, Ore Deposits, and Environmental Geochemistry* (ed. Hellman and Wood) The Geochemical Society, 3-35.

van Hees P. A. W., Jones D. L., Jenstschke G., Godbold D. L. (2005) Organic acid concentrations in soil solution: effects of young coniferous trees and ectomycorrhizal fungi. *Soil Biol. Biochem.* **37**, 771-776.

van Hees P. A. W., Rosling A., Essén S., Godbold D. L., Jones D. L., Finlay R. D. (2006) Oxalate and ferricrocin exudation by the extrametrical mycelium of an ectomycorrhizal fungus in symbiosis with *Pinus sylvestris*. *New Phytol.* **169**, 367-378.

Viollier E., Inglett P. W., Hunter K., Roychoudhury A. N., Van Cappellen P. (2000) The ferrozine method revisited: Fe(II)/Fe(III) determination in natural waters. *Appl. Geochem.* **15**, 785-790.

Voinot A., Lemarchand D., Collignon C., Granet M., Chabaux F., Turpault M.-P. (2013) Experimental dissolution vs. transformation of micas under acidic soil conditions: Clues from boron isotopes. *Geochim. Cosmochim. Acta* **117**, 144-160.

Wallander H. and Wickman T. (1999) Biotite and microcline as potassium sources in ectomycorrhizal and non-mycorrhizal Pinus sylvestris seedlings. *Mycorrhiza* **9**, 25-32.

Wand B. and Qui Y.-L. (2006) Phylogenetic distribution and evolution of mycorrhizas in land plants. Mycorrhiza 16, 299-363.

Webmineral.com (accessed April, 2013) < http://webmineral.com/data/Biotite.shtml>.

Welch S. A. and Ullman. (1993) The effect of organic acids on plagioclase dissolution rates and stoichiometry. *Geochim. Cosmochim. Acta* **57**, 2725-2736.

White A. F. and Brantley S. L. (2003) The effect of time on the weathering of silicate minerals: why do weathering rates differ in the laboratory and field? *Chem. Geol.* **202**, 479-506.

Whitfield J. (2007) Underground networking. *Nature* **449**, 136–138.

Wilkinson S.R.,Welch Ross. M., Mayland H. F. Grunes D. L. (1990) Magnesium in Plants: Uptake, Distribution, Function, and Utilization by Man and Animals. In: *Metals Ions in Biolgical Systems* Vol 26: Compendium on magnesium and its role in Biology, Nutrition and Physiology (ed: Sigel H and Sigel A).

Winkelmann G. (1991) Specificity of iron transport in bacteria and fungi. In *CRC Handbook of microbial iron chelates* (ed. Winkelmann G.), CRC Press, Florida.

Wolff-Boenisch D., Gislason S. R., Oelkers E. H., Putnis C. V. (2004) The dissolution rates of natural glasses as a function of their composition at pH 4 and 10.6 and temperatures from 25 to 74 °C. *Geochim. Cosmochim. Acta* **68**, 4843-4858.

Wolff-Boenisch S. and Traina S. (2007a) The effect of desferrioxamine B on the desorption of U(VI) from Georgia kaolinite KGa-1b and its ligand-promoted dissolution at pH 6 and 25 °C.

Wolff-Boenisch S. and Traina S. (2007b) The effect of desferrioxamine B, enterobactin, oxalic acid and Na-alginate on the dissolution of uranyl-treated goethite at pH 6 and 25 °C. *Chem. Geol.* **243**, 357-368.

Wosten H. A. B., De Vries O. M. H., Wessels J. G. H. (1993) Interfacial self-assembly of a fungal hydrophobin into a hydrophobic rodlet layer: The Plant Cell **5**, 1567–1574.

Appendix A.

Supplementary information for Chapter 4.

Table A– 1

Element weight % of the Grasåsen biotite determined by Olympus Innov-x X-5000 portable XRF at 10 kV.

Element	wt %	±
LE	63.02	0.470
Si	20.26	0.040
P	0.04	0.004
K	5.14	0.009
Ca	1.36	0.005
Ti	1.42	0.022
Cr	0.01	0.011
Mn	0.04	0.003
Fe	8.60	0.025
Sum	99.89	

LE = Light Elements

Table A– 2

Experimental details of biotite-bearing batch titrations. * indicates values of pH_{imm}.

Mineral suspension concentration = 19.98 g/L; Initital fluid composition = 0.01 M NaCl; Titration time = 20 minutes; Suspension volume = 0.007 L

	Titrant (mol/L 10^{-3})		Fluid composition (t = 20; metal concentrations: mol/L 10^{-5})									
Experiment	[HCl]	[NaOH]	pH	Si	Na	Mg	Al	K	Ca	Ti	Mn	Fe
BT-01-01	0	0	9.247*	10.46	982.41	22.75	1.46	254.12	13.57	0.06	0.01	0.19
BT-01-02	9.41	0	5.964	41.29	864.72	101.26	2.08	283.74	345.22	0.16	1.33	0.08
BT-01-10	1.58	0	7.853	12.42	998.09	46.37	0.63	276.56	76.58	0.03	0.02	0.002
BT-01-17	0.16	0	9.053	10.38	1002.03	24.84	1.23	261.06	13.88	0.03	0.01	0.01
BT-01-18	0.00	0.18	9.523	10.70	1044.87	20.75	1.54	258.75	10.75	0.04	0.005	0.03
BT-01-21	0.00	5.79	11.477	28.17	1611.49	0.26	6.01	233.52	3.24	0.04	0.002	DL
BT-01-22	124.72	0	1.272	683.04	1023.22	724.12	772.51	683.73	641.06	34.61	6.49	580.53
BT-01-23	66.50	0	1.692	538.67	818.31	400.33	427.48	468.65	383.69	12.82	3.72	305.44

Mineral suspension concentration = 19.91 g/L; Initital fluid composition = 0.01 M NaCl; Titration time = 60 minutes; Suspension volume = 0.007 L

	Titrant (mol/L 10^{-3})		Fluid composition (t = 60; metal concentrations: mol/L 10^{-5})									
Experiment	[HCl]	[NaOH]	pH	Si	Na	Mg	Al	K	Ca	Ti	Mn	Fe
BT-02-01	0	0	9.811*	12.05	987.86	5.60	2.11	292.30	6.42	0.03	0.00	DL
BT-02-02	93.37	0	1.185	599.65	889.19	548.35	590.54	545.49	414.32	26.27	4.43	450.84
BT-02-03	76.60	0	1.311	584.28	881.21	521.50	569.27	551.26	429.11	22.20	4.50	431.56
BT-02-04	67.90	0	1.419	583.56	898.16	518.31	544.24	554.51	417.97	19.75	4.47	416.10
BT-02-05	58.96	0	1.545	559.06	923.98	508.99	544.15	551.63	428.99	16.67	4.50	400.05
BT-02-06	49.79	0	1.714	536.45	951.08	479.80	509.28	553.69	439.22	13.37	4.40	370.67
BT-02-07	40.37	0	1.991	485.63	928.51	431.98	436.56	493.55	418.45	7.82	4.32	311.64
BT-02-08	30.69	0	2.557	425.90	953.26	379.29	372.89	477.16	400.75	2.78	4.11	238.57
BT-02-09	20.74	0	3.849	251.60	959.43	270.44	143.10	410.84	401.69	0.64	3.62	94.79
BT-02-10	15.67	0	4.359	161.36	958.99	211.47	29.67	407.61	390.64	0.61	3.17	44.37
BT-02-11	9.41	0	6.086	44.44	859.87	116.10	2.26	314.81	310.06	0.15	1.37	0.06
BT-02-12	7.28	0	6.271	31.47	909.57	91.35	0.34	296.40	307.50	0.03	0.60	DL
BT-02-13	5.02	0	7.047	22.67	938.93	70.52	0.42	331.58	250.74	0.03	0.19	DL
BT-02-14	2.59	0	7.888	13.27	952.33	41.43	0.49	292.22	114.58	0.03	0.03	DL
BT-02-15	0.93	0	8.653	8.72	861.77	17.09	0.95	240.53	34.60	0.03	0.01	DL
BT-02-16	0.72	0	8.934	8.74	886.48	14.21	1.11	243.29	24.65	0.03	0.004	DL
BT-02-17	0.50	0	9.185	8.55	917.63	10.92	1.43	241.11	16.05	0.03	0.002	DL
BT-02-18	0.26	0	9.478	9.06	953.36	7.55	1.72	241.21	10.08	0.03	0.001	DL
BT-02-19	0.10	0	9.628	9.38	973.66	6.04	1.98	234.74	8.53	0.03	0.002	DL
BT-02-20	0.00	1.33	10.631	12.82	968.93	1.10	3.92	199.94	1.48	0.03	0.000	DL

Table A– 2 cont.

Mineral suspension concentration = 20.04 g/L; Initital fluid composition = 0.01 M NaCl; Titration time = 60 minutes; Suspension volume = 0.007 L

	Titrant (mol/L 10^{-3})		Fluid composition (t = 60; metal concentrations: mol/L 10^{-5})									
Experiment	[HCl]	[NaOH]	pH	Si	Na	Mg	Al	K	Ca	Ti	Mn	Fe
BT-03-01	0	0	9.931*	9.30	976.60	6.08	2.17	301.60	5.71	0.03	0.00	DL
BT-03-02	93.37	0	1.166	576.30	912.71	496.87	538.78	562.44	399.81	28.90	4.25	407.47
BT-03-03	76.60	0	1.287	570.83	936.14	497.56	535.56	555.28	475.58	26.49	4.52	404.86
BT-03-04	67.90	0	1.382	554.90	953.30	497.43	534.80	579.52	490.94	24.42	4.53	398.14
BT-03-05	58.96	0	1.502	546.19	1053.14	488.71	523.32	664.01	525.43	21.67	4.76	387.28
BT-03-06	49.79	0	1.647	517.14	972.31	450.99	471.12	534.64	499.70	17.77	4.36	340.88
BT-03-07	40.37	0	1.889	477.18	989.96	417.78	436.99	537.41	493.54	11.61	4.32	302.47
BT-03-08	30.69	0	2.437	425.71	984.14	363.14	371.03	498.94	491.15	4.21	4.11	230.60
BT-03-09	20.74	0	3.785	259.06	1062.81	272.55	164.85	436.17	486.67	0.66	3.66	103.84
BT-03-10	15.67	0	4.314	158.88	972.84	200.20	29.57	414.01	462.19	0.36	3.25	46.82
BT-03-11	9.41	0	5.810	89.37	879.19	107.33	2.26	310.92	329.36	0.16	1.66	0.06
BT-03-12	7.28	0	6.535	75.69	894.79	86.42	1.80	326.82	292.79	0.15	0.62	DL
BT-03-13	5.02	0	7.091	14.36	924.23	65.75	0.42	332.73	261.19	0.03	0.19	DL
BT-03-14	2.59	0	7.869	9.28	949.76	39.87	0.52	289.40	119.09	0.03	0.04	0.01
BT-03-15	0.93	0	8.784	8.70	859.76	16.32	1.01	230.04	34.75	0.03	0.01	0.01
BT-03-16	0.72	0	9.012	8.73	903.92	13.15	1.20	229.97	24.40	0.03	0.01	0.01
BT-03-17	0.50	0	9.232	9.14	925.08	10.38	1.44	244.35	16.72	0.03	0.004	0.01
BT-03-18	0.26	0	9.547	9.58	946.17	7.63	1.82	236.82	10.60	0.03	0.003	0.01
BT-03-19	0.10	0	9.749	14.75	978.07	6.29	2.12	239.80	8.43	0.03	0.002	0.01
BT-03-20		1.33	10.733	9.67	990.80	1.15	3.58	370.65	3.75	0.03	0.002	0.002

Table A– 2 cont.

[a] Biotite-bearing suspension 5 mL

Mineral suspension concentration = 19.99 g/L; Initital fluid composition = 0.001 M NaCl; Titration time = 20 minutes; Suspension volume = 0.007 L

	Titrant (mol/L 10^{-3})		Fluid composition (t = 20; metal concentrations: mol/L 10^{-5})									
Experiment	[HCl]	[NaOH]	pH	Si	Na	Mg	Al	K	Ca	Ti	Mn	Fe
BT-04-01	0	0	9.476*	55.08	101.27	6.83	3.17	267.08	19.70	0.27	DL	DL
BT-04-02	72.28	0	1.336	563.72	96.64	492.96	522.88	551.01	521.21	27.02	4.17	385.77
BT-04-03	49.79	0	1.614	504.23	101.12	423.18	447.79	513.93	505.27	18.57	3.89	313.06
BT-04-04	40.37	0	1.874	469.64	106.49	403.94	431.74	526.93	510.01	12.72	3.78	292.94
BT-04-05	30.69	0	2.548	420.33	116.75	356.99	368.20	530.44	480.80	3.86	3.89	223.75
BT-04-06	28.23	0	2.920	389.95	121.92	333.67	331.27	532.38	475.70	2.43	3.65	187.89
BT-04-07	25.75	0	3.333	356.87	114.98	318.58	278.95	521.82	471.12	1.62	3.53	157.80
BT-04-08	23.26	0	3.564	298.55	95.70	288.16	201.17	429.10	460.48	1.08	3.39	120.69
BT-04-09	20.74	0	3.861	247.00	127.82	274.60	146.85	473.52	498.65	0.87	3.41	94.47
BT-04-10	18.21	0	4.022	203.89	111.62	242.58	89.67	434.47	474.66	0.86	3.18	71.70
BT-04-11	15.67	0	4.396	153.25	112.47	192.03	24.87	393.13	450.83	0.81	2.69	38.38
BT-04-12	13.10	0	5.240	118.30	111.99	153.53	3.94	366.37	412.20	0.38	2.44	11.84
BT-04-13	10.52	0	5.878	39.14	107.81	131.65	1.77	377.93	394.12	0.21	1.83	0.60
BT-04-14	8.99	0	6.129	31.85	100.93	104.07	1.69	325.75	327.08	0.21	1.14	DL
BT-04-15	7.72	0	6.342	31.15	98.16	91.31	1.61	314.97	291.38	0.19	0.66	DL
BT-04-16	7.28	0	6.466	20.22	103.50	88.92	1.69	322.72	284.69	0.22	0.57	DL
BT-04-17[a]	7.52	0	6.966	31.19	104.56	69.16	1.68	314.79	221.41	0.22	0.10	DL

Table A– 3

Experimental details of biotite-free batch titrations. Fluids equilibrated with biotite for 12 hours and subsequently filtered prior to titration. * indicates values of pH_{imm}.

	Titrant (mol/L 10^{-3})	
Experiment	[HCl]	pH
BT-05-01	0	9.638*
BT-05-02	11.04	1.938
BT-05-03	6.79	2.178
BT-05-04	5.21	2.313
BT-05-05	3.56	2.552
BT-05-06	2.70	2.763
BT-05-07	1.82	3.181
BT-05-09	0.68	6.577
BT-05-10	0.52	7.110
BT-05-11	0.36	7.481
BT-05-12	0.18	8.279
BT-05-13	0.07	8.860

Mineral suspension concentration = 19.73 g/L; Initital fluid composition = 0.001 M NaCl; Titration time = 20 minutes; Suspension volume = 0.002 L

	Titrant (mol/L 10^{-3})	
Experiment	[HCl]	pH
BT-06-01	0	9.839*
BT-06-02	67.90	1.095
BT-06-03	48.86	1.253
BT-06-04	35.56	1.389
BT-06-05	21.75	1.602
BT-06-06	11.04	1.905
BT-06-07	6.79	2.155
BT-06-08	3.56	2.536
BT-06-09	0.68	6.710
BT-06-10	0.36	7.511
BT-06-11	0.07	9.002

Mineral suspension concentration = 20.08 g/L; Initital fluid composition = 0.001 M NaCl; Titration time = 20 minutes; Suspension volume = 0.002 L

	Titrant (mol/L 10^{-3})	
Experiment	[HCl]	pH
BT-07-01	0	9.661*
BT-07-02	11.04	1.901
BT-07-03	6.79	2.128
BT-07-04	5.21	2.276
BT-07-05	3.56	2.508
BT-07-06	2.70	2.727
BT-07-07	1.82	3.165
BT-07-08	0.92	6.338
BT-07-09	0.68	6.694
BT-07-10	0.52	6.972
BT-07-11	0.36	7.461
BT-07-12	1.46	3.621
BT-07-13	1.10	5.926
BT-07-14	1.28	4.752

Table A– 4

Experimental details of electrokinetic titrations performed at 25 °C.

Ionic Strength	Electrolyte	pH	Mobility		ζ-potential	
			(μm/s/V/cm)	S.D.	(mV)	S.D.
0.001	HCl	3.032	0.05	0.28	0.71	3.75
	NaCl	3.664	-0.67	0.27	-9.16	3.64
		4.453	-1.26	0.29	-17.11	3.94
		6.256	-3.34	0.24	-45.2	3.25
		6.253	-3.67	0.36	-46.69	4.87
		6.339	-4.26	0.51	-57.65	6.85
0.005	NaCl	3.650	-0.22	0.27	-3.22	3.97
		4.898	-0.6	0.25	-8.74	3.63
		5.974	-1.93	0.23	-28.12	3.40
		6.240	-2.35	0.43	-34.12	6.28
		6.111	-2.36	0.38	-34.27	5.49
		6.651	-2.27	0.59	-32.91	8.53
		6.566	-2.47	0.37	-35.8	5.42
		7.231	-3.13	0.31	-45.31	4.51
0.01	HCl	2.006	0.37	0.22	4.93	2.92
	NaCl	2.966	-0.38	0.20	-5.02	2.70
		3.924	-0.75	0.21	-9.98	2.80
		4.920	-1.21	0.23	-16.05	3.11
		5.822	-1.97	0.27	-26.01	3.57
		6.182	-2.44	0.31	-32.46	4.14
		6.618	-2.76	0.29	-36.71	3.83
		6.714	-2.71	0.48	-36.01	6.41
		7.250	-2.91	0.37	-38.59	4.97
		7.266	-2.59	0.19	-34.3	2.52
		7.480	-2.9	0.25	-38.29	3.30
		7.890	-3.01	0.38	-39.7	5.04
		8.303	-3.27	0.18	-43.08	2.31
		8.923	-3.21	0.23	-42.27	2.97
0.05	NaCl	1.941	0.43	0.18	6.06	2.49
		2.489	0.3	0.19	4.25	2.73
		3.074	0.12	0.17	1.65	2.45
		4.411	-0.3	0.15	-4.23	2.11
		5.732	-0.55	0.23	-7.66	3.20
		6.296	-1.4	0.33	-19.65	4.59
		6.643	-2.1	0.18	-29.29	2.45
		6.726	-2.11	0.22	-29.52	3.88
		6.724	-2.2	0.25	-30.74	3.55
		6.712	-2.16	0.35	-30.14	4.88
		6.901	-2.17	0.24	-30.33	3.32
		7.370	-2.21	0.19	-30.86	2.71
		7.861	-2.31	0.29	-32.24	3.98
		8.276	-2.51	0.34	-34.94	4.68
		10.096	-2.72	0.15	-37.91	2.16
0.1	HCl	1.055	0.21	0.36	2.92	5.03
	NaCl	1.929	0.24	0.20	3.31	2.83
		2.450	0.41	0.19	5.68	2.58
		3.012	0.31	0.09	4.25	1.24
		3.670	-0.05	0.16	-0.75	2.27
		5.462	-0.56	0.16	-7.78	2.29
		6.333	-1.35	0.19	-18.77	2.64
		6.528	-1.71	0.19	-23.71	2.59
		6.684	-1.56	0.21	-21.71	2.95
		6.761	-1.54	0.16	-21.39	2.18
		6.800	-1.68	0.20	-23.36	2.80
		6.945	-1.72	0.11	-23.83	1.52
		7.317	-2.01	0.31	-27.84	4.30
		9.072	-2.03	0.23	-28.16	3.23
		11.661	-2.18	0.23	-30.17	3.24

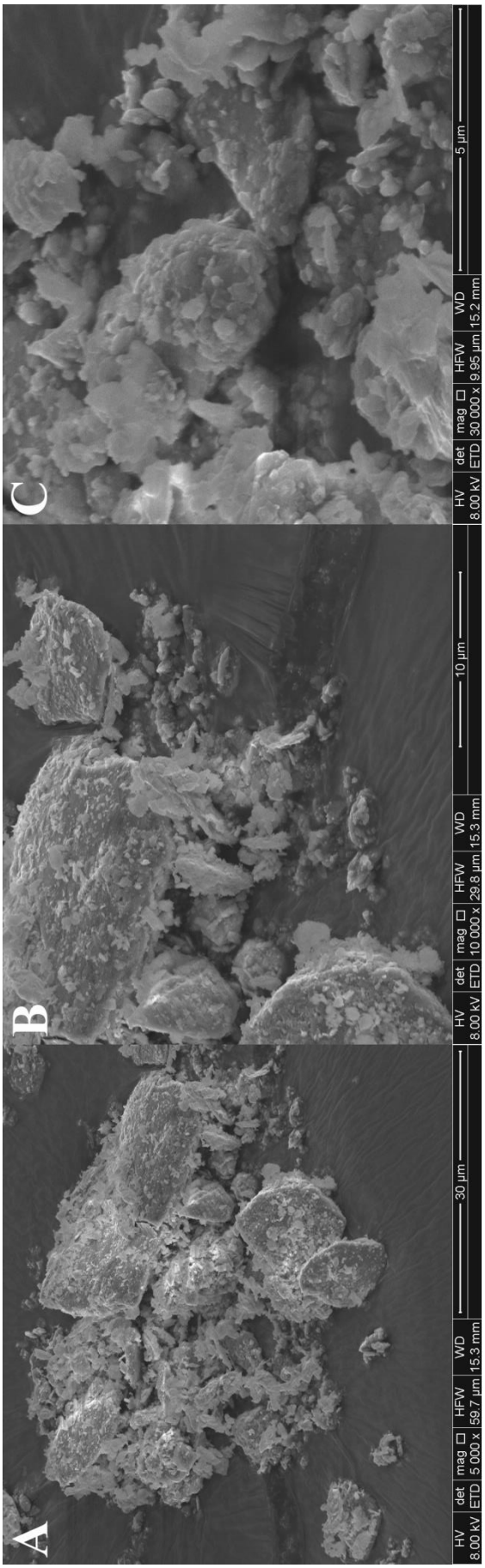

Figure A– 1

Scanning electron micrographs of crushed biotite, pre immersion with the NaCl electrolyte at magnifications of 5000 (A), 10000 (B) and 30000 (C).

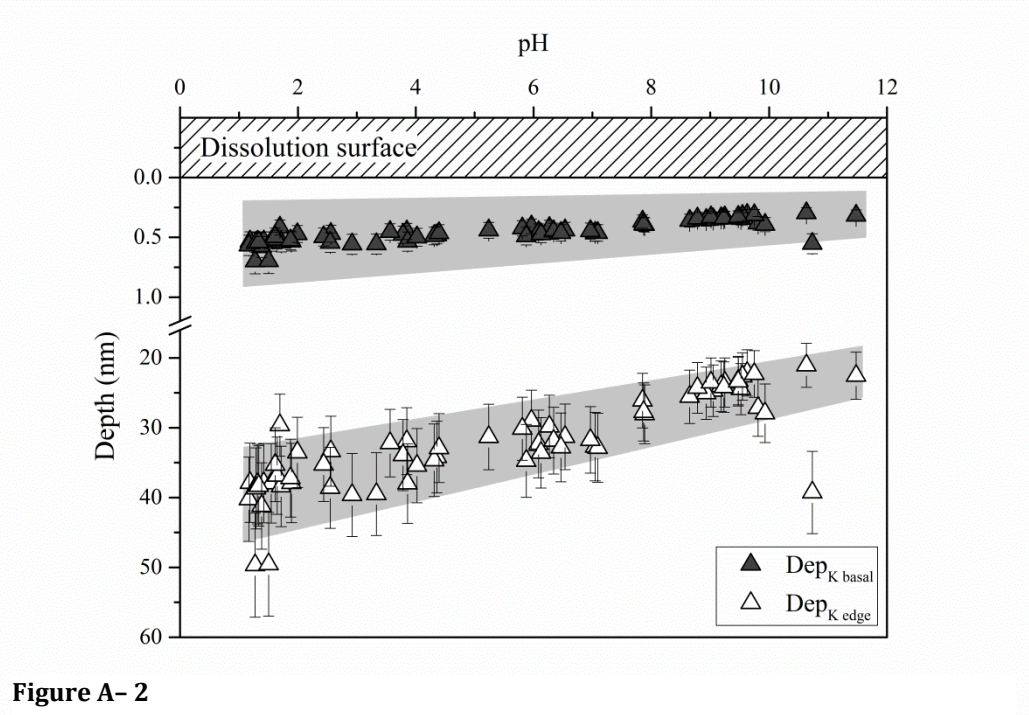

Figure A– 2

Average K depletion depth at the basal ($Dep_{K\ basal}$) and edge ($Dep_{K\ edge}$) surfaces as a function of pH. The points represent the relative depletion depths based on an edge:basal reactivity ratio of 71:1 (Hodson, 2006) with the shaded representing depths based on the maximum and minimum edge:basal ratios of 240:1 and 36:1 (Turpault and Trotignon, 1994). Note the break in the y-axis and the change of scale. Error bars represent a 15% uncertainty in the calculated depletion depths.

Appendix B.

Supplementary information for Chapter 5.

Table B– 1

Fluid saturation state with respect to Al and Fe secondary phases, calculated using PHREEQC3. Calculations based on electrolyte/buffer ionic strength of 0.01 M, and the released concentrations of elements from biotite after 12 hours of closed-system reaction.

Solution	pH	α-$Al(OH)_3$	Al_2O_3	Ferrihydrite	Gibbsite
NaCl electrolyte	2.56	-8.19	-14.43	0.09	-5.68
	3.21	-6.40	-10.85	0.96	-3.89
	4.16	-3.75	-5.56	1.75	-1.24
	5.18	-1.28	-0.61	2.45	1.23
	5.95	-0.85	0.24	2.37	1.65
Phthalate buffer	2.56	-8.13	-14.31	-0.05	-5.62
	3.21	-6.57	-11.19	0.64	-4.06
	4.16	-4.68	-7.42	1.28	-2.17
	5.18	-2.84	-3.74	1.95	-0.33
	5.95	-1.66	-1.37	2.24	0.85
Phthalate buffer + Citrate	2.56	-8.50	-15.06	-1.98	-6.00
	3.21	-7.67	-13.38	-1.69	-5.16
	4.16	-6.85	-11.75	-1.00	-4.34
	5.18	-5.90	-9.86	0.45	-3.39
	5.95	-4.94	-7.93	2.00	-2.43
Phthalate buffer + Oxalic	2.56	-8.75	-15.55	-5.28	-6.24
	3.21	-7.99	-14.04	-4.86	-5.48
	4.16	-6.51	-11.08	-3.81	-4.00
	5.18	-4.24	-6.54	-1.80	-1.73
	5.95	-2.21	-2.47	0.18	0.30
Phthalate buffer + DFOB	2.56	-9.97	-17.99	-7.53	-7.46
	3.21	-10.18	-18.42	-7.70	-7.67
	4.16	-10.47	-19.00	-7.93	-7.97
	5.18	-10.52	-19.10	-7.99	-8.01
	5.95	-10.68	-19.41	-8.14	-8.17

Table B– 2

Stability constants for phthalate, citrate, oxalate and DFOB used in PHREEQC3 calculations.

Reactants	Products	log *K*	Reference
H+, K–Phthalate-	KH–Phthalate	5.40	Martell et al., 2004
K+, Phthalate-2	K–Phthalate-	0.70	Martell et al., 2004
H+, Phthalate-2	H–Phthalate-	5.41	Martell et al., 2004
H+, H–Phthalate-	H2–Phthalate	2.95	Martell et al., 2004
Al^{+3}, $Phthalate^{-2}$	$Al–Phthalate^{+}$	4.56	Martell et al., 2004
Al^{+3}, $2Phthalate^{-2}$	$Al–Phthalate_2^{-}$	7.20	Martell et al., 2004
Fe^{+3}, $Phthalate^{-2}$	$Fe–Phthalate^{+}$	6.07	Martell et al., 2004
Fe^{+3}, $2Phthalate^{-2}$	$Fe–Phthalate_2^{-}$	10.56	Martell et al., 2004
Fe^{+3}, $3Phthalate^{-2}$	$Fe–Phthalate_3^{-3}$	13.26	Martell et al., 2004
Mg^{+2}, $Phthalate^{-2}$	Mg–Phthalate	2.49	Martell et al., 2004
$2H^{+}$, $Citrate^{-3}$	$H_2–Citrate^{-}$	11.16	Martell et al., 2004
$3H^{+}$, $Citrate^{-3}$	H_3–Citrate	14.29	Martell et al., 2004
Al^{+3}, $Citrate^{-3}$	Al–Citrate	9.97	Martell et al., 2004
Al^{+3}, $2Citrate^{-3}$	$Al–Citrate_2^{-3}$	14.80	Martell et al., 2004
Al^{+3}, H^{+}, $Citrate^{-3}$	$AlH–Citrate^{+}$	12.85	Martell et al., 2004
Fe^{+2}, $Citrate^{-3}$	$Fe–Citrate^{-}$	6.10	Martell et al., 2004
Fe^{+2}, H^{+}, $Citrate^{-3}$	FeH–Citrate	10.20	Martell et al., 2004
Fe^{+3}, $Citrate^{-3}$	Fe–Citrate	13.10	Martell et al., 2004
Fe^{+3}, H^{+}, $Citrate^{-3}$	$FeH–Citrate^{+}$	14.40	Martell et al., 2004
Mg^{+2}, $Citrate^{-3}$	$Mg–Citrate^{-}$	4.89	Martell et al., 2004
Mg^{+2}, H^{+}, $Citrate^{-3}$	MgH–Citrate	8.91	Martell et al., 2004
Mg^{+2}, $2H^{+}$, $Citrate^{-3}$	MgH_2–Citrate	12.20	Martell et al., 2004
H^{+}, $H–Oxalate^{-}$	H_2–Oxalate	1.25	Martell et al., 2004
H^{+}, $Oxalate^{-2}$	$H–Oxalate^{-}$	4.27	Martell et al., 2004
Al^{+3}, $Oxalate^{-2}$	$Al–Oxalate^{+}$	6.00	Martell et al., 2004
Al^{+3}, $2Oxalate^{-2}$	$Al–Oxalate_2^{-}$	11.00	Martell et al., 2004
Fe^{+3}, $Oxalate^{-2}$	$Fe–Oxalate^{+}$	9.74	Martell et al., 2004
Fe^{+3}, $2Oxalate^{-2}$	$Fe–Oxalate_2^{-}$	16.76	Martell et al., 2004
Fe^{+3}, $3Oxalate^{-2}$	$Fe–Oxalate_3^{-2}$	20.54	Martell et al., 2004
Mg^{+2}, $Oxalate^{-2}$	Mg–Oxalate	3.43	Martell & Smith, 1977
Mg^{+2}, $2Oxalate^{-2}$	$Mg–Oxalate_2^{-2}$	4.24	Martell & Smith, 1977
H^{+}, $DFOB^{-3}$	$H–DFOB^{-2}$	11.48	Martell et al., 2004
H^{+}, $H–DFOB^{-2}$	$H_2–DFOB^{-}$	9.98	Martell et al., 2004
H^{+}, $H_2–DFOB^{-}$	H_3–DFOB	9.20	Martell et al., 2004
H^{+}, H_3–DFOB	$H_4–DFOB^{+}$	8.30	Martell et al., 2004
Al^{+3}, $H–DFOB^{-2}$	$AlH–DFOB^{+}$	25.46	Martell et al., 2004
$AlH–DFOB^{+}$	Al–DFOB, H^{+}	-9.41	Martell et al., 2004
H^{+}, $AlH–DFOB^{+}$	$AlH_2–DFOB^{+2}$	1.20	Martell et al., 2004
Fe_{+3}, $H-DFOB^{-2}$	$FeH–DFOB^{+}$	31.90	Martell et al., 2004
$FeH–DFOB^{+}$	Fe–DFOB, H^{+}	-10.38	Martell et al., 2004
H^{+}, $FeH–DFOB^{+}$	$FeH_2–DFOB^{+2}$	1.00	Martell et al., 2004
Mg^{+2}, H–DFOB-2	MgH–DFOB	4.30	Martell & Smith, 1977

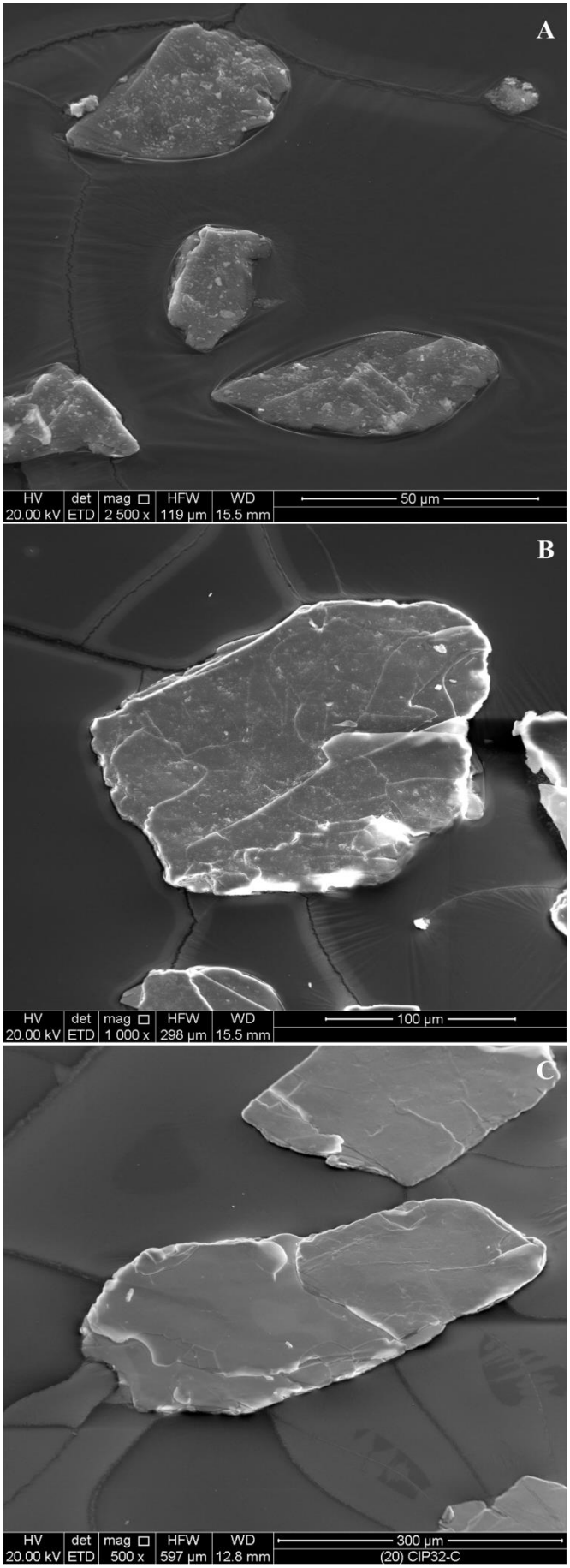

Figure B– 1

Scanning electron microscope images of Graså sen biotite grains before reaction from the (A) 25-53 µm, (B) 53-180 µm, and (C) 180-500 µm size fractions.

Figure B– 2 (opposite)

Surface area and stoichiometry normalised concentrations of released elements from biotite in ligand-free, citric acid, oxalic acid and DFOB closed-system experimental fluids, as a function of time. The figure presents data by element (Al, Fe, Mg, Si, right to left), and pH (2.5 to 6, top to bottom), and includes the concentrations after 12 hours for each pH and experimental fluid in the lowest row.

Appendix C.

Appendix C is a is reproduction of a peer-reviewed publication in *Geochimica et Cosmochimica Acta*:

Bray A. W., Benning L. G., Bonneville S., Oelkers E. H. (2014) Biotite surface chemistry as a function of aqueous fluid composition. *Geochim. Cosmochim Acta* **128**, 58-70.

Appendix D.

Appendix D is a reproduction of a peer-reviewed publication in *Geochimica Cosmochimica Acta* which the candidate is an author on.

Bonneville S., Morgan D. J., Schmalenberger A., **Bray A.**, Brown A., Banwart S. A., Benning L. G. (2011) Tree-mycorrhiza symbiosis accelerate mineral weathering: Evidences from nanometer-scale elemental fluxes at the hypha–mineral interface. *Geochimica et Cosmochimica Acta* **75**, 6988-7005.

Al

Fe

Mg

Si

pH 2.5

pH 3

pH 4

pH 5

pH 6

$t = 12$ hours